U.PORTO
FEUP FACULDADE DE ENGENHARIA
UNIVERSIDADE DO PORTO

Faculdade Engenharia da Universidade do Porto
Departamento de Engenharia Mecânica e Gestão Industrial

Torque Loss in a Planetary Multiplier Gearbox: Influence of Operating Conditions and Gear Oil Formulation

Raquel Camacho Simões Dias

Master's Degree Dissertation presented to
Faculdade de Engenharia da Universidade do Porto

Dissertation supervised by

Dr. Ramiro Carneiro Martins
Auxiliary researcher of INEGI

Dr. Jorge Humberto O. Seabra
Full Professor of FEUP

Porto, July 2014

LaTeX

FEUP-U.PORTO

r.camacho

2014

to Eng. Manuel Camacho Simões,
my grandfather and greatest teacher

Acknowledgements

I would like to express my gratitude to a few people who have helped and supported me throughout my Master's Degree Thesis.

First of all, I would like to express my very great appreciation to my supervisors, Prof. Jorge H. O. Seabra, Dr. Ramiro C. Martins and Eng. Pedro M. T. Marques, for their support, availability, guidance and for all the transmitted knowledge.

I would like to offer my special thanks to CETRIB (Unidade de Tribologia, Vibrações e Manutenção Industrial) for having given me the opportunity of doing this work in an outstanding laboratory. To my CETRIB colleagues: Armando Campos, Beatriz Graça, Carlos Fernandes, David Gonçalves, João Nogueira, Jorge Castro, José Brandão and Samuel Pinho, I would like to give my sincere thanks not only for all the help and support, but also for the warm welcome and the good moments we shared.

I wish to acknowledge Fundação para a Ciência e Tecnologia for the financial support given through the project *Transmissões por engrenagem de elevada eficiência e fiabilidade tribológica*, with research contract EXCL/EMS-PRO/0103/2012.

I would also like to acknowledge Faculdade de Engenharia da Universidade do Porto for the time and resources spent on my Master's degree in Mechanical Engineering.

This thesis represents the end of a five years journey. To the strangers I met as a freshman and to whom I have the honor to call friends, thank you. College life wouldn't be the same without you. You are unbeatable.

Last, but for sure not the least, I would like to give my biggest thank you to my family, for being always there. You are three powerful guardian angels.

Keywords

Wind Turbine gear oils

Power loss

Efficiency

Planetary gearbox

Multiplier gearbox

Coefficient of Friction

Gears friction loss

Rolling bearings power loss

Wear

Palavras Chave

Lubrificantes para engrenagens de turbinas eólicas

Perdas de Potência

Eficiência

Engrenagens planetárias

Caixa de engrenagens multiplicadora

Coeficiente de fricção

Perdas de potência por atrito nos engrenamentos

Perdas de potência nos rolamentos

Desgaste

Abstract

In the past few years, sustainability issues have acquired major importance, as the environmental toxicity and the ozone layer destruction indicators reach worrying levels. Worldwide effort have been made aiming to increase renewable energy production and to diminish the usage of energy produced with fossil fuels.

One of the most relevant renewable energy is the wind power, which represents the second greatest renewable energy source worldwide. Wind power is obtained through wind turbines, converting the kinetic power of the wind to mechanical energy.

One of the most important components in a wind turbines is the gearbox, where the rotational speed of the rotor is multiplied in order to match the working conditions of the generator. Despite the wind energy industry development, wind turbine are still experiencing several breakdowns in the gearboxes and in the roller bearings due to the high loads and variable working conditions, requiring regular maintenance interventions.

Optimizing the gearbox efficiency represents not only an increase of the amount energy produced per wind turbine, but also leads to lower operating temperatures which benefits the working life of all components. Lower operating temperatures lead to a lower failure probability, therefore lowering the maintenance costs.

The purpose of this work is to continue the studies already done by Gonçalves [1], Marques [2] and Pereira [3], in an effort to clarify the influence of the oil formulation on a gearbox efficiency. Gonçalves and Marques [1, 2] carried out tests in parallel shaft helical gears, although with different working conditions. Pereira [3] has done tests in planetary gears at low loads.

The work that is presented in this document consisted in tests with planetary gears, with the care that the operating conditions matched the first stage of a wind turbine gearbox in terms of tangential speed and Hertz pressure. Four lubricants were tested: two of them being mineral based, and two of them being synthetic. Several working parameters indicators of the oil performance were measured and analyzed. Also, oil samples were collected and the wear indexes were calculated, and the wear particles were analyzed, using Direct Reading Ferrography (DRIII) and Analytical Ferrography (FRIII).

A power loss numerical model was implemented aiming to understand the influence of each component in the power loss of the tested gearbox .

Resumo

Nos últimos anos a questão da sustentabilidade tem ganho particular relevância, à medida que os vários indicadores de toxicidade ambiental e de destruição da camada de ozono atingem valores preocupantes. Um pouco por todo o mundo estão a ser feitos esforços no sentido de se aumentar a produção de energia através de fontes renováveis e no sentido de se diminuir a quantidade de energia produzida a partir da queima de combustiveis fósseis.

Uma das energias renovaveis de maior importânica é a energia eólica, representando a segunda maior fonte de energia renovavel à escala mundial. A energia eólica é obtida através de turbinas eólicas que convertem a energia cinética do vento em energia mecânica.

Um dos componentes mais relevantes de uma turbina eólica é a caixa de engrenagens, onde a velocidade de rotação do rotor é multiplicada de forma a atingir as condições de funcionamento do gerador. Apesar do desenvolvimento da indústria de energia eólica, as turbinas eólicas continuam a apresentar inúmeras falhas ao nivel das engrenagens e dos rolamentos, devido às elevadas cargas a que estão sujeitos e às condições de funciomento variavel, obrigando a intervenções de manutenção regulares.

A optimização da eficiência da caixa de engrenagens representa não só um aumento na quantidade de energia gerada por cada turbina eólica, como conduz a temperaturas de funcionamento mais baixas, o que beneficia a vida geral de todos os componentes em funcionamento. Temperaturas de funcionamento mais baixas conduzem a uma menor probabilidade de avaria, reduzindo também os custos de manutenção.

O objectivo deste trabalho é dar continuação aos estudos realizados por Gonçalves [1], Marques [2] e Pereira [3], no sentido de clarificar a influência da formulação de lubrificação na eficiência de uma caixa de engrenagens. Gonçalves e Marques [1, 2] levaram a cabo testes em caixas de engrenagens helicoidais, embora com condições de funcionamento diferentes. Pereira [3] realizou testes em caixas planetárias com um nivel de carga reduzido.

O trabalho levado a cabo consistiu na realização de testes em caixas planetárias, com o cuidado de que as condições de funcionamento fossem equiparadas ao primeiro andar da caixa de engrenagens de uma turbina eólica em termos de velocidade tangencial e de pressão de Hertz. Foram testados quatro lubrificantes diferentes: dois de base mineral e dois sintéticos. Foram avaliados vários parâmetros de funcionamento indicadores da *performance* de cada óleo. Foram também retiradas amostras de lubrificante de forma a determinar os indices de desgaste e a analisar as particulas de desgaste, através de Ferrometria de Leitura Directa (DRIII) e Ferrometria Analítica (FRIII).

Foi implementado um modelo numérico de perda de potência com o objectivo de analisar a perda de potência associada a cada componente da caixa de engrenagens.

Nomenclature

Symbol	Units	Description
a	m	Centre distance
$a_{0,1,2,3,4}$	–	Coefficients dependent on tip contact ratio
A	m^2	External area of the gearbox
b	m	Gear width
B	mm	Rolling bearing width
$c_{A,B}$	N/m	Rolling bearing spring constant
$CPUC$	–	Index of wear particle concentration
C_w	–	Variable used for the calculation of the frictional moment of drag losses
d	mm	Rolling bearing bore diameter
D	mm	Rolling bearing outside diameter
D_L	–	Number of large particles
d_m	m	Bearing mean diameter
D_S	–	Number of small particles
d_{sh}	mm	Shaft diameter
d_i	m	Gear reference diameter
E^*	Pa	Equivalent Young modulus
F	N	Force
f_A	–	Variable used for the calculation of the frictional moment of drag losses
F_a	N	Axial Force
F_{bt}	N	Tooth normal force (transverse section)
F_r	N	Radial Force
f_t	–	Variable used for the calculation of the frictional moment of drag losses
F_t	N	Tangential force
f_0	–	Coefficient dependent on bearing design and lubrication method
F_0	N	Preload force
$f_{1,2}$	–	Coefficient that takes into account the direction of load application
G_{rr}	N·m	Variable for the calculation of the rolling frictional moment
G_{sl}	N·m	Variable for the calculation of the sliding frictional moment
H	mm	Oil level

h_0	m	Film thickness
h_{0T}	m	Corrected film thickness
H_V	–	Gear loss factor
$ISUC$	–	Index of wear severity
K	W/m·m	Thermal conductivity
K_a	N	Axial load on the tapered roller bearings, necessary for the preload calculation
$K_{ball,roll}$	–	Rolling element related constant
K_{rs}	–	Replenishment/starvation coefficient
K_Z	–	Bearing type related geometric constant
i	–	Gear ratio
i_{rw}	–	Number of rows of the bearing
l	m	Average sum of contacting lines length
L	–	Thermal parameter of the lubricant
l_D	–	Variable used for the calculation of the frictional moment of drag losses
l_g	–	Parameter for the calculation of $a_{0,1,2,3,4}$
m	m	Module
m_g	–	Parameter for the calculation of $a_{0,1,2,3,4}$
M	N·m	Total frictional moment of a bearing
$M_{A,D,ext,mot}$	N·m	Moment or torque (index related to the application point)
M_{drag}	N·m	Frictional moment of drag losses
M_{rr}	N·m	Rolling frictional moment
M_{seal}	N·m	Frictional moment of the bearing seal
M_{sl}	N·m	Sliding frictional moment
n	rpm	Rotational speed
N	–	Number of planets
n_{sh}	Rad/s	Shaft rotational speed
n_g	–	Parameter for the calculation of $a_{0,1,2,3,4}$
p	Pa	Pressure
P_a	W	Transmitted power
p_H	N/mm^2	Contact pressure
p_R	N/mm^2	Reference value for contact pressure
P_V	W	Total power loss
P_{VD}	W	Seals power loss
P_{VD0}	W	Rolling bearings no-load losses
P_{VDP}	W	Rolling bearings load losses
P_{VZ0}	W	Gears no-load power losses
P_{VZP}	W	Gears load losses
$\dot{Q}_{cd}$	W	Heat flow rate due to conductuion
$\dot{Q}_{cv}$	W	Heat flow rate due to convection
$\dot{Q}_{rad}$	W	Heat flow rate due to radiation
$\dot{Q}_{total}$	W	Total heat flow rate
R_a	m	Arithmetic mean roughness

r_b	m	Base radius
R_S	–	Variable used for the calculation of the frictional moment of drag losses
R_X	m	Equivalent radius
$R_{1,2}$	–	Geometric constants for rolling frictional moment
t	–	Variable used for the calculation of the frictional moment of drag losses
T	K or °C	Temperature
T_{Oil}	°C	Oil temperature
T_{Room}	°C	Room temperature
T_{VL}	N·m	Total frictional moment of a needle bearing
T_{VL0}	N·m	No-load component of frictional moment of a needle bearing
T_{VL1}	N·m	Load component of frictional moment of a needle bearing
U	–	Speed parameter
$U_{1,2}$	m/s	Velocity of each surface
v	m/s	Tangential speed
V_e	–	Sliding ratio
$V.I.$	–	Viscosity index
V_M	–	Drag loss factor
W	–	Load parameter
Y	–	Axial load factor for single-row bearings
Z	–	Number of teeth
α	Pa^{-1}	Coefficient of piezoviscosity
α_t	Rad	Transverse pressure angle
α_{SKF}	°	Variable used to calculate G_{rr}
α_{Heat}	W/m·K	Heat transfer coefficient
β	K^{-1}	Thermoviscous coefficient
β_b	Rad	Base helix angle
ΔT	°	Stabilized operating temperature
ϵ_α	–	Transverse contact ratio
$\epsilon_{1,2}$	–	Tip contact ratio
η	Pa·s	Dynamic viscosity
η_0	Pa·s	Dynamic viscosity at the oil bath temperature
Λ	–	Specific film thickness
μ_{bl}	–	Coefficient dependent on the lubricant additive package
μ_{mz}	–	Coefficient of friction
μ_{sl}	–	Sliding friction coefficient
ν	cSt	Kinematic viscosity
ξ	–	Portion of fluid film
ϕ_{bl}	–	Weighting factor for the sliding friction coefficient
ϕ_{ish}	–	Inlet shear heating reduction factor
ϕ_{rs}	–	Kinematic replenishment/starvation reduction factor
ϕ_T	–	Inlet heating influence factor
ω	Rad/s	Rotational speed

Contents

List of Figures

List of Tables

1. Introduction

Modern energy enables quality of life. From lighting and heating to powering cutting-edged technology, modern energy is one of the foundations of mankind as we know it today. Yet, over one billion people lack access to modern energy and as world population increases so increases world's energy demand [4].

Global warming and environmental issues are major concerns that push us toward renewable energy and efficiency improvements in energy generation and consumption. Efficiency is expected to be the most important factor in the near term, whereas renewables will become increasingly important over time [4].

By 2035, it is expected that renewables will be generating more than 25% of world's electricity, with a quarter of this coming from wind. Over the last 18 years, the global wind installed capacity has grown from 6GW in 1996 to nearly 320GW in 2013 [5], as shown in figure 1.1.

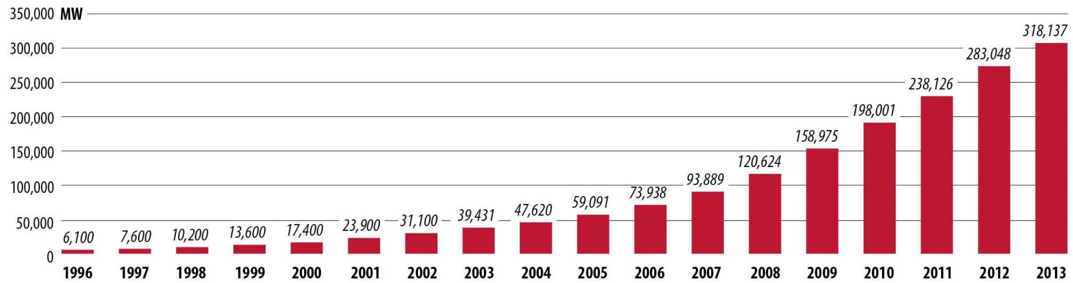

Figure 1.1.: Global cumulative wind installed wind capacity 1996 – 2013 [5].

Wind turbines are used to generate electricity from the kinetic power of the wind. The blades are aerodynamically designed to spin as the air flows through them, converting the kinematic energy of the wind into mechanical energy - torque - which is transmitted along the main shaft to the generator. The rotor rotational speed and torque are transformed by the gearbox in order to match the necessary operating conditions of the generator.

Global wind capacity owns its growth not only to the number of installed turbines but also to the growing capacity of each unit. Figure 1.2 shows the average diameter and capacity of wind turbines in 1985 and today, as well as the expectation for the future.

As the rated power increases, the drive train concept evolves. Research on direct-drive systems and torque splitting mechanism is being done in order to keep up the

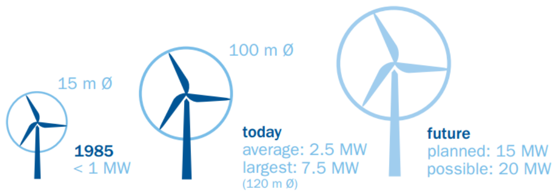

Figure 1.2.: Size and capacity of wind turbines: evolution and prediction [6].

growing capacity of wind turbines, but the current drive train standard option for the $1.5-3$MW wind turbines is the planetary gearbox [7].

The most common planetary gearbox offset for wind turbines is one or two planetary stages with a helical stage at the end of the drive train. Planetary gearing systems exhibit higher power densities than parallel axis gears and offer a multitude of gearing options that allow significant changes in rotational speed with a small volume [8]. Different operating and lubrication conditions are to be found between the different stages of the gearbox and their weight on the torque loss of a planetary multiplier gearbox is not yet fully understood.

Mechanical energy is transmitted with high efficiencies when compared with other forms. In the overall power losses of a wind turbine the losses related to the gearbox represent a minor role. As so, the *war* on gear efficiency improvement is seen by many as a war that is no longer worth fighting for. Nevertheless, in a three stage gearbox used in a 1MW wind turbine, an improvement of 0.33% per gear stage leads to an overall efficiency improvement of 1% which represents an energy gain of 10kW. The average household energy consumption world wide for 2011 was 3338kWh, [9], representing 0.93kW per household. This means that such a slight improvement as 0.33% would allow each wind turbine to supply ten extra households. As little as it may seem, taking into account all the already existent wind farms with wind turbines usually with a capacity ranging $1.5-3$MW, the slight improvements on a the efficiency of a gearbox should not be neglected.

In a gearbox operating at or near nominal operating conditions the main energy dissipation sources are the gears and the rolling bearings [10, 11].

In order to improve gearbox efficiency one can then act to improve the gears and rolling bearings efficiency. This can be achieved by simply changing to a more efficient gear design [12] or changing the rolling bearings type [11].

Despite being an effective way to improve the efficiency of a gearbox, changing the components is usually only a viable option at the design stage. Nevertheless, for gearbox units that are already installed there's still an option which is changing to a lubricating fluid that promotes less friction between the contacting bodies.

Fernandes *et al.* [13, 14, 15, 16] and Marques *et al.* [17] have already shown that is possible to obtain important efficiency gains in gears and rolling bearings by changing between different formulations of wind turbine gear oils.

The work presented in this dissertation comes as a follow up of previous works that aimed to study the influence of wind turbine gear oils in gearbox efficiency.

Gonçalves [1] and Marques [2] have done their studies in a parallel axis gearbox with helical gears (3rd stage in a wind turbine gearbox) and more recently Pereira [3] has done a similar work in a planetary gearbox with helical gears at low loads.

The aim of this work is then to study the influence of different wind turbine gear oil formulations in the efficiency of a planetary gearbox with helical gears at high loads and low speeds (1st and 2nd stages in a wind turbine gearbox).

1.1. Thesis Outline

This dissertation is divided in five parts.

The first part deals with the presentation and measurement of some of the properties of the wind turbine gear oils properties and techniques that were used. The gearbox test rig and tested planetary gearbox are also presented as well as the planing of the efficiency tests and the experimental procedure. The ferrography techniques that were used to verify the gear oils wear performance are also presented.

The second part is dedicated to describe and present the power loss model for planetary gearboxes. The derivation of the static loads and kinematics is shown. Some considerations regarding the power loss and dissipated heat at stabilized operating conditions are also done.

The third part introduces the experimental results that were obtained. These results are analysed in detail and comparisons with the numerical predictions are done. This part also introduces the results that were obtained after some additional tests were done in order ascertain certain specifics of the experimental results.

The forth and last Part of the main text is dedicated to the final conclusions of this work and future work suggestions.

The last section of this dissertation consist of a compilation of the test sheets with the results of the efficiency tests and some numerical and experimental results that were not in the main text.

Part I.

Materials and Methods

2. Selected Lubricants

Wind turbine lubricants need to last as long as possible, offering excellent oxidation and shear stability, whilst protecting key turbine components such as main bearings from failure, and gears from micropitting [18].

Four fully formulated ISO VG 320 wind turbine gear oils were selected, two of them being mineral based oils (MINR and MINE) and the other two being synthetic based oils: a poly$-\alpha-$olefin (PAOR) and a polyalkylene glycol (PAGD).

The chemical composition and the physical properties of the selected oils were listed in the manufacturer's data sheets. Nevertheless, a few measurements regarding the physical properties were carried out in order to confirm the data given by the manufacturers and to have a higher accuracy in the lubricant properties and behavior.

2.1. Techniques and devices used

2.1.1. Engler viscometer

To measure the viscosity of the selected lubricants an Engler viscometer was used, which consists of two containers, one inside another, supported by a three legged adjustable support.[19]

The desired fluid is placed in the inner container which has a hole on the bottom. A wood pointer is used to close or open the hole, in order to stop or allow the fluid flow. The space between the inner and outer container is filled with thermal fluid. The containers are heated by an electrical resistance and the temperature of each fluid is controlled with a thermometer [20].

The measurement procedure followed the IP 212/92 standard [19]. Figure 2.1a shows the Engler viscometer used to measure the viscosity of the tested oils.

2.1.2. Density meter

In order to measure the variation of density of the tested oils at atmospheric temperature a density meter was used.

The density meter used, figure 2.1b, collects a 2ml sample and measures the density of a fluid in a range of temperatures between 0 and 40°C. The density of each oil sample was measured at three different temperatures so that the thermal expansion coefficient was determined [21], allowing the calculation of each oil's density at a given temperature.

(a) Engler viscometer. (b) Anton Paar DM A35N density meter.

Figure 2.1.: Devices used.

2.2. Lubricant properties

The kinematic viscosity variation with temperature calculation followed the standard ASTM D341 [20]. For the four tested gear oils, the viscosity variation with temperature is shown in figure 2.2.

It is possible to observe that at 40°C the gear oils have similar viscosity except for PAGD, which is lower. With temperature increase, the viscosity decreases, being the MINR the oil with the highest variation and PAGD being the lowest. MINE and PAOR show a very similar behavior for the considered range of temperatures. This behaviors are easily related to the viscosity index. In table 2.1 is possible to observe that MINR has the lowest viscosity index while PAGD has the highest. MINE and PAOR have similar viscosity index and the same viscosity at 40°C thus showing a very similar behavior.

The density variation with temperature is shown in figure 2.3.

All oils show a linear decrease of density with increasing temperature. It is to be noticed that PAGD has a range of density considerably higher than all the other oils, having a higher density than water for temperatures below 90°C.

The selected oils were already used in previous works [1, 2, 3]. The chemical composition and the physical properties are presented in table 2.1.

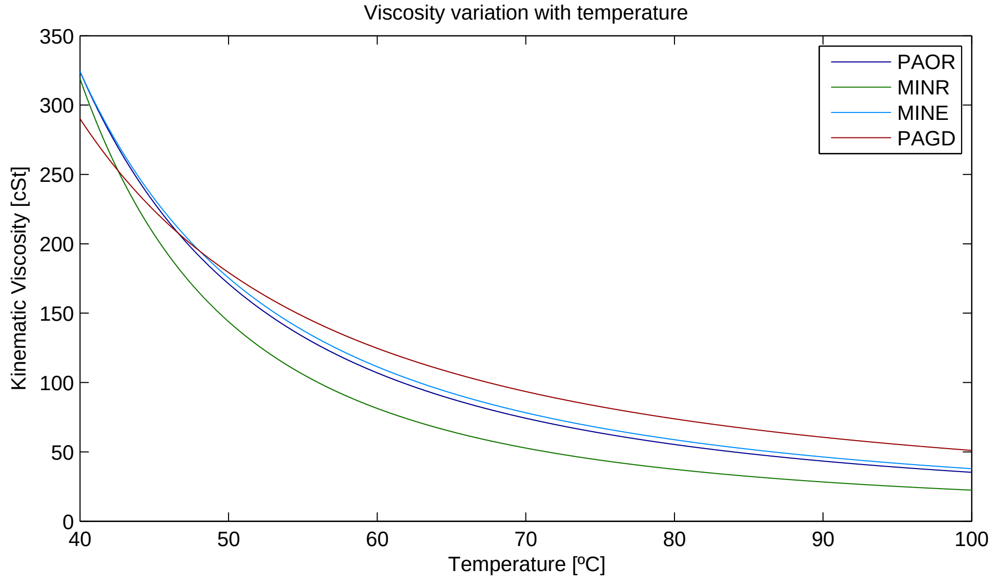

Figure 2.2.: Tested oils' viscosity variation with temperature (ASTM D341).

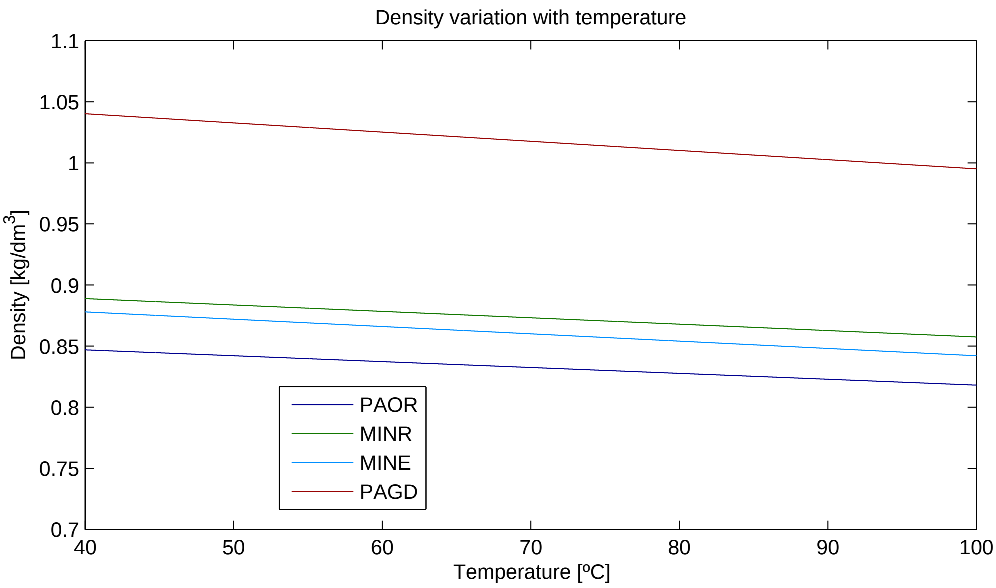

Figure 2.3.: Tested oils' density variation with temperature.

Table 2.1.: Chemical composition and physical properties of the tested lubricants.

	MINR	PAOR	MINE	PAGD
Base oil:	Mineral	Poly−α−olefin	Mineral +40% PAMA	Polyalkalene Glycol
		Chemical composition		
Zinc (Zn) [ppm]	0.9	<1	3.5	1.0
Magnesium (Mg) [ppm]	0.9	<1	0.5	1.4
Phosphorus (P) [ppm]	354.3	460	415.9	1100
Calcium (Ca) [ppm]	2.5	2	0.5	0.8
Boron (B) [ppm]	22.3	36	38.4	1.0
Sulfur (S) [ppm]	11200	6750	5020	362
		Physical properties		
Density @ 15°C [g/cm^3]	0.902	0.859	0.893	1.059
Thermal expansion coefficient x 10^{-4} [K^{-1}]	-5.8	-5.6	-6.7	-7.1
Viscosity @ 40°C [cSt]	319.25	324.38	324.38	290.26
Viscosity @ 70°C [cSt]	65.87	87.92	92.72	102.33
Viscosity @ 100°C [cSt]	22.41	35.27	37.88	51.06
Viscosity Index	85	155	166	241

In terms of chemical composition, the biggest differences are in the phosphorous, boron and sulfur values of PAGD when compared to the other oils. PAGD has more than twice the amount of phosphorus, while having values dozen of times lower of sulfur and boron. Phosphorus, boron and sulfur are known to be used in the chemical composition of the gear oils as extreme pressure additives.

3. Testing gearbox efficiency

3.1. Test rig

The gearbox test rig works on a back-to-back configuration with recirculating power. Two sets of helical gears, represented by number 2 and 7 on figure 3.1, are used in order to recirculate the power. Both sets are lubricated by oil injection.

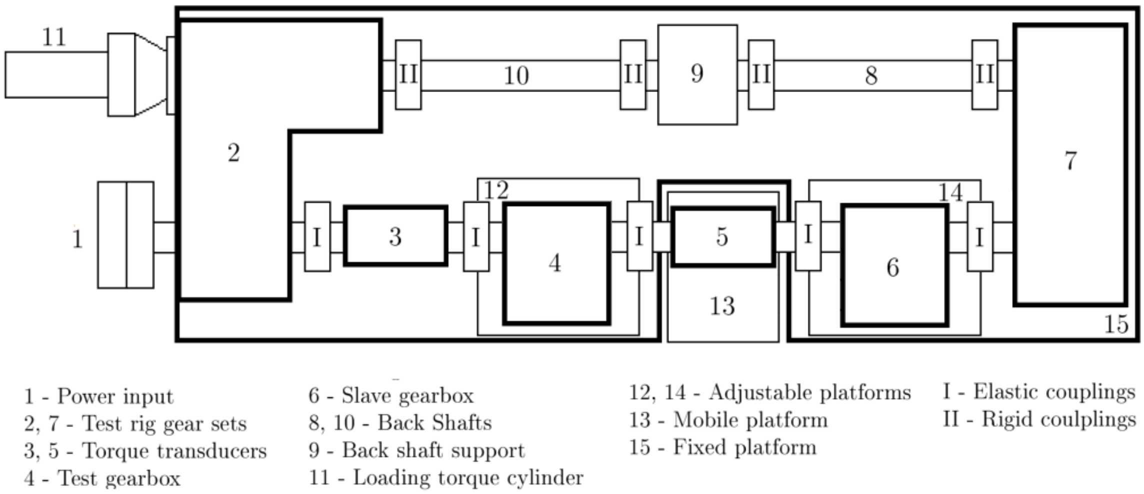

Figure 3.1.: Top view diagram of the gearbox test rig.

The test and slave gearbox, numbers 4 and 6, work on a back-to-back configurations, matching the input speed of one gearbox with the output speed of the other. Thus, only reversible gearboxes can be tested.

The test rig is able to test gearboxes with asymmetrical geometries, due to the adjustable platforms (12 and 14). The torque transducer (5) placed between the test and slave gearboxes can have its height and depth adjusted by the mobile platform (13).

The test rig and the back to back configuration of the gearboxes is presented in figure 3.2.

The torque loading mechanism consists of a hydraulic cylinder that introduces an axial displacement on one of the helical gears of the gear set 2. The axial displacement forces the wheel to slightly rotate, creating a torsional displacement in the test rig components and so loading it with a static torque.

The rotational speed of the electric motor and the torque on the torque transducer (5) are set on the central control, show in figure 3.3.

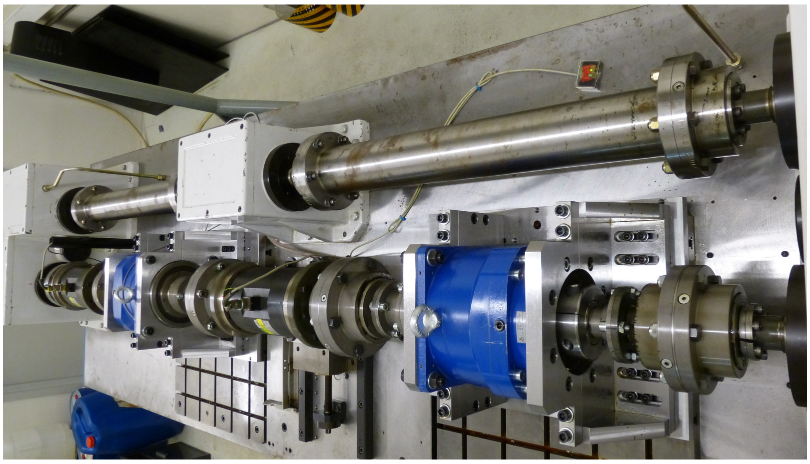

(a) Test rig.

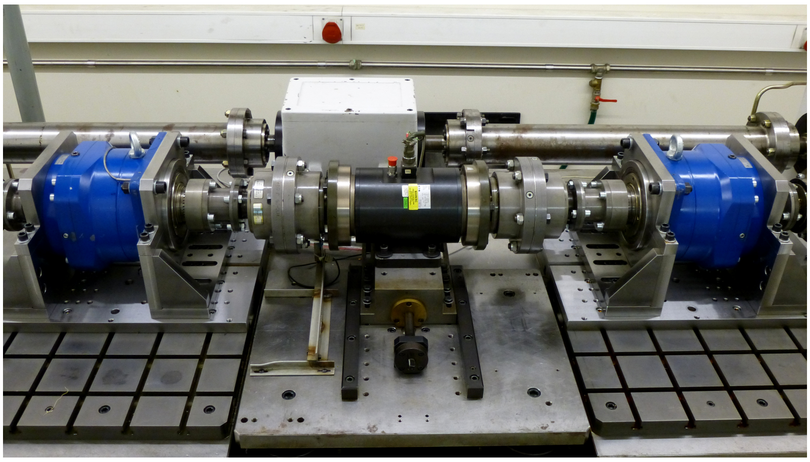

(b) Back-to-back configuration.

Figure 3.2.: Photographs of the test rig.

Figure 3.3.: Central control.

On it's current configuration, the test rig has the highest torque in between the gearboxes, which allows smoother working conditions for all the test rig. The working conditions of the test rig are the following:

- Rotational speed: $100 - 1900$rpm;
- Torque: $100 - 1300$Nm.

The torque control is done in the torque transducer (5) which is located between both gearboxes. The gearboxes setup is so that the highest torque only happen in between gearboxes, allowing to test higher loads without submitting the rest of the test rig to those loads. Therefore, the rest of the test rig operates at lower loads, but higher speeds, which is also beneficial for the motor speed control.

In order to assess the working temperatures, the test rig is equipped with several sensors, some of which were installed in the test gearbox. The sensors are measuring:

- The oil temperature in two different zones (industrial grade PT100 RTD's);
- The wall temperature (industrial grade PT100 RTD's);
- The ambient temperature;
- The room temperature.

A photograph of the gearbox instrumented with the three temperature sensors is shown in figure 3.4

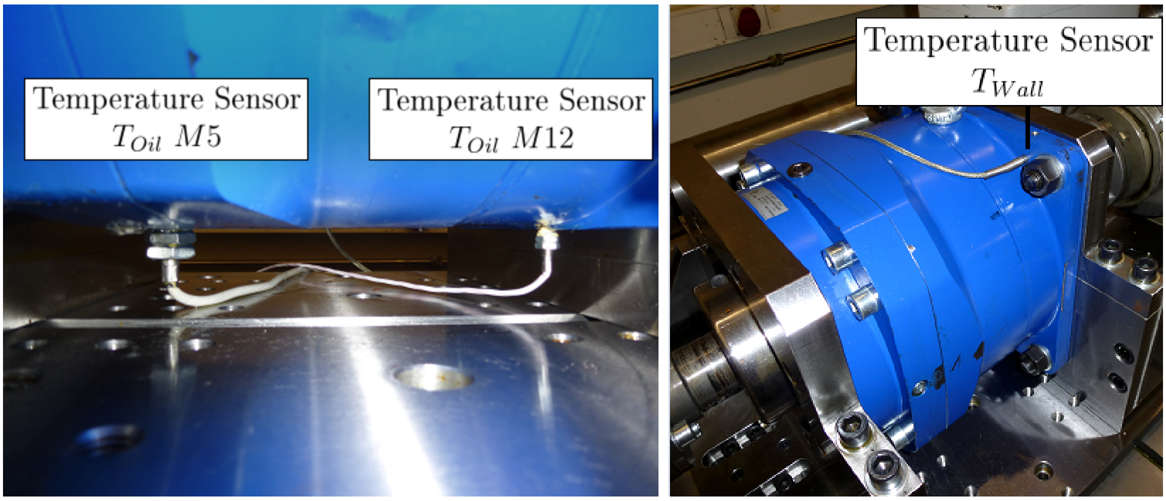

(a) Oil temperature sensors. (b) Wall temperature sensor.

Figure 3.4.: Temperature sensors' positioning in the tested gearbox.

The input and output torque as well as rotating speeds were also constantly measured and recorded overtime.

3.2. Planetary gearbox

The selected gearbox is a planetary multiplier with a transmission ratio of 4 and with a nominal input speed of 1000rpm and a nominal output torque of 2500Nm.

The tested planetary gearbox was partially disassembled (details shown in figures 3.5a, 3.5b and 3.5c) and therefore some of the components of the gearbox could be listed. The access to other components, such as the needle and the tapered bearings, was not possible and so this components are estimated based on the size and dimension of the gearbox, the shaft diameter and on the scheme presented in the manufacturer's catalog, figure 3.6.

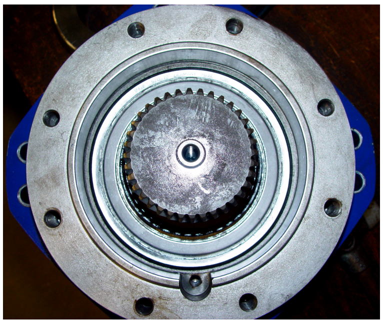

(a) Sun gear.

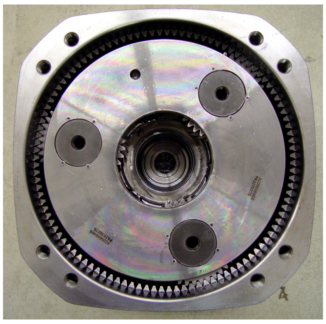

(b) Planet carrier assemble.

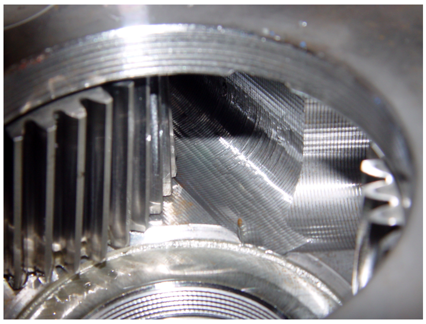

(c) Detail of the planet.

Figure 3.5.: Photographs of the tested gearbox.

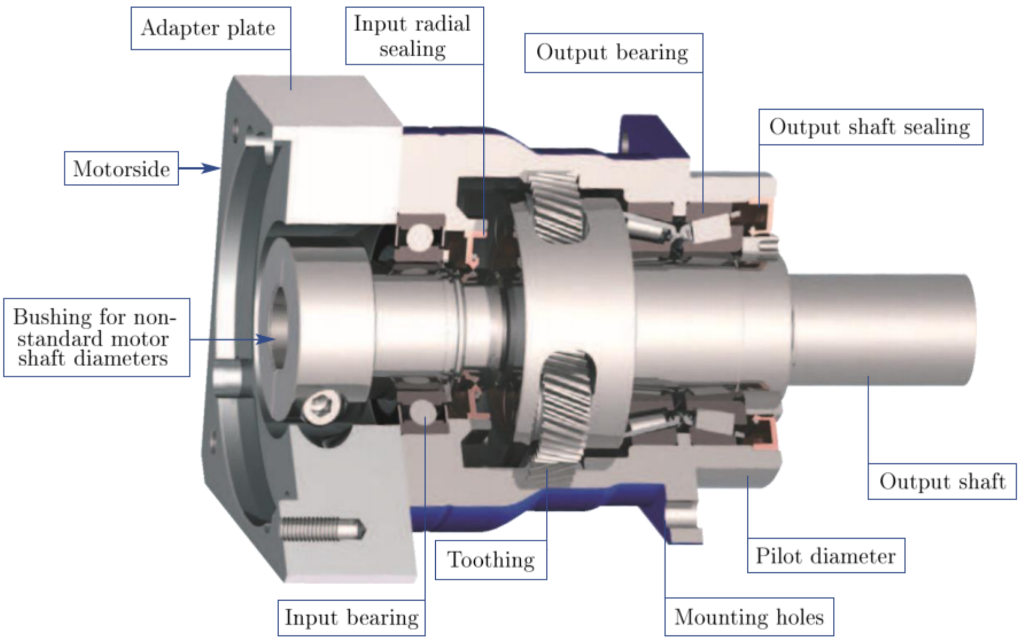

Figure 3.6.: Scheme of the planetary gearbox.

The geometrical characteristics of the gears are listed in table 3.1.

The gearbox rolling bearings are listed in table 3.2. While disassembled it was possible to see that the deep grove ball bearing is shielded and contains it's own lubricant. Although the tapered rolling bearings were not visible, it was assumed that they are equally shielded and contain their own lubricant as well.

Table 3.1.: Geometrical characteristics of the planetary gearbox.

	Sun	**Planet**	**Ring**
Number of teeth [/]	36	36	-108
Profile shit coefficient [mm]	-0.0189	-0.0189	0.0566
Reference diameter [mm]	73.1101	73.1101	-219.332
Base diameter [mm]	68.577	68.577	-205.731
Tip diameter [mm]	77.035	77.035	-215.106
Width [mm]		42	
Pressure angle [°]		20	
Working transverse pressure angle [°]		20.122	
Helix angle [°]		10	
Normal module [mm]		2	
Center distance [mm]		73.111	
Working center distance [mm]		73.035	

Table 3.2.: Rolling bearings and seals in the planetary gearbox.

Component	**Quantity**	**Designation**
Tapered roller bearings	2	32022 X/Q *
Deep groove ball bearing	1	6217-2Z
Input and output seal	2	BAUM6 SLX7 140-170-13/12 CFW A1
Needle roller bearing	6	K 40x48x20*

$*$ – Estimated

3.3. Tests planning

In order to fully understand the influence of the operating conditions on the torque loss behavior of the gearbox, a 16 test grid was planned, comprising 4 different loads (1600/2000/2400/2800Nm) and 4 different speeds (100/150/200/250rpm). The operating conditions of the 16 test grid were selected according to the working conditions allowed by the test rig and according to the planetary gearbox specifications. From that grid, 5 tests were selected trying to meet the working conditions of one the stages of a gearbox used in wind turbines in terms of Hertz pressure and tangential speed.

The Hertz pressure is essentially function of the load while the tangential speed is function of the rotational speed. The contact pressure and the tangential speed resulting from the imposed working conditions on the test gearbox are represented in table 3.3, and the contact pressure and the tangential speed of the gearboxes used in wind turbine are represented in table 3.4. The full planning of tests is shown in table 3.5. The speed and torque mentioned are the ones measured in between gearboxes, see figure 3.1.

Table 3.3.: Tangential speed and Hertz Pressure in the test gearbox.

Imposed rotational speed [rpm]	**Tangential speed** [m/s]	**Imposed torque** [Nm]	**Hertz pressure** [N/mm^2]
100	1.15	1600	955.0738 (SP)
			646.1703 (PR)
150	1.72	2000	1063.6336 (SP)
			719.9055 (PR)
200	2.30	2400	1165.3512 (SP)
			785.9340 (PR)
250	2.87	2800	1249.1650 (SP)
			846.1466 (PR)

SP – Sun-Planet contact

PR – Planet-Ring contact

Table 3.4.: Tangential speed and Hertz Pressure in gearboxes used in wind turbines.

Gear Stage	**Tangential Speed** [m/s]	**Hertz pressure** [N/mm^2]
1st Stage	1.63	1381.769 (SP)
		987.743 (PR)
2nd Stage	5.49	2873.516 (SP)
		2029.198 (PR)

SP – Sun-Planet contact

PR – Planet-Ring contact

Table 3.5.: Experimental test plan.

Oil	Speed [rpm]	Torque [Nm]	Power [W]	Test time [min]
PAOR	100	1600	16755.2	240 + 90
		2000	20944.0	240 + 90
		2400	25132.7	240 + 90
		2800	29321.5	240 + 90
	150	1600	25132.7	240 + 90
		2000	31415.9	240 + 90
		2400	37699.1	240 + 90
		2800	43982.3	240 + 90
	200	1600	33510.3	240 + 90
		2000	41887.9	240 + 90
		2400	50265.5	240 + 90
		2800	58643.1	240 + 90
	250	1600	41887.9	240 + 90
		2000	52359.9	240 + 90
		2400	62831.9	240 + 90
		2800	73303.8	240 + 90
PAOR/MINR/MINE/PAGD	100	2800	29321.5	240 + 90
	150	2000	31415.9	240 + 90
		2400	37699.1	240 + 90
		2800	43982.3	240 + 90
	200	2800	58643.1	240 + 90

3.4. Experimental procedure

The duration of each test was five hours and thirty minutes. During the first four hours the test gearbox worked as a multiplier, and in the other one and a half hour worked as a reducer. The duration of both parts of the test was set in order to achieve stabilized operating conditions: load, speed and temperatures.

The ventilation of the room where the test rig works doesn't have enough power to guarantee a stabilized room temperature. Nevertheless, the power losses are function of a temperature difference, which achieved reasonably stable values.

The values read by the sensors were automatically recorded by the central control with a frequency of 0.5Hz. The calibration of the torque transducers was checked periodically in order to assure proper function.

The behavior of various metrics, such as torque, speed and temperature, were displayed in the central control over time, to allow a fast detection and intervention of any abnormal variation on the behavior of the test rig.

An oil sample was collected from the test gearbox when appropriate, being collected a total of 8 samples. The samples are shown in figure 3.7b and the working conditions that preceded the sample collection are represented in table 3.6.

Table 3.6.: Oil samples collected.

Test Grid	Oil Sample	Tests performed
16 PAOR	PAOR_100	100rpm; 1600/2000/2400Nm;
	PAOR_150	150rpm; 1600/2000/2400Nm;
	PAOR_200	200rpm; 1600/2000/2400Nm;
	PAOR_250	250rpm; 1600/2000/2400Nm;
	PAOR_2800	100/150/200/250rpm; 2800Nm;
5 Test Grid	MINR_5	Full test grid
	MINE_5	Full test grid
	PAGD_5	Full test grid

Each oil sample was collected through the top gearbox plug's hole, using a vacuum pump, figure 3.7a. All oil samples were collected immediately at the end of a given test, in the interest of avoiding particle deposition at the bottom of the gearbox and to guarantee that the sample is representative of the oil's condition.

There was no fresh MINE oil available, so it was also taken an oil sample of MINE oil before it was introduced in the gearbox, to serve as a point of comparison.

The last test in the 16 PAOR test grid (250rpm; 2800Nm) showed an abnormal increase of the oil temperature and the test was aborted at 15min to it's end. Therefore, the tested gearbox was open and it was found that one of the seals was no longer sealing. The ball bearing of the tested gearbox was therefore being lubricated with oil instead of grease. The test and slave gearbox changed places, and several

(a) Vacuum pump. (b) Oil samples.

Figure 3.7.: Vacuum pump and oil samples.

tests were conducted. The repeatability of the test was assured, and the remaining planned tests were performed.

The gearboxes' oil was always changed at the same time. The oil was drained through a plug in the bottom and then the gearboxes were filled with petroleum ether, except for PAGD which was first flushed with an ISO VG320 ester oil and with a special solvent afterward. While the gearboxes were filled with solvent, the test rig was manually rotated for several minutes aiming to remove the maximum amount of remaining oil and wear particles. The solvent was removed the same way as the oil, and then the gearboxes were left to dry for 12h and then filled with 1litre of fresh lubricant.

4. Analysis techniques

The oil samples were analyzed using a set of techniques called ferrography which are normally used to monitor the wear evolution over time and diagnose the causes of certain failures in mechanical components lubricated with oil or grease. Using this technique the quantity and the morphology of the wear particles suspended in the oil sample can be analyzed allowing an evaluation of the wear performance of a lubricant. It can also be used to perform preventive maintenance and to predict the failure of a component in a mechanism.

Two different methods were used: direct reading ferrography (DRIII) and analytic ferrography (FMIII).

4.1. Direct Reading Ferrography (DRIII)

A direct reading ferrograph (figure 4.1) allows a rapid and objective quantification of large and small particles in an oil sample.

Figure 4.1.: Direct reading ferrograph by *Predict Technologies*.

One milliliter of oil circulates through a capillary tube which has a section submitted to a strong magnetic field and two beams of light. The solid particles lodge along the tube due to the magnetic field or simply by sedimentation. The larger will deposit first, as they are heavier and suffer greater influence of the magnetic field, followed by those of smaller dimension.

One of the beams of light is located at the beginning of the measuring section, and the other at the end. The amount of light that crosses the tube is limited by the amount and size of the particles that are deposited and so, the first beam of light will be limited by the larger particles and the second by the smaller ones.

Two values are obtained by the direct reading ferrograph: D_L and D_S which represent the relative quantity of the larger and smaller particles in the oil sample. This values are then used to calculate the index of *Wear Particles, CPUC* (equation 4.1.1) and the index of *Wear Severity, ISUC* (equation 4.1.2).

$$CPUC = \frac{D_L + D_S}{d} \tag{4.1.1}$$

$$ISUC = \frac{D_L^2 - D_S^2}{d^2} \tag{4.1.2}$$

Where d is the dilution factor which is used in cases of excessive particles which causes saturation of the sensors.

4.2. Analytic ferrography (FMIII)

Analytic ferrography is used to obtain detailed information about particles in the oil sample. The oil is forced to flow ate a very slow speed between the two edges of a thin glass slide, which is called a ferrogram. A magnet located bellow the ferrogram causes the ferrous particles to deposit. The particles will deposit accordingly to their sizes due to the effect of the magnetic field, figure 4.2.

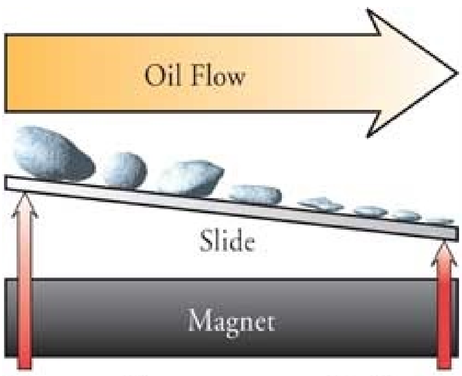

Figure 4.2.: Sedimentation process of the particles in the ferrogram [22].

The ferromagnetic particles will deposit perpendicularly arranged relatively to the oil flow.

Although this method is particularly useful on detecting ferrous particles, other particles such as aluminum and copper particles can also deposit in the ferrogram as they can get trapped between ferrous particles or they may acquire magnetism from the contact with ferrous particles. Other particles such as contaminants, fibers and products resulting from oxidation will randomly deposit along the ferrogram due to the force of gravity.

Ferrograms are made of heat resistant glass, which allows heat treatments that can help to estimate the composition of the metallic particles, in particular the ferrous ones.

To prepare the ferrograms was used an analytic ferrograph, model FM-III-Ferrograph by *Predict Technologies*, figure 4.3a. The ferrograms were observed using a Ferroscope - IV, figure 4.3b.

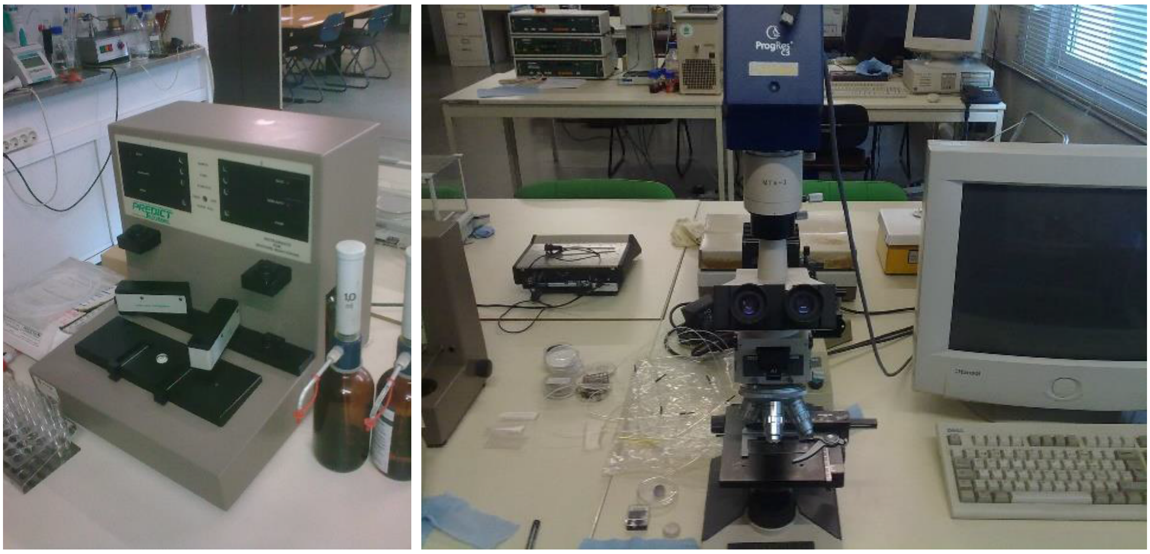

(a) Analytic ferrograph (FMIII). (b) Ferroscope - IV.

Figure 4.3.: Devices used in analytic ferrography, both by *Predict Technologies*.

Part II.

Numeric Model

5. Planetary gearbox: Loads, Kinematics and Power Loss

5.1. Load analysis

The load dependent power loss calculation requires the determination of the loads acting in each contacting component. The static load analysis is presented in the following paragraphs. A schematic representation of a planetary gear is shown in figure 5.1. The different components were labeled with numbers and the main points were labeled with letters, in order to keep simple the load and kinematic equations. Forces of inertia, moments of inertia and gravity forces were neglected. The ring is the fixed element.

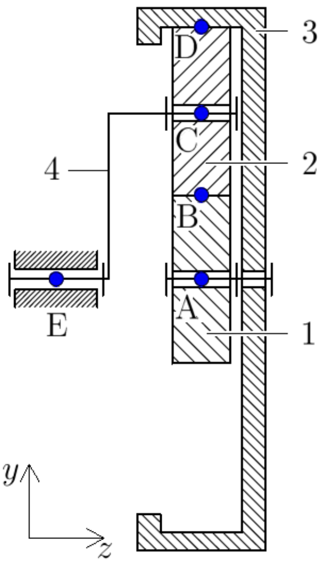

Figure 5.1.: Schematic representation of the planetary gear (side view).

The free body diagram of the planet carrier is shown in figure 5.2, considering the torque input being through the planet carrier.

The load F_{24} is determined with equation (5.1.2).

$$\sum M_E = 0 \tag{5.1.1}$$

$$F_{24} = \frac{\frac{M_{mot}}{N}}{a} \tag{5.1.2}$$

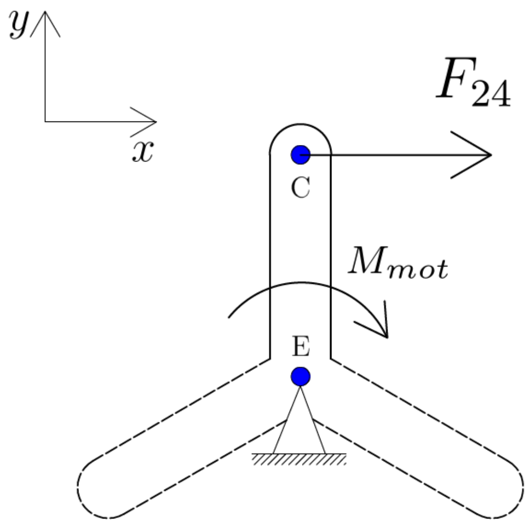

Figure 5.2.: Free body diagram of the planet carrier.

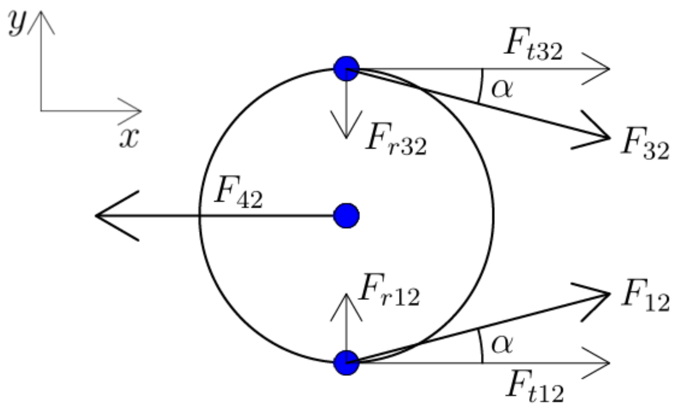

Figure 5.3.: Free body diagram of the planet.

Where N is the number of planets of the gearbox and a is the center distance, which is the same for the sun/planet gears and the planet/ring gears. Since the gearbox in study has 3 planets, $N = 3$ will be assumed.

The free body diagram of a planet is represented in figure 5.3.

The force balance equation of the planet is written as following:

$$\sum \vec{F} = \overrightarrow{F_{42}} + \overrightarrow{F_{32}} + \overrightarrow{F_{12}} \tag{5.1.3}$$

Where:

$$\overrightarrow{F_{12}} = \overrightarrow{F_{t12}} + \overrightarrow{F_{r12}} \tag{5.1.4}$$

$$\overrightarrow{F_{32}} = \overrightarrow{F_{t32}} + \overrightarrow{F_{r32}} \tag{5.1.5}$$

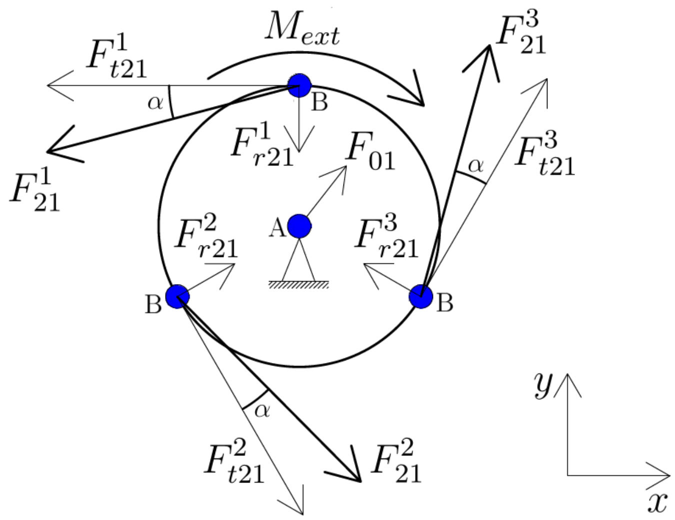

Figure 5.4.: Free body diagram of the sun.

Considering the Cx axis it is possible to write that:

$$\sum F_x = 0 \Leftrightarrow \tag{5.1.6}$$

$$\Leftrightarrow F_{42} = F_{t12} + F_{t32} \tag{5.1.7}$$

And on the Cy axis:

$$\sum F_y = 0 \Leftrightarrow \tag{5.1.8}$$

$$\Leftrightarrow F_{r12} = F_{r32} \tag{5.1.9}$$

Therefore:

$$F_{t12} = F_{t32} = \frac{-F_{42}}{2} \tag{5.1.10}$$

$$|F_{r12}| = |F_{r32}| = |F_{t12} \cdot \tan(\alpha_t)| \tag{5.1.11}$$

The free body diagram of the sun gear is represented in figure 5.4.

The moment balance regarding A is established according to equation (5.1.12).

$$\sum \overrightarrow{M_A} = \overline{AB^1} \cdot \overrightarrow{F^1_{t21}} + \overline{AB^2} \cdot \overrightarrow{F^2_{t21}} + \overline{AB^3} \cdot \overrightarrow{F^3_{t21}} + \overrightarrow{M_{ext}} = \vec{0} \tag{5.1.12}$$

Due to the symmetry of the sun/planet system, the equalities written in equations

(5.1.15) and (5.1.13) can be established:

$$\overline{AB^1} = \overline{AB^2} = \overline{AB^3} \tag{5.1.13}$$

$$|F_{t21}^1| = |F_{t21}^2| = |F_{t21}^3| \tag{5.1.14}$$

$$|F_{r21}^1| = |F_{r21}^2| = |F_{r21}^3| \tag{5.1.15}$$

The radial forces are equal, and due to their spatial position they cancel each other out.

Since $\overline{AB^i} = \frac{d_1}{2}$,

$$\overrightarrow{M_{ext}} = 3 \cdot \overrightarrow{F_{t21}} \cdot \frac{d_1}{2} \tag{5.1.16}$$

The reaction in A can be obtained through equation (5.1.17).

$$\sum \vec{F} = \overrightarrow{F_{21}^1} + \overrightarrow{F_{21}^2} + \overrightarrow{F_{21}^3} + \overrightarrow{F_{01}} = \vec{0} \tag{5.1.17}$$

On the Ax axis,

$$F_{01}^x - F_{t21}^1 + |\overrightarrow{F_{t21}^2}| \cdot \sin(30°) + |\overrightarrow{F_{t21}^3}| \cdot \sin(30°) = 0 \tag{5.1.18}$$

$$F_{01}^x = 0 \tag{5.1.19}$$

And on the Ay axis,

$$F_{01}^y - |\overrightarrow{F_{t21}^2}| \cdot \cos(30°) + |\overrightarrow{F_{t21}^3}| \cdot \cos(30°) = 0 \tag{5.1.20}$$

$$F_{01}^y = 0 \tag{5.1.21}$$

The axial forces can be obtained using equations (5.1.22) and (5.1.23).

$$|\overrightarrow{F_{a12}}| = |\overrightarrow{F_{t12}}| \cdot \tan(\beta) \tag{5.1.22}$$

$$|\overrightarrow{F_{a32}}| = |\overrightarrow{F_{t32}}| \cdot \tan(\beta) \tag{5.1.23}$$

The results for the forces at nominal working conditions (2500Nm and 250rpm) is presented in table 5.1.

Table 5.1.: Forces at nominal working conditions.

	Variables	Results
Tangential force [N]	$F^1_{t21}, F^2_{t21}, F^3_{t21}, F_{t32}$	5699.1
Radial force [N]	$F^1_{r21}, F^2_{r21}, F^3_{r21}, F_{r32}$	2106.3
Axial force [N]	F_{a12}, F_{a32}	1004.9

5.2. Kinematic analysis

The power losses of all the components in the gearbox are dependent of the speed at which they operate. Therefore, it is necessary a kinematic analysis in order to determine the velocities involved. In the following paragraphs the calculation method adopted is presented.

The numbers and letters used in the kinematic analysis follow the labeling presented in section 5.1. A different schematic representation of the planetary gear is show in figure 5.5.

As the gearbox will be working as a multiplier, the power input will be in the planet carrier (4). Point C belongs to the planet carrier as well as it is the geometric center of the planets. Thus, the velocity of point C calculated from one object or another must match, equation (5.2.1).

$$\overrightarrow{v_{C_{40}}} = \overrightarrow{v_{C_{20}}} \tag{5.2.1}$$

In equations (5.2.2) and (5.2.3), Mozzi's equations are used to determine the rotational speed of the planet:

$$\overrightarrow{v_{A_{40}}} + \overrightarrow{\omega_{40}} \times \overrightarrow{AC} = \overrightarrow{v_{D_{20}}} + \overrightarrow{\omega_{20}} \times \overrightarrow{DC} \tag{5.2.2}$$

Let r_i be the radius of body i. As the velocities of point A and D are null,

$$\begin{Bmatrix} 0 \\ 0 \\ \omega_{40} \end{Bmatrix} \times \begin{Bmatrix} 0 \\ r_1 + r_2 \\ 0 \end{Bmatrix} = \begin{Bmatrix} 0 \\ 0 \\ \omega_{20} \end{Bmatrix} \times \begin{Bmatrix} 0 \\ -r_2 \\ 0 \end{Bmatrix} \tag{5.2.3}$$

The planet's rotational speed is given by equation (5.2.4)

$$\omega_{20} = -\omega_{40} \cdot \frac{r_1 + r_2}{r_2} \tag{5.2.4}$$

Point B is the contact point between the sun and the planet, and therefore can be used to relate the sun velocity with the planet velocity considering that point B velocity is the same for both the planet and the sun, equation (5.2.5).

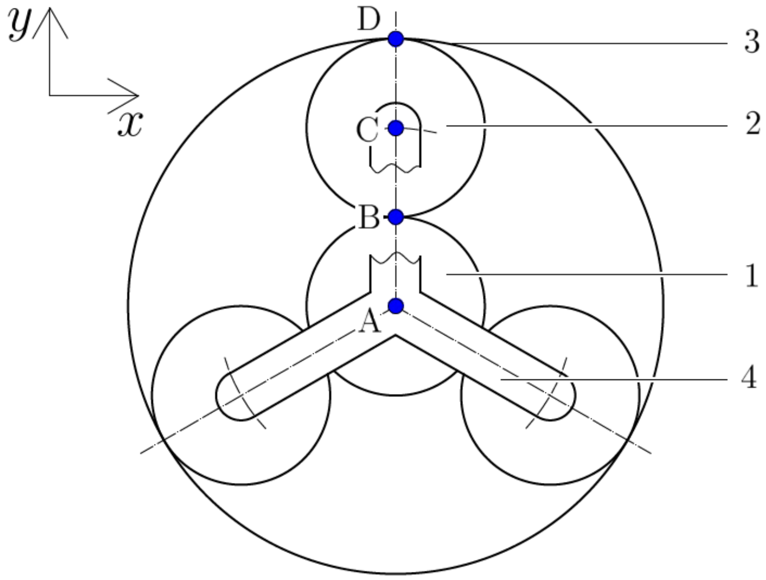

Figure 5.5.: Schematic representation of the planetary gear (front view).

$$\overrightarrow{v_{B_{10}}} = \overrightarrow{v_{B_{20}}} \tag{5.2.5}$$

In equations (5.2.6) and (5.2.7), Mozzi's equations are used to determine the rotational speed of the sun:

$$\overrightarrow{v_{A_{10}}} + \overrightarrow{\omega_{10}} \times \overrightarrow{AB} = \overrightarrow{v_{D_{20}}} + \overrightarrow{\omega_{20}} \times \overrightarrow{DB} \tag{5.2.6}$$

$$\begin{Bmatrix} 0 \\ 0 \\ \omega_{10} \end{Bmatrix} \times \begin{Bmatrix} 0 \\ r_1 \\ 0 \end{Bmatrix} = \begin{Bmatrix} 0 \\ 0 \\ \omega_{20} \end{Bmatrix} \times \begin{Bmatrix} 0 \\ -2r_2 \\ 0 \end{Bmatrix} \tag{5.2.7}$$

The sun rotational speed is given by equation (5.2.8),

$$\omega_{10} = -\omega_{20} \cdot \frac{2r_2}{r_1} \tag{5.2.8}$$

Or, in terms of the carrier rotational speed:

$$\omega_{10} = -\omega_{40} \cdot \frac{2(r_1 + r_2)}{r_1} \tag{5.2.9}$$

Considering the definition of gear normal module, equation (5.2.10):

$$m = \frac{d}{z} \tag{5.2.10}$$

and the geometric relations in a planetary gear, equation (5.2.11)

$$r_1 + 2r_2 = r_3 \tag{5.2.11}$$

it is possible to write the sun and planet rotational speed as a function of the number of teeth and the rotational speed of the carrier, equation (5.2.12) and (5.2.13):

$$\omega_{10} = \omega_{40} \cdot 2 \cdot \left(1 + \frac{z_2}{z_1}\right) = \omega_{40} \cdot \left(1 + \frac{z_3}{z_1}\right) \tag{5.2.12}$$

$$\omega_{20} = -\omega_{40} \cdot \left(1 + \frac{z_1}{z_2}\right) \tag{5.2.13}$$

Therefore, the gear ration, i, can be written as in equation (5.2.14) or in equation (5.2.15).

$$i = 1 + \frac{z_3}{z_1} \tag{5.2.14}$$

$$i = 2 + \frac{2 \cdot z_2}{z_1} \tag{5.2.15}$$

Equation (5.2.11) does not take into account the shift profile coefficents, and as a consequence, equation (5.2.14) is not valid for all cases.

The gear ratio of the test gearbox is presented in table 5.2 as well as an example of the rotational speed of the several components for the nominal working conditions (2500Nm and 250rpm).

Table 5.2.: Gear ratio and rotational speed of the gearbox components.

	Variables	**Results**
Gear ratio [-]	i	4
Carrier rotational speed [rpm]	ω_{40}	250
Planet rotational speed [rpm]	ω_{20}	-500
Sun rotational speed [rpm]	ω_{10}	1000

5.3. Introduction to the power loss in a gearbox

According to Höhn *et al.* [10], the total power loss in a gearbox is the sum of gears, bearings, seals and auxiliary losses, figure 5.6.

The gear and the roller bearing losses can be divided in load losses, associated to the transmitted power, and the no-load losses which are independent of the transmitted torque.

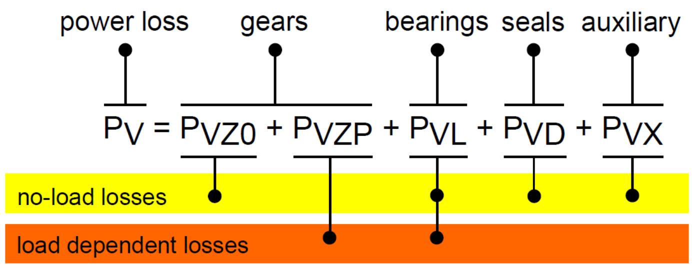

Figure 5.6.: Different power loss components in a gearbox [10].

The load losses are function of the transmitted torque, the coefficient of friction and the sliding velocity in the contact areas.

No-load losses are dependent upon the operating speed, the internal housing design, the lubricant viscosity and density, as well as the immersion depth of the gearbox components in the oil sump.

Usually, for nominal operating conditions, the dominant power losses of a gearbox are the load losses. When working at high speeds and with low or moderate loads, no-load losses can overcome the load losses.

In behalf of improving a gearbox efficiency, it is fundamental to understand how each component contributes to the total power loss and how the operating conditions and the lubricant formulation can influence each energy dissipation source.

5.4. Gears power loss

Gear losses are dependent on the transmitted power, the mean coefficient of friction and a gear loss factor. The average gear power loss is given by equation (5.4.1).

$$P_{VZP} = P_a \cdot \mu_m \cdot H_V \tag{5.4.1}$$

Where:

- P_a is the transmitted power;
- μ_m is the mean coefficient of friction (determined in section 5.4.1).
- H_V is a gear loss factor.

The transmitted power can be calculated using equation (5.4.2).

$$P_a = F_b t \cdot \omega \cdot r_b \tag{5.4.2}$$

The gear loss factor, H_V is dependent of the gear geometry and it's an indicator of the efficiency associated to a certain gear, despite the working conditions, the transmitted power and the lubricant used. Originally, H_V was obtained on the assumption that the coefficient of friction is constant along the line of action, and can be calculated according to equation (5.4.3).

$$H_V = \frac{\pi(i+1)}{z_1 \cdot i \cdot \cos(\beta_b)} \left(a_0 + a_1 \cdot |\epsilon_1| + a_2 \cdot |\epsilon_2| + a_3 \cdot |\epsilon_1| \cdot \epsilon_1 + a_4 \cdot |\epsilon_2| \cdot \epsilon_2\right) \tag{5.4.3}$$

Where:

- i is the gear ratio;
- z_1 os the number of teeth of the pinion;
- β_b is the helix angle at the base;
- ϵ_α is the profile contact ratio;
- $\epsilon_{1,2}$ are the tip contact ratios: pinion(1) and wheel(2);
- $a_{0,1,2,3,4}$ are the coefficient dependent on the tip contact ratios.

Based on ϵ_1, ϵ_2 and ϵ_α three parameters are defined:

- $\epsilon_1 \in]l_g - 1 : lg[$
- $\epsilon_2 \in]m_g - 1 : mg[$
- $\epsilon_\alpha \in]n_g - 1 : ng[$

And the $a_{0,1,2,3,4}$ can be calculated according to table 5.3.

Table 5.3.: Formulation of the coefficients a_i, $(i = 1 : 4)$.

	$\epsilon_\alpha < 1$	$\epsilon_\alpha > 1$ $\epsilon_1 < 0 \vee \epsilon_2 < 0$	$\epsilon_\alpha > 1$ $\epsilon_1, \epsilon_2 > 0$ $l + m = n$	$\epsilon_\alpha > 1$ $\epsilon_1, \epsilon_2 > 0$ $l + m = n + 1$
a_0	0	0	$\frac{2lm}{n}$	$\frac{2(lm-n)}{n-1}$
a_1	0	1	$\frac{l(l-1)-m(m-1)-2lm}{n(n-1)}$	$\frac{l(l-1)+m(m-1)-2(m-1)n}{n(n-1)}$
a_2	0	1	$\frac{-l(l-1)+m(m-1)-2lm}{n(n-1)}$	$\frac{l(l-1)+m(m-1)-2(m-1)n}{n(n-1)}$
a_3	$\frac{1}{\epsilon_\alpha}$	0	$\frac{2m}{n(n-1)}$	$\frac{2(m-1)}{n(n-1)}$
a_4	$\frac{1}{\epsilon_\alpha}$	0	$\frac{2l}{n(n-1)}$	$\frac{2(l-1)}{n(n-1)}$

Equation (5.4.3) was derived for spur gears and for a single gear pair. Despite considering the base helix angle, this equation is not suited to helical gears and the elasticity of the meshing tooth is disregarded. *KISSsoft* [8] is a software that allows the calculations of a multitude of gears (including planetary gears) considering imposed operating conditions such as input torque, speed and coefficient of friction. The contact analysis module allows the study of the gear contacts considering elastic effects. The average power loss in one of the metrics that can be calculated, therefore once the friction coefficient is imposed, equation (5.4.1) can be used to derive more accurate gear loss factors.

Table 5.4 displays the $H_V$values used.

Table 5.4.: H_V values derived from KISSsoft.

Contact	H_V factor
Sun-Planet	0.167709
Planet-Ring	0.062473

5.4.1. Friction and film thickness between gear teeth

The average coefficient of friction has a great influence in the gear mesh power loss, as can be seen in equation (5.4.1), and therefore is a major factor in what concerns to efficiency. Besides, the coefficient of friction has a direct influence on the contact temperature and failure probability.

To assess the coefficient of friction in a lubricated contact, it is necessary to begin with the calculation of the specific film thickness, which has a strong correlation with the coefficient of friction, as shown by the Stribeck curve, figure 5.7.

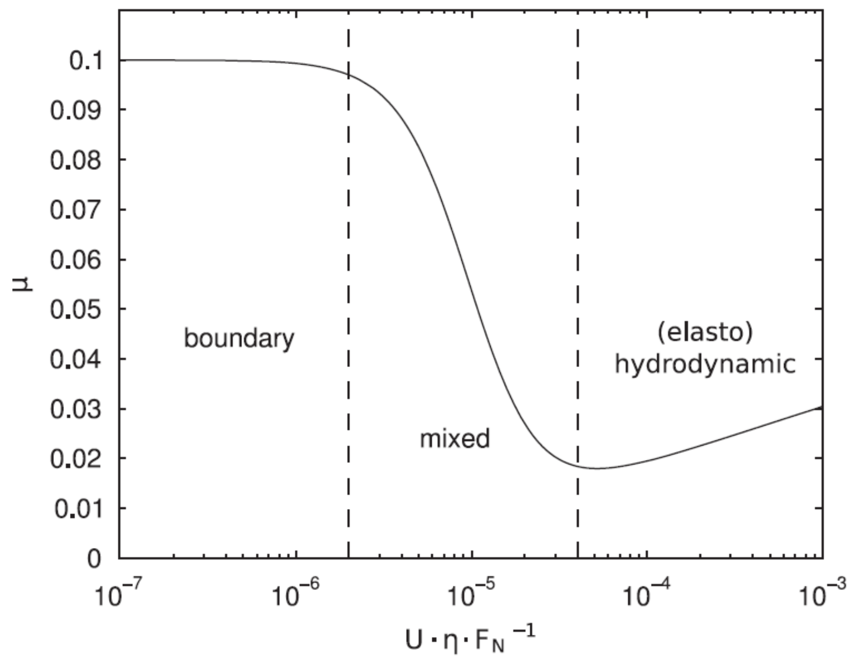

Figure 5.7.: Example of a Stribeck curve [23].

The gear teeth contact is considered to be an elastohydrodynamic (EHD) contact which, according to Dowson and Higginson [24], can be represented as in figure 5.8.

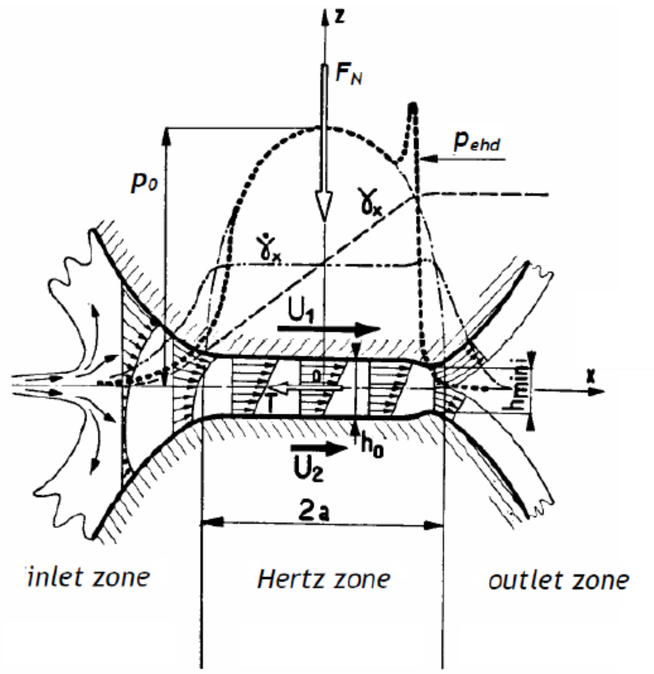

Figure 5.8.: Linear elastohydrodynamic contact [25].

The film thickness depends on:

- Viscosity of the lubricant (which depends on the temperature);
- Rolling speed;
- Piezoviscosity coefficient;
- Equivalent radius;
- Normal load;
- Width of the gear.

Classic EHD theory was derived assuming that the lubricant flow inside the contact zone is isothermal and so, the viscosity of the lubricant depends only in the contact pressure. However, this hypothesis is not valid for gears due to the high sliding along the contact line. In the inlet zone, the lubricant suffers a high shear rate strain as a result of the pressure gradient as well as the rolling and sliding speed. The shear strain causes inlet shear heating, and the lubricant flow can't be assumed as isothermal. The inlet shear heating causes an increase of the lubricant temperature, followed by a decrease in the lubricant viscosity and film thickness.

To take into account the inlet shear heating, the film thickness is multiplied by a heating correction factor, ϕ_T which depends on the lubricant thermoviscosity and thermal conductivity as well as the surface's speed.

Even so, the EHD film thickness can't be used directly as it considers the surfaces as perfectly smooth and doesn't account the surface's roughness. The ratio between the film thickness and the composite surface roughness defines the specific film thickness, Λ, which is an indicator of the lubrication regime in the contact. Table 5.5 presents a brief description of the three typical lubrication regimes, according to the specific film thickness value.

The calculation methods for the film thickness and the coeficient of friction are presented in the following paragraphs.

Film thickness

The film thickness calculation falls back on four main parameters: speed, material, load and lubricant parameter.

Speed parameter

$$U = \frac{\eta_0 \cdot (U_1 + U_2)}{2 \cdot R_x \cdot E^*} \tag{5.4.4}$$

Where:

- η_0 is the dynamic viscosity;
- $U_{1,2}$ is the velocity of each surface;
- R_x is the equivalent radius;
- E^* is the equivalent Young modulus.

Material parameter

$$G = 2 \cdot \alpha \cdot E^* \tag{5.4.5}$$

Where α is the piezoviscosity coefficient, calculated according to Gold *et al.* [27].

Load parameter

$$W = \frac{F_n}{R_x \cdot l \cdot E^*} \tag{5.4.6}$$

Where F_n is the normal force and l is the average sum of contacting lines length on a helical gear, calculated according to equation (5.4.7).

$$l = \frac{b \cdot \epsilon_\alpha}{cos\,(\beta_b)} \tag{5.4.7}$$

Lubricant parameter

$$L = \frac{\beta \cdot \ \eta_0 \cdot (U_1 + U_2)^2}{K} \tag{5.4.8}$$

Table 5.5.: EHD lubrication regimes [26].

<table>
<tr><th>Specific film thickness</th><th>Regime</th><th>Description</th></tr>
<tr><td>$\Lambda \geq 2.0$</td><td>Full film</td><td>The surfaces are completely separated by the lubricant film.</td></tr>
<tr><td colspan="3">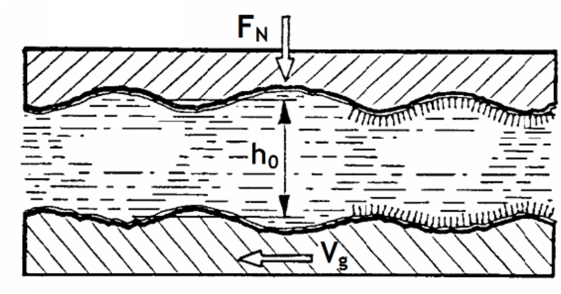
</td></tr>
<tr><td>$0.7 < \Lambda < 2.0$</td><td>Mixed film</td><td>The surfaces are partially separated by the lubricant film, there are some points where there is asperity contact.</td></tr>
<tr><td colspan="3">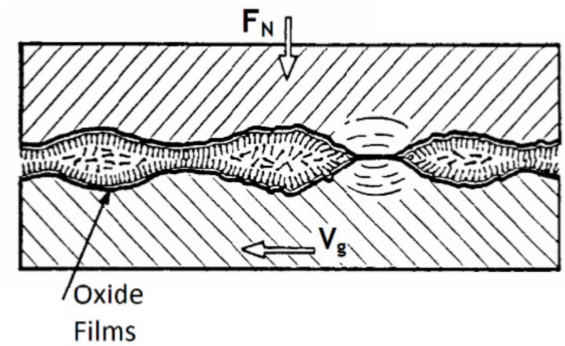
</td></tr>
<tr><td>$\Lambda \leq 0.7$</td><td>Boundary film</td><td>There is no lubricant film separating the surfaces, asperity contact dominates.</td></tr>
<tr><td colspan="3">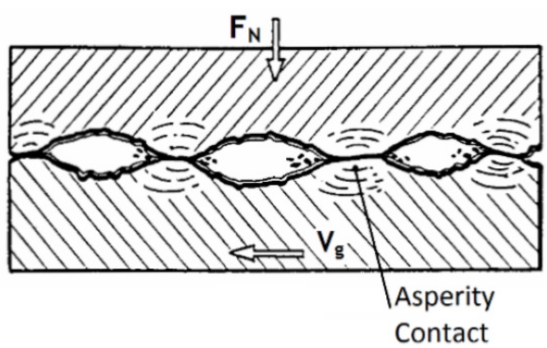
</td></tr>
</table>

Where β is the thermoviscosity coefficient (ASTM D341) and K is the thermal conductivity.

The inlet shear heating influence was calculated using equation (5.4.9).

$$\phi_T = \left(1 + 0.1 \cdot \left(1 + 1.48 \cdot V_e^{0.83}\right) \cdot L^{0.64}\right)^{-1} \tag{5.4.9}$$

The film thickness in the center of contact was calculated using equation (5.4.10).

$$h_0 = 0.975 \cdot R_x \cdot U^{0.727} \cdot G^{0.727} \cdot W^{-0.091} \tag{5.4.10}$$

The corrected film thickness was given by equation (5.4.11).

$$h_{0T} = h_0 \cdot \phi_T \tag{5.4.11}$$

Lastly, the specific film thickness was calculated using equation (5.4.12).

$$\Lambda = \frac{h_{0T}}{\sigma} \tag{5.4.12}$$

Where σ is the composite surface roughness.

Coefficient of friction

Despite the relation between specific film thickness and friction, the coefficient of friction models for gears consider an average value which is usually derived from experimental studies. One of the most well known average coefficient of friction models for gears was proposed by Schlenk *et al.* [28]. This model is simple and relies on key parameters such as operating conditions, gear geometry, surface finish and lubricant characteristics.

One of the main advantages of this model is that given a proper lubricant factor X_L it can be used to predict the average coefficient of friction between meshing tooth pair for different base oils and addictive packages. The lubricant factor for the gear oils that were selected was determined by Fernandes *et al.* [16] in an experimental work in a FZG test rig.

The Schlenk *et al.* [28] formulation for the average coefficient of friction is presented in equation (5.4.13) and table 5.6 presents the X_L factor used for the selected wind turbine gear oils.

$$\mu_{mz} = 0.048 \cdot \left(\frac{F_N}{l \cdot R_x \cdot (U_1 + U_2)}\right)^{0.20} \cdot \left(\frac{1}{\eta_0}\right)^{0.05} \cdot R_a^{0.25} \cdot X_L \tag{5.4.13}$$

Where R_a is the arithmetic mean roughness and X_L is the lubricant correction factor ($X_L = 1$ for non-additivated mineral oils in mixed film lubrication)

Table 5.6.: X_L factor for the selected oils [16].

Oil	X_L
PAOR	0.666
MINR	0.858
MINE	0.746
PAGD	0.572

5.4.2. No-load power loss

The no-load power losses in gears have been object of study by several different authors and a considerable amount of experimental and analytical studies are available. Some of the most relevant are the ones presented by Höhn *et al.* [10] and Changenet *et al.* [29, 30].

Höhn *et al.* [10] conducted an experimental study of no-load and load dependent gear power losses in cylindrical and bevel gears, as function of lubricant type and viscosity, as well as the operating load, speed and temperature, presenting a single flow regime model for the gear churning losses of a pinion/wheel.

Changenet *et al.* [29] deducted a set of equations to calculate dimensionless gear drag torque. These equations are directly influenced by the different flow regimes dependent upon a critical Reynolds number, which is related to the flow nature and to the centrifugal acceleration parameter, which in turns is related to fluid projection caused by rotating gears. Changenet *et al.* [30] shown that the internal housing geometry of a gearbox is a major influence on the churning power loss.

Other studies are available: Terekhov [31] studied the churning losses of gears with modules ranging from 2 to 8mm lubricated by high viscosity lubricants (200-2000cSt) at low speeds. Boness [32] studied churning losses of partially submerged discs and gear, in different fluids like water and oil. Seetharaman *et al.* [33] suggested a physics-based fluid mechanics model to predict spin power losses of gears due to oil churning and windage. Le Prince *et al.* [34] proposed a simplified model based on surface tension and lubricant aeration, establishing a relationship between lubricant aeration and gear churning losses.

Despite the handful of studies regarding gear churning losses, none presents an approach to the churning losses of a planetary gearbox. Planetary gearbox allow a great amount of different configurations in what concerns to the number of planets, the size of the gears and the design of the planet carrier; the gearbox housing has to keep up with the configuration of the gears and therefore can vary greatly; the fluid/geometry interactions are strongly dependent on the geometry and the multitude of possible configurations can be the the reason why there are no reliable models available for the churning losses in planetary gears.

One way of predicting the churning losses of the planetary gearbox in study would be through a computational fluid dynamics (CFD) analysis. In recent years, with the increase computational power of desktop computers, CFD is becoming a more and more attractive approach to solve the churning losses. Ideally, a simulation should consider all the geometry details and the interaction between the fluid and the geometry. The fluid/geometry interactions to include are the following:

- Interaction of the rotating sun and planet carrier with the oil sump (the interaction occurs at different speeds);
- Interaction of the rotating planets with the oil sump, considering two relative motions: the orbit of the planet towards the sun and its own rotation;
- Constant compression/expansion of volume due to the meshing gears (pocketing effects).

These phenomena occur simultaneously and they might be affected by each other. Consequently the sum of each contribution is likely to be different from the power loss of their joint effect.

Recently Concli *et al.* [35] proposed a solution for the problem of the churning power loss in a planetary speed reducer which was based on a CFD approach, with promising results.

Due to the lack of numerical models and to the complexity expected in the creation of one, the no-load losses associated to the gears were not taken into account in the presented model.

5.5. Rolling bearings power loss

To determine the power loss associated to the deep groove ball bearings and tapered roller bearings, the model presented by *SKF Rolling Bearings Catalogue 10000/1 EN* [36] was used. The bearing power loss is directly related to the frictional moment in a rolling bearing and the rotational speed of the shaft, as shown in equation (5.5.1).

$$P_{VL} = M \cdot n \cdot \frac{\pi}{30} \cdot 10^{-3} \tag{5.5.1}$$

The friction in a rolling bearing is the result of the rolling and sliding friction, which in turn are generated by the loads applied, the operating speed, as well as bearing and lubricant factors. The total friction moment combined with the operating speed determines the amount of heat generated by the bearing.

The total frictional moment was calculated using equation (5.5.2).

$$M = M_{rr} + M_{sl} + M_{seal} + M_{drag} \tag{5.5.2}$$

Where:

- M is the total frictional moment;
- M_{rr} is the rolling frictional moment;
- M_{sl} is the sliding frictional moment;
- M_{seal} is the frictional moment of seals;
- M_{drag} is the frictional moment of associated with the lubricant flow (drag, churning, splashing).

5.5.1. Rolling frictional moment

The rolling frictional moment was given by equation (5.5.3).

$$M_{rr} = \phi_{ish} \cdot \phi_{rs} \cdot G_{rr} \cdot (\upsilon \cdot n)^{0.6} \tag{5.5.3}$$

Where:

- M_{rr} is the rolling frictional moment (N·mm);
- ϕ_{ish} is the inlet shear heating reduction factor;
- ϕ_{rs} is the kinematic replenishment/starvation reduction factor;
- G_{rr} is a variable that depends on the bearing type, mean diameter, radial and axial load;
- n is the rotational speed (rpm);
- υ is the kinematic viscosity at operating temperature of the oil or the base oil viscosity of the grease (cSt).

G_{rr} is calculated differently for deep groove ball bearing and for tapered bearings, equation (5.5.4) and (5.5.5).

Deep groove ball bearing

$$G_{rr} = \begin{cases} R_1 \cdot d_m^{1.96} \cdot F_r^{0.54} & \text{if } F_a = 0 \\ R_1 \cdot d_m^{1.96} \cdot \left(F_r + \frac{R_2}{sin(\alpha_{SKF})}\right)^{0.54} & \text{if } F_a > 0 \end{cases} \tag{5.5.4}$$

Tapered roller bearing

$$G_{rr} = R_1 \cdot d_m^{2.38} \cdot (F_r + R_2 \cdot Y \cdot F_a)^{0.31} \tag{5.5.5}$$

Where:

- $R_{1,2}$ are geometric constants that depend on bearing type and series;

- Y is the axial load factor for single row bearings;
- d_m is the mean diameter;
- F_r is the radial load;
- F_a is the axial load;
- $\alpha_{SKF} = \left(\frac{F_a}{C_0}\right)^{0.24}$

5.5.2. Inlet shear heating factor

The amount of lubricant used to form a hydrodynamic film is very small. Thus, part of the oil near the contact area is rejected and forms a reverse flow, as show in figure 5.9.

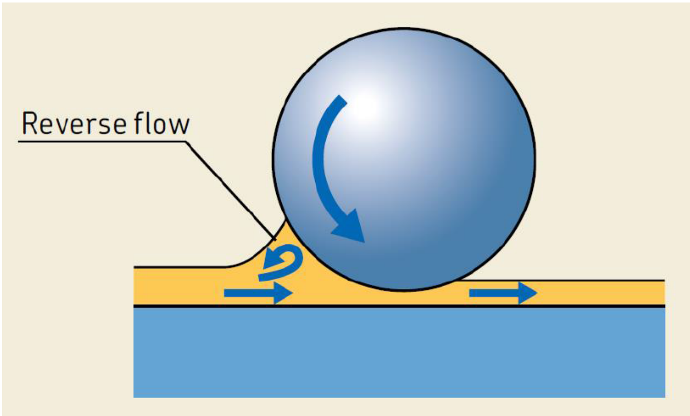

Figure 5.9.: Reverse flow in a ball bearing [36].

The reverse flow shears the lubricant generating heat. Therefore, the viscosity lowers, the film thickness is reduced and the the rolling friction decreases. The inlet shear heating reduction factor was estimated using equation (5.5.6).

$$\phi_{ish} = \frac{1}{1 + 1.84 \cdot 10^{-9} \cdot (n \cdot d_m)^{1.28} \cdot \upsilon^{0.64}} \tag{5.5.6}$$

5.5.3. Kinematic replenishment/starvation reduction factor

When high speeds or high viscosity are involved, the lubricant may not have enough time to replenish the raceways, causing a "kinematic starvation" effect, which reduces the film thickness and rolling friction.

The kinematic replenishment/starvation factor was estimated using equation (5.5.7).

$$\phi_{rs} = \frac{1}{e^{K_{rs} \cdot \upsilon \cdot (d+D) \cdot \sqrt{\frac{K_z}{2 \cdot (D-d)}}}} \tag{5.5.7}$$

Where:

- ϕ_{rs} is the kinematic replenishment/starvation reduction factor;
- K_{rs} is the kinematic replenishment/starvation constant: for low level oil bath and oil jet lubrication $K_{rs} = 3 \cdot 10^{-8}$ and for grease and oil-air lubrication $K_{rs} = 6 \cdot 10^{-8}$;
- K_z is a geometric constant related to bearing type;
- v is the kinematic viscosity at operating temperature of the oil or the base oil viscosity of the grease (cSt).
- n is the rotational speed (rpm);
- d is the bearing bore diameter;
- D is the bearing outside diameter.

According to the online SKF bearing calculator (REF1), for a tapered roller bearing 32022X/Q, equation (5.5.7) is only valid for a oil level bellow 7.525mm. If this does not verify, $\phi_{rs} = 1$.

5.5.4. Sliding frictional moment

The sliding frictional moment was given by equation (5.5.8).

$$M_{sl} = G_{sl} \cdot \mu_{sl} \tag{5.5.8}$$

Where:

- M_{sl} is the sliding frictional moment;
- G_{sl} is a variable dependent on the bearing type, mean diameter, radial and axial load.
- μ_{sl} is the sliding friction coefficient.

G_{sl} was calculated differently for deep groove ball bearing and for tapered bearings, equation (5.5.9) and (5.5.10).

Deep groove ball bearing

$$G_{sl} = \begin{cases} S_1 \cdot d_m^{-0.26} \cdot F_r^{\frac{5}{3}} & \text{if } F_a = 0 \\ S_1 \cdot d_m^{-0.145} \cdot \left(F_r^5 + \frac{S_2 \cdot d_m^{1.5}}{\sin(\alpha_F)} \cdot F_a^4\right)^{\frac{1}{3}} & \text{if } F_a > 0 \end{cases} \tag{5.5.9}$$

Tapered roller bearing

$$G_{sl} = S_1 \cdot d_m^{0.82} \cdot (F_r + S_2 \cdot Y \cdot F_a) \tag{5.5.10}$$

Where $S_{1,2}$ are geometric constants for sliding frictional moments.

The sliding friction coefficient for full-film and mixed lubrication conditions can be estimated using equation (5.5.11).

$$\mu_{sl} = \phi_{bl} \cdot \mu_{bl} + (1 - \phi_{bl}) \cdot \mu_{EHL} \tag{5.5.11}$$

Where:

- ϕ_{bl} is a weighting factor for the sliding friction coefficient;
- μ_{sl} is the sliding friction coefficient;
- μ_{bl} is a friction coefficient dependent on the additive package of the lubricant, generally $\mu_{bl} = 0.15$.
- μ_{EHL} is the sliding frictional coefficient in full-film conditions:

  0.02 for cylindrical roller bearings;

  0.002 for tapered roller bearings;

  other bearings: 0.05 for mineral oils and 0.04 for synthetic oils.

The weighting factor, ϕ_{bl}, can be estimated using equation (5.5.12).

$$\phi_{bl} = \frac{1}{e^{2.6 \cdot 10^{-8} \cdot (\upsilon \cdot n)^{1.4} \cdot d_m}} \tag{5.5.12}$$

5.5.5. Drag Losses

Drag losses occur when a bearing is rotating in an oil bath and, in most cases, their contribution to the total power loss is representative enough to not be neglected. Drag losses are dependent on several factors: bearing operating speed, oil viscosity, oil level, size and geometry of the oil sump and external oil agitation caused by surrounding mechanic elements.

The SKF model calculates the drag losses of rolling bearings following the equations (5.5.13) to (5.5.16).

Deep groove ball bearing

$$M_{drag} = 0.4 \cdot V_M \cdot K_{ball} \cdot d_m^5 \cdot n^2 + 1.093 \cdot 10^{-7} \cdot n^2 \cdot d_m^3 \cdot \left(\frac{n \cdot d_m^2 \cdot f_t}{\upsilon}\right)^{-1.379} \cdot R_s \tag{5.5.13}$$

$$K_{ball} = \frac{i_{rw} \cdot K_z \cdot (d + D)}{D - d} \cdot 10^{-12} \tag{5.5.14}$$

Roller bearing

$$M_{drag} = 4 \cdot V_M \cdot K_{roll} \cdot C_W \cdot B \cdot d_m^4 \cdot n^2 + 1.093 \cdot 10^{-7} \cdot n^2 \cdot d_m^3 \cdot \left(\frac{n \cdot d_m^2 \cdot f_t}{\upsilon} \right)^{-1.379} \cdot R_s \quad (5.5.15)$$

$$K_{roll} = \frac{K_L \cdot K_z \cdot (d + D)}{D - d} \cdot 10^{-12} \quad (5.5.16)$$

The remaining variables, common for ball and roller bearings are stated in equation (5.5.17) to (5.5.22).

$$C_W = 2.789 \cdot 10^{-10} \cdot l_D^3 - 2.786 \cdot 10^{-4} \cdot l_D^2 + 0.0195 \cdot l_D + 0.6439 \quad (5.5.17)$$

$$l_D = 5 \cdot \frac{K_L \cdot B}{d_m} \quad (5.5.18)$$

$$f_t = \begin{cases} \sin(0.5 \cdot t) & \text{when } 0 \leq t \leq \pi \\ 1 & \text{when } \pi < t < 2\pi \end{cases} \quad (5.5.19)$$

$$R_S = 0.36 \cdot d_m^2 \cdot (t - \sin(t)) \cdot f_A \quad (5.5.20)$$

$$t = 2 \cdot \cos^{-1}\left(\frac{0.6 \cdot d_m - H}{0.6 \cdot d_m} \right), \quad \text{when } H \geq d_m \text{ use } H = d_m \quad (5.5.21)$$

$$f_A = 0.05 \cdot \frac{K_z \cdot (D + d)}{D - d} \quad (5.5.22)$$

Where:

- M_{drag} is the frictional moment of drag losses [N·mm];
- V_M is the drag loss factor;
- B is the bearing width [mm];
- H is the oil level (figure 5.10);
- i_{rw} is the number of ball rows;
- K_L is a geometric constant related to the bearing type;

To determine the oil level, for tapered roller bearings the lowest point should be considered the outside diameter (D), and for all the other bearings should be the outer ring mean diameter ($0.5 \cdot (D + D_1)$).

The drag loss factor, V_M can be determined using figure 5.11.

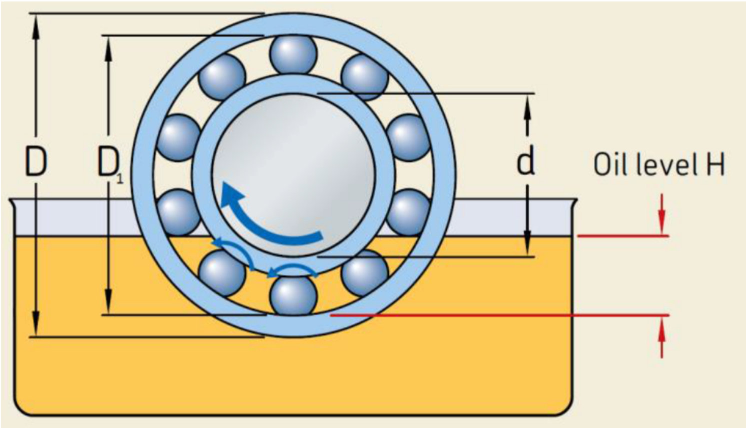

Figure 5.10.: Oil level measurement [36].

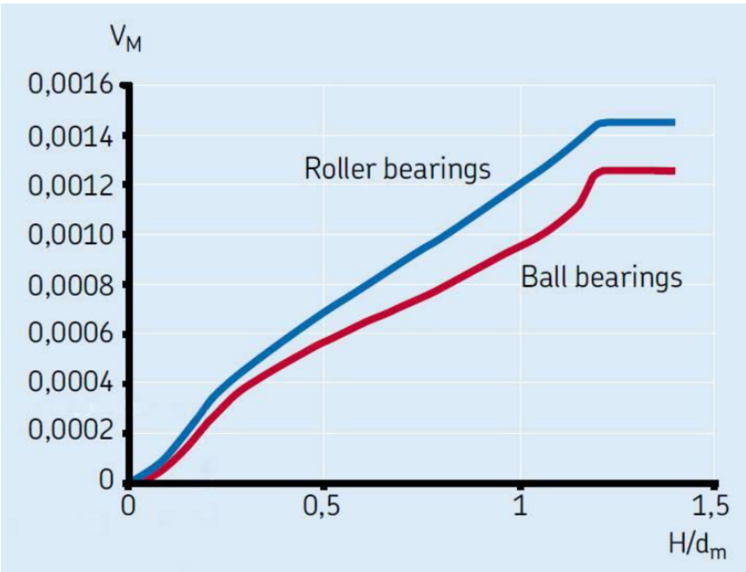

Figure 5.11.: Drag loss factor graph [36].

5.5.6. Preload (tapered roller bearings)

The tapered roller bearings are assumed to be in a back-to-back configuration and when an axial force acts in one of the bearings, the second bearing has to be subjected to a preload in order to diminish the axial displacement of the first bearing.

The preload force F_0 that prevents the second bearing (bearing B) of becoming unloaded in the presence of an axial force K_A in the first bearing (bearing A) is given by equation (5.5.23).

$$F_0 = K_a \cdot \left(\frac{c_B}{c_A + c_B} \right) \tag{5.5.23}$$

Where c_A and c_B are the spring constants of the bearings. As in the studied gearbox the bearings are equal, $c_A = c_B$ and equation (5.5.23) can be rewritten as:

$$F_0 = \frac{1}{2} \cdot K_a \tag{5.5.24}$$

The K_a value was determined based on the gearbox manufacturer's catalog for the maximum axial force allowed on the output shaft of the planetary gearbox and the axial force caused by the maximum input torque for each test.

An example of the power losses for the tapered roller bearing (TRB) and the deep groove ball bearing (DGB) is given in table 5.7, considering the nominal operating conditions of the tested gearbox, running with PAOR at 85°C.

Table 5.7.: Example for the bearings losses for the nominal operating conditions.

	Variables	Results	
		TRB	DGB
Rolling frictional moment [N·mm]	M_{rr}	2064.5	330.87
Variable of the rolling frictional moment	G_{rr}	14.756	1.0556
Inlet shear heating reduction factor	ϕ_{ish}	0.9932	0.9685
Kinematic replenishment/starvation reduction factor	ϕ_{rs}	1	1
Sliding friction moment [N·mm]	M_{sl}	2995.1	85.988
Variable of the sliding frictional moment	G_{sl}	43223	4299.4
Sliding frictional coefficient	μ_{sl}	0.1	0.1
Weighting factor for the sliding coefficient	ϕ_{bl}	0.6867	0
Frictional moment of drag losses [N·m]	M_{drag}	38.499	0*
Preload	F_0	33000	–
Total frictional moment [N·m]	M	5098.2	416.86
Total power loss [W]	P_{VL}	133.47	43.65

(*) – For grease lubricated rolling bearings the *SKF* model considers $M_{drag} = 0$ which is the case in study.

5.6. Needle roller bearing losses

The rolling bearing power loss model that was previously presented lacks the support for needle roller bearings. The frictional moment of a needle roller bearing, equation (5.6.1), was calculated according to both Höhn *et al.* [10] and Eschmann *et al.* [37] models.

$$T_{VL} = T_{VL0} + T_{VL1} \tag{5.6.1}$$

The no-load component is calculated according to equation (5.6.2).

$$T_{VL0} = \begin{cases} 1.6 \cdot 10^{-8} \cdot f_0 \cdot d_m^3 & \text{when } \upsilon \cdot n < 2000 \\ 10^{-10} \cdot f_0 \cdot (\upsilon \cdot n)^{\frac{2}{3}} \cdot d_m^3 & \text{when } \upsilon \cdot n \geq 2000 \end{cases} \tag{5.6.2}$$

Where:

- T_{VL0} is the no-load frictional moment [N·m];
- f_0 is a coefficient dependent on the bearing design and lubrication method ($f_0 = 12$);

The load component, T_{VLP1}, can be calculated using equation (5.6.3).

$$T_{VLP1} = 10^{-3} \cdot f_1 \cdot P_1 \cdot d_m \tag{5.6.3}$$

Where:

- P_1 is the equivalent bearing load;
- f_1 is a coefficient which takes into account the direction of load application ($f_1 = 0.002$)

An example of the power losses for the needle roller bearing is given in table 5.8, considering the nominal operating conditions of the tested gearbox, running with PAOR at 85°C.

Table 5.8.: Example for the needle roller bearing losses.

	Variables	Results
No-load component [N·m]	T_{VL0}	0.0303
Load component [N·m]	T_{VL1}	0.0588
Equivalent bearing load [N]	P_1	6687.3
Total frictional moment [N·m]	T_{VL}	0.0890
Total power loss [W]	P_{VL}	6.9937

5.7. Seals power loss

In most applications, seal power losses represent a minor fraction of the total power loss of a gearbox, and are almost negligible when compared to the losses of other components. Nevertheless, in order to obtain a model as realistic as possible, the seals losses were also taken into account. An approximation is given in equation (5.7.1) [10].

$$P_{VD} = 7.69 \times 10^{-6} \times d_{sh}^2 \times n \tag{5.7.1}$$

Where:

- d_{sh} is the shaft diameter [mm];
- n is the shaft rotational speed [rpm].

The seals power loss is independent of the transmitted torque, being the major influences the operating speed and the shaft diameter. It is possible that equation (5.7.1) needs small adjustments as different seal materials may influence the seals power loss [10].

Table 5.9.: Seals power losses for gearbox nominal working conditions.

	Variables	Results
Input Seal Power Loss [W]	$P_{VD_{in}}$	37.681
Output Seal Power Loss [W]	$P_{VD_{out}}$	55.560

For the nominal operating conditions of the test gearbox, table 5.9 shows the seal power losses in both input and output seals.

5.8. Heat balance

While a gearbox is operating heat is generated, which will be dissipated to the surrounding environment. According to thermodynamics, the mechanical energy that is dissipated by the gearbox must be equal to the thermal energy that the surrounding environment receives, equation (5.8.1).

$$P_V = \dot{Q}_{total} \tag{5.8.1}$$

The main heat transfer mechanisms are conduction, convection and radiation, equation (5.8.2).

$$\dot{Q}_{total} = \dot{Q}_{cd} + \dot{Q}_{cv} + \dot{Q}_{rad} \tag{5.8.2}$$

Thermal conduction reflect the small amount of heat that is transferred to the shafts, couplings and foundations of the gearbox. Convection and radiation comprise the heat transfer that occurs through the external surface of the gearbox.

Höhn *et al.* [10] suggested that the total heat flow rate can be calculated according to the equation (5.8.3).

$$\dot{Q}_{total} = \alpha_{Heat} \cdot A \cdot (T_{Oil} - T_{Room}) \tag{5.8.3}$$

Where:

- α_{Heat} is the heat transfer coefficient (which takes into account the heat transfer due to conduction, convection and radiation);
- A is the external area of the gearbox;
- T_{Oil} is the oil temperature;
- T_{Room} is the room temperature.

To be noticed, is the fact that equation (5.8.3) does not take into account other relevant characteristics of the air in the room, such as relative humidity. Bearing in mind that the specific heat of dry air and water vapor are, at atmospheric pressure:

- $c_{p_{dry\ air}} = 1.01 kJ/kg°C$
- $c_{p_{water\ vapour}} = 1.84 kJ/kg°C$

it is not difficult to understand that the relative humidity might be a relevant factor in the relation between the stabilization temperature ($T_{Oil} - T_{Room}$) and the total heat flow rate, therefore equation 5.8.3 can only be applied in very controlled environments.

Part III.

Experimental and Numerical Results

6. Sixteen Test Grid (PAOR)

6.1. Overall analysis

The sixteen test grid was planned with the aim of reaching a comprehensive understanding of the influence of the operating conditions in terms of power loss, efficiency, operating and stabilized temperatures as well as specific film thickness. As a secondary goal, the sixteen test grid was meant to evaluate the accuracy of the numerical model and its variation according to the operating conditions. The sixteen tests were performed with PAOR.

The power loss values of the sixteen test grid are shown in figure 6.1.

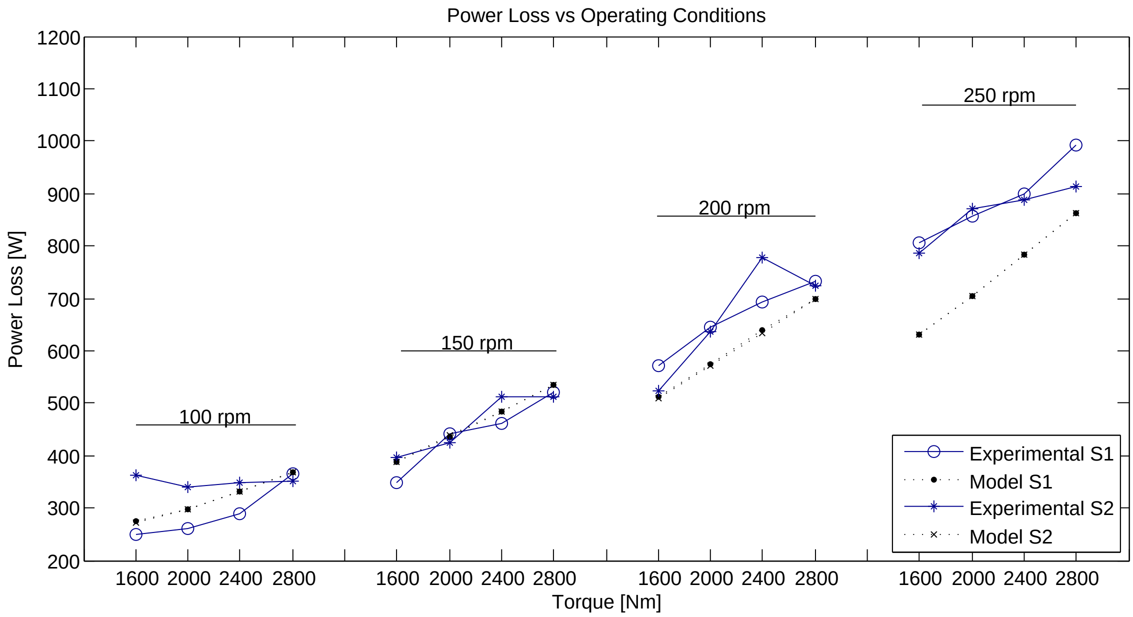

Figure 6.1.: PAOR: Power Loss.

It is visible a strong relation between operating speed and power loss. As speed increases, the power loss for each set of tests increases, even if the nominal input power is lower. An example is presented in table 6.1, considering the gearbox working as a multiplier (S1).

In roughly half of the tests, it is also visible that the power loss was not equal for both operating directions. This differences occur in three tests (out of four) at 100rpm, in two tests at 150 and 200rpm and at one test at 250rpm, meaning that this differences might be related to the operating speed.

Table 6.1.: Example of input power vs. power loss.

Speed* [rpm]	Torque* [Nm]	Input power* [W]	Power Loss [W]
150	2800	43982.3	624.5
200	1600	33510.3	671.9

(*) – Nominal Values

The numerical results are in reasonable agreement with the experiments at lower speeds (100 and 150rpm), standing in the middle of the experimental values of both directions. For higher speeds the numerical results stand bellow the experimental values, essentially because the numerical model is not considering the churning losses, which are highly dependent on the operating speed. The average deviation of the numerical results at higher speeds is 57W for 200rpm and 130W for 250rpm.

Numerical predictions are equal for both directions. This is due to the fact that the numerical model was not designed to consider the power flow through the components in the gearbox, assuming that the power arriving at each component is not affected by the power loss.

As it can be seen in figure 6.2, in terms of efficiency, the differences between both operating directions are even more notorious. Only four tests presented similar efficiency values for both directions. At 100rpm , the efficiency of the gearbox working as a multiplier was higher than when working as a reducer in three out of four tests. For the remaining twelve tests, this happened only once (150rpm/1600Nm).

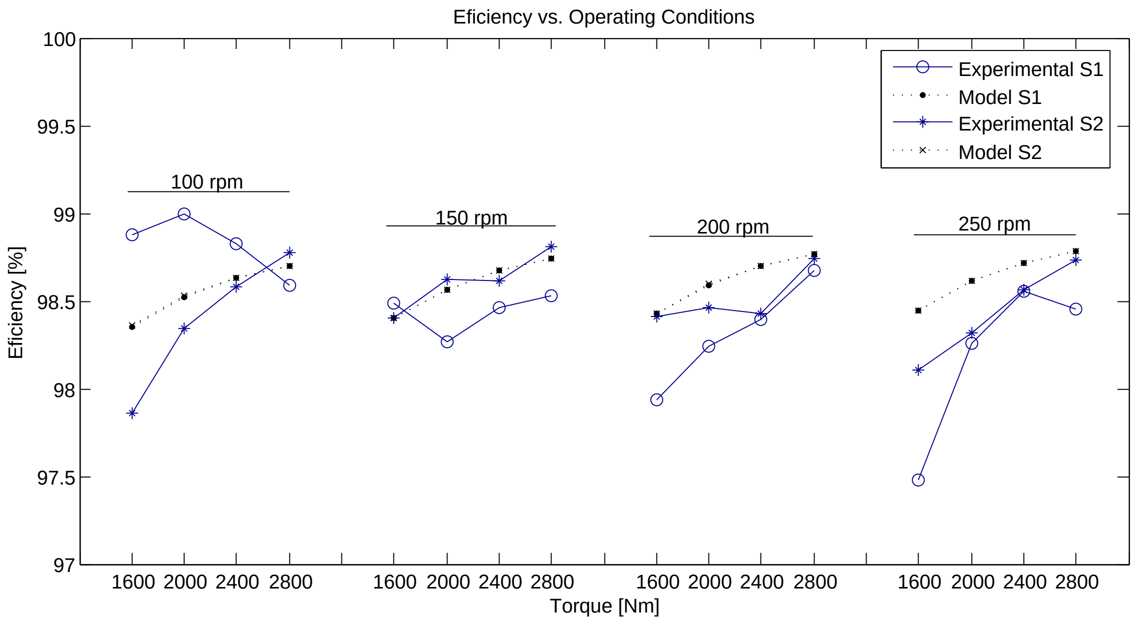

Figure 6.2.: PAOR: Efficiency.

Plotting the efficiency variation between both directions as a function of the nominal input power, the plot of figure 6.3 is obtained.

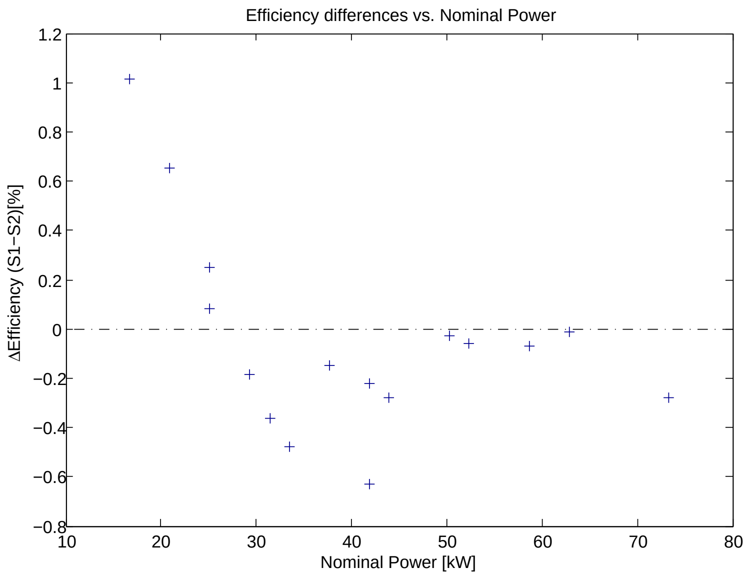

Figure 6.3.: Efficiency differences between both operating directions.

For a nominal power bellow 27kW, the gearbox presented higher efficiency working as a multiplier, while above 27kW presented higher efficiency as a reducer. Also, in the range of 45 to 65 kW the efficiencies of both directions presented variations bellow 0.1%.

It is important to notice that this differences found in the power loss and in the efficiency are not followed by significant differences in the stabilization temperature, figure 6.4. The stabilization temperature is defined as the difference between the oil and room temperatures ($\Delta T = T_{Oil} - T_{Room}$). Furthermore, the oil operating temperature is always higher in the second operating direction. This might be due to the fact that the test in direction S2 was always performed right after S1, with a few minutes of interval.

The differences found in the measured values of power loss and efficiency might be somehow affected by the measurement uncertainty of the torque sensors, as there are no unusual behaviors in the operating and stabilized temperatures that could justify the differences found.

Having the knowledge of the power loss and the temperatures of stabilized operating conditions it is possible to define a global heat transfer coefficient according to equation (5.8.3). The surface area of the gearbox couldn't be ascertain accurately, so instead of determine a heat transfer coefficient - α - , it was determined the product of the heat transfer coefficient by the gearbox surface area, αA. Since the numerical results are in fair agreement with the experimentals, αA was calculated considering both numerial and experimental power loss. These results are shown in figure 6.5.

The experimental values presented a much higher dispersion (the norm of residuals is nearly three times the value found for numerical values). This might indicate that there is indeed a measurement uncertainty associated with the torque sensors or that due to the different weather conditions, the properties of the air of the room

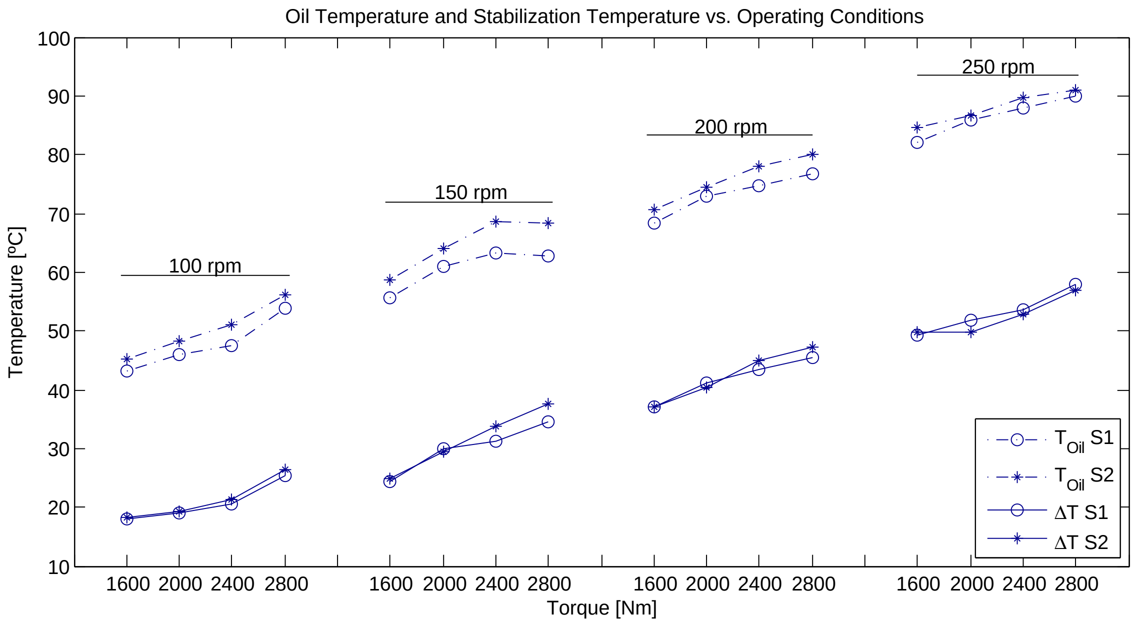

Figure 6.4.: PAOR: Oil temperature and Stabilization temperature.

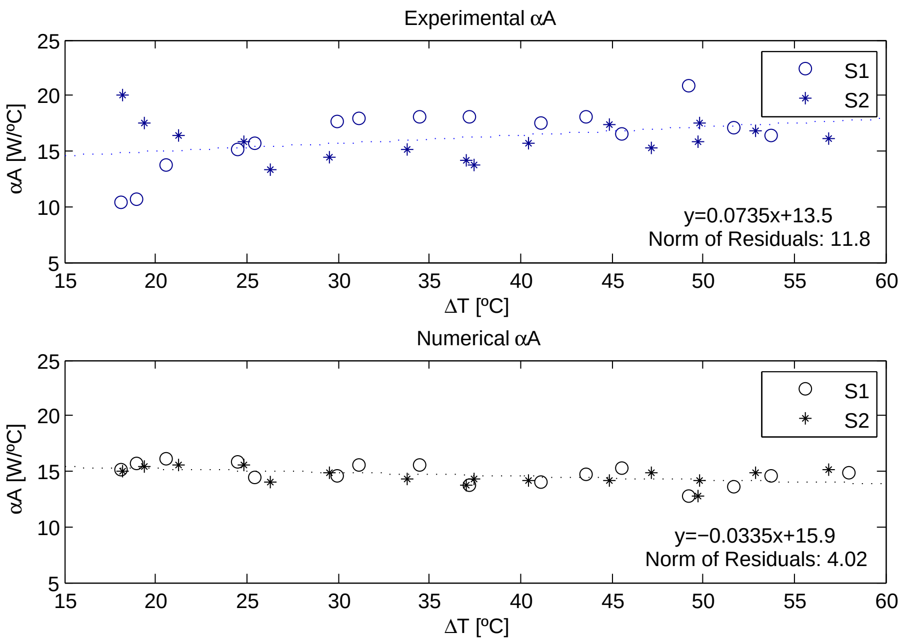

Figure 6.5.: PAOR: Heat transfer coefficient.

differed considerably between tests and therefore the stabilized room temperature is not enough to ascertain the heat dissipated by the gearbox. As referred in section 5.8, the relative humidity of the air in the room is a relevant factor in the estimation of the dissipated heat.

The numerical values, although presenting a lower dispersion, follow a slightly decreasing trend line, which is not consistent with previous works [3]. Nevertheless, this can be explained by the fact that the model is not considering the churning losses. The highest temperatures occur at higher speeds, where the churning losses are more relevant. If the churning losses were considered, the amount of power loss found with higher operating temperatures would have led to an increasing trend line in the numerical values.

In order to understand in which range of lubrication regime the tests were performed the specific film thickness was calculated. The results are presented in figure 6.6.

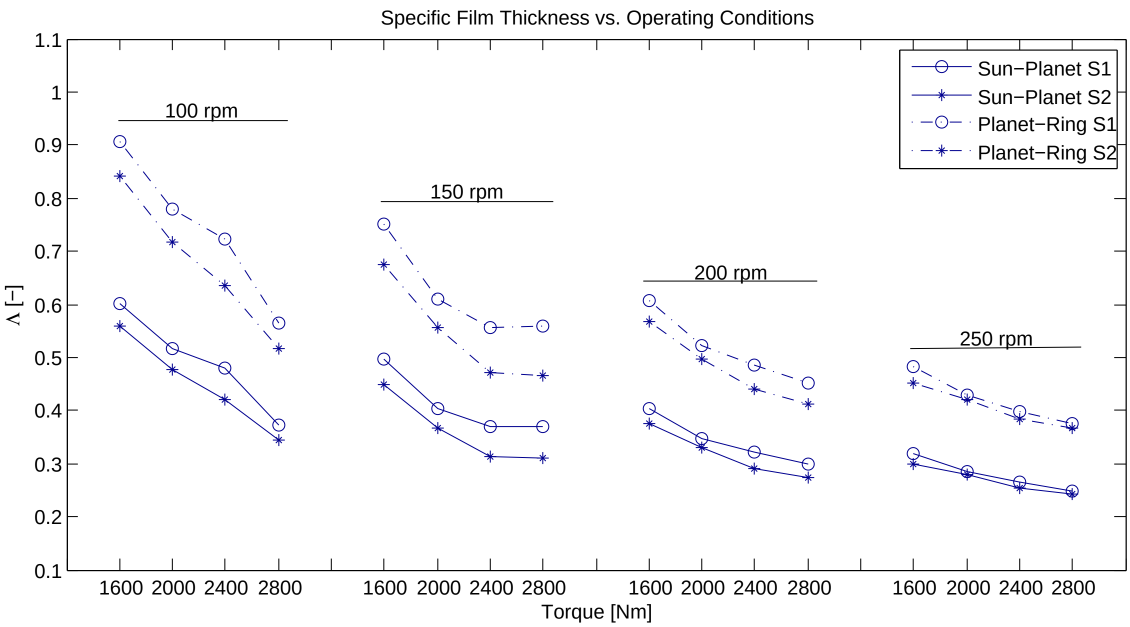

Figure 6.6.: PAOR: Specific Film Thickness.

The specific film thickness follows a decreasing trend with increasing torque and/or speed. For lower speeds, the specific film thickness is very sensitive to an increase of torque while at higher speeds the decrease of the specific film thickness with increasing torque is not so marked. The film thickness depends on the oil operating dynamic viscosity, which in turn depends on the operating temperature. Comparing both temperature and film thickness results, it is clear that the film thickness lowers with increasing oil temperature, as a consequence of lower dynamic viscosity.

The Planet-Ring contact has always higher specific film thickness than the Sun-Planet contact, mainly due to the higher equivalent radius and its lower load line. The Sun-Planet contact presented specific film values lower than 0.7, meaning it is operating in a boundary film lubrication regime. As for the Planet-Ring contact, the lubrication regime is also boundary film, except for the tests 100rpm/1600Nm and 100rpm/2000Nm.

It was also found that the specific film thickness of direction S1 was always higher than the ones for direction S2. This occurs because the specific film thickness has a direct correlation with the operating viscosity which in turn depend on the oil temperatures which were always higher for direction S2, explaining the lower specific film thickness values.

6.2. Numerical predictions:part by part

In figure 6.7, the numerical power loss results were plotted discerning the contribution of each component of the gearbox in the total power loss.

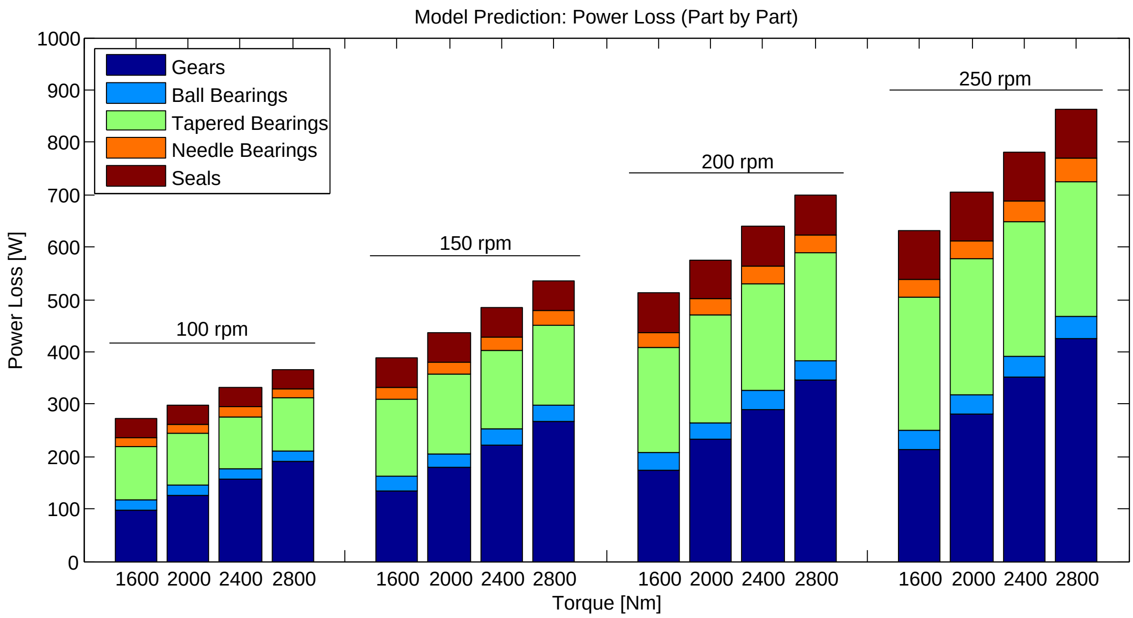

Figure 6.7.: Power Loss: Part by Part.

The two main sources of power loss were the gears and the tapered rolling bearings. The tapered rolling bearings losses only overcame the gear losses in the tests with the lowest torque (1600Nm). For all the other torques, the gears were the main source of power loss.

The gear losses seem to be equally dependent on the speed and torque. The tapered rolling bearing losses were roughly constant with increasing torque, but showed to be quite sensitive to the operating speed. The studied gearbox is a planetary speed multiplier capable of supporting very high radial and axial loads in the output shaft, meaning that the tapered roller bearings have a fairly high preload. Since the helical angle of the planetary gear is quite low, the axial forces applied in the tapered will be considerably low when compared to the preload, therefore the power loss in the tapered roller bearings is almost independent of the input torque.

The third source of power loss were the seals. According to equation (5.7.1), the seals' losses are exclusively dependent on the operating speed.

The ball and the needle roller bearing losses had the least significant contribution to the total power loss. It is evident that both ball and needle roller bearings react to an increase of speed. For the lowest speed (100rpm), the mentioned bearings react poorly to the torque increases, but for the others speeds, it seems that the ball and needle bearing losses gain sensitivity to the torque increases too.

Considering the two extreme values of speed and torque, the power loss of each component was plotted as percentages relative to the input power, shown in figure 6.8.

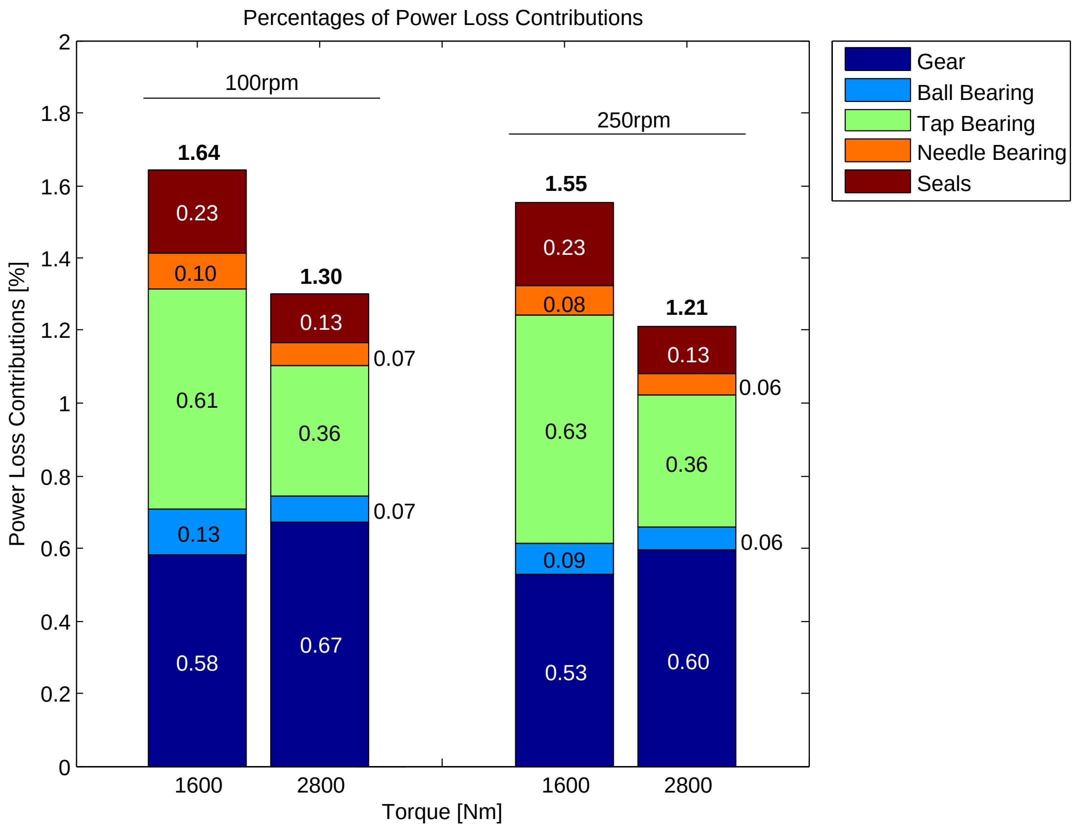

Figure 6.8.: Percentages of Power Loss Contributions.

The weight of each dissipation source in the total power loss does not vary much with the speed, but it's highly sensitive to torque variations.

The gears are responsible for a power loss between 0.53% and 0.67% of the input power. Their relevance increases with torque and decreases with speed.

The tapered roller bearings are responsible for a power loss of 0.61% and 0.63% at the lowest torque, but decrease to 0.36% at the highest load. Their importance is roughly constant with speed but greatly decreases as torque increases.

The importance of the seals is strictly dependent on the torque and decreases when the torque increases. The seals are responsible for losses from 0.13% to 0.23%

of the input power.

Both ball and needle roller bearings are minor power loss sources. They both decrease their relevance with increasing speed and/or increasing torque. The power losses associated to the ball and needle rolling bearings vary form 0.06% to 0.13% of the input power.

7. Five Test Grid

7.1. PAOR

After the sixteen test grid the test and slave gearboxes changed places. To assess the repeatability of the tests, the five grid test was repeated with fresh PAOR oil. The power loss results are shown in figure 7.1.

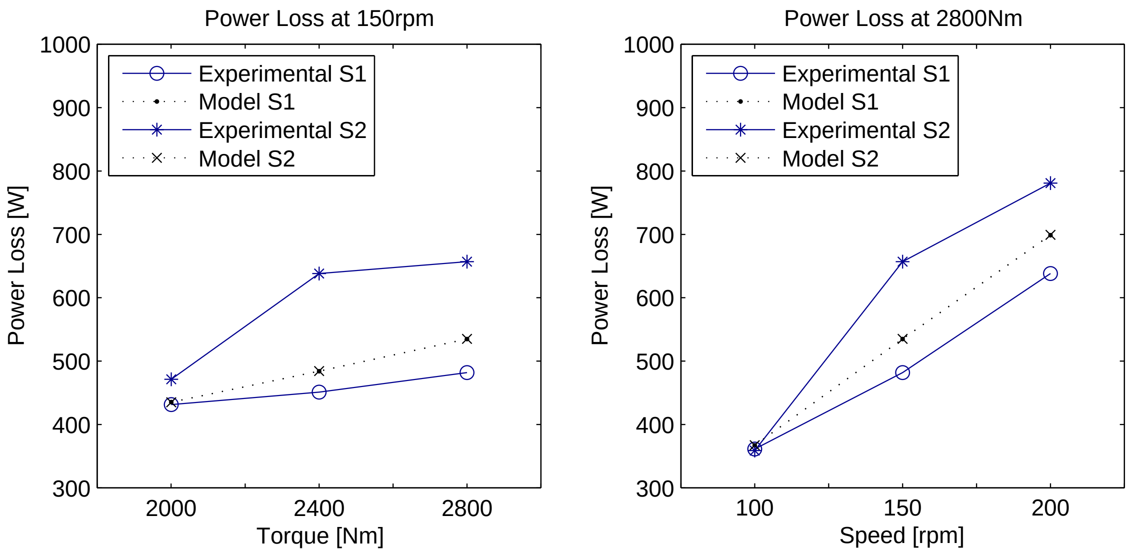

Figure 7.1.: PAOR: Power Loss.

For the five tests carried out, the power loss was always higher when the gearbox worked as reducer, except for the test at 100rpm and 2800Nm, which had very similar values in both operating directions. The numerical results for the power loss values stood in the middle of the experimental values, once again.

In terms of efficiency, the results are presented in figure 7.2.

Despite all the five tests being carried out above 27kW of nominal input power, the efficiency obtained for this tests does not match the results obtained for the sixteen grid test, were above 27kW the efficiency in S2 were always higher (see figure 6.3).

The two tests carried at a nominal input power lower than 35kW (100rpm/2800Nm and 150rpm/2000Nm) had a higher efficiency with the gearbox working as a reducer. For the rest of the tests, with a nominal input power above 35kW, the efficiency as multiplier overcame the efficiency as reducer.

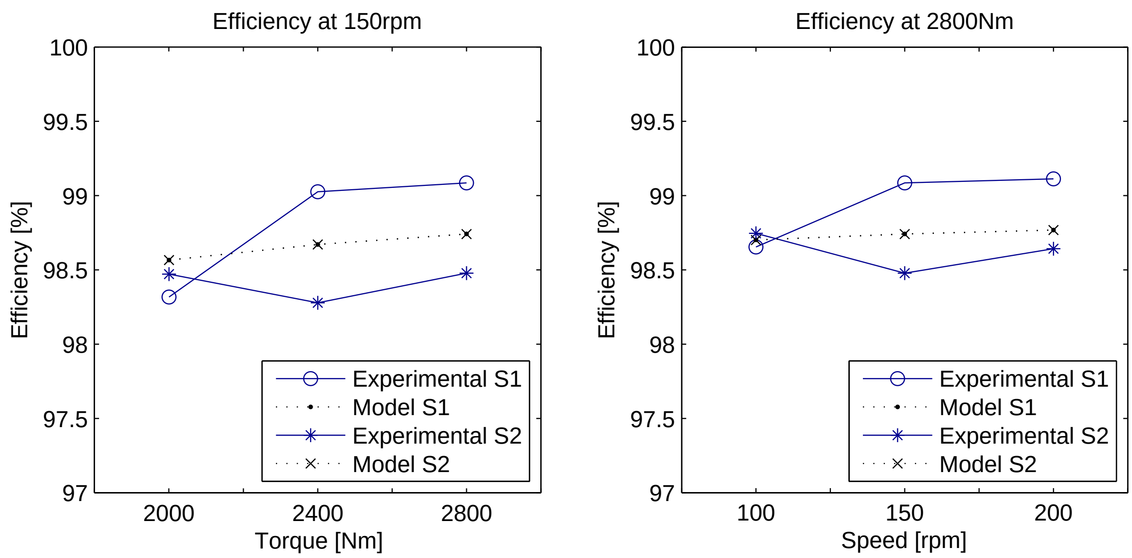

Figure 7.2.: PAOR: Efficiency.

In both PAOR grids, there is a correlation between the nominal input power and the direction with higher efficiency. Nevertheless, this correlation is not clear: in the first grid, the power level at which the higher efficiency changed from one direction to another was at 27kW, and in the second grid was at 35kW. Furthermore, in the first grid the highest efficiency evolves from S1 at lower input power to S2 at higher power and in the second grid, it happens the other way around: the highest efficiency belongs to S2 at lower input power, and evolves to S1 at higher power levels.

It is worth noting that not all the tests carried for the second time presented the same results. The results obtained for the 100rpm/2800Nm and 150rpm/2000Nm tests were very similar in power loss, efficiency and operating and stabilized temperatures. For the rest of the tests, the values presented relevant differences. A detailed comparison between the sixteen and five grid tests can be consulted in appendix (consult section B.3).

The operating and stabilized temperatures are presented in figure 7.3.

In this grid, the operating and stabilized temperatures associated to S2 were always higher. The higher stabilized temperature associated to S2 indicates higher power loss when the gearbox works as a reducer, even that the measured power loss values (see figure 7.1) do not always follow the temperature readings.

Comparing with the sixteen test grid, the operating temperatures follow the same trend (S2 higher than S1), although some values do not match. This happens because the power loss is related to the stabilized temperature, which in turn depends of the room temperature. Nevertheless, while the stabilized temperature of the sixteen tests presented very similar values for both operating directions, in the five test grid these differences can't be disregarded.

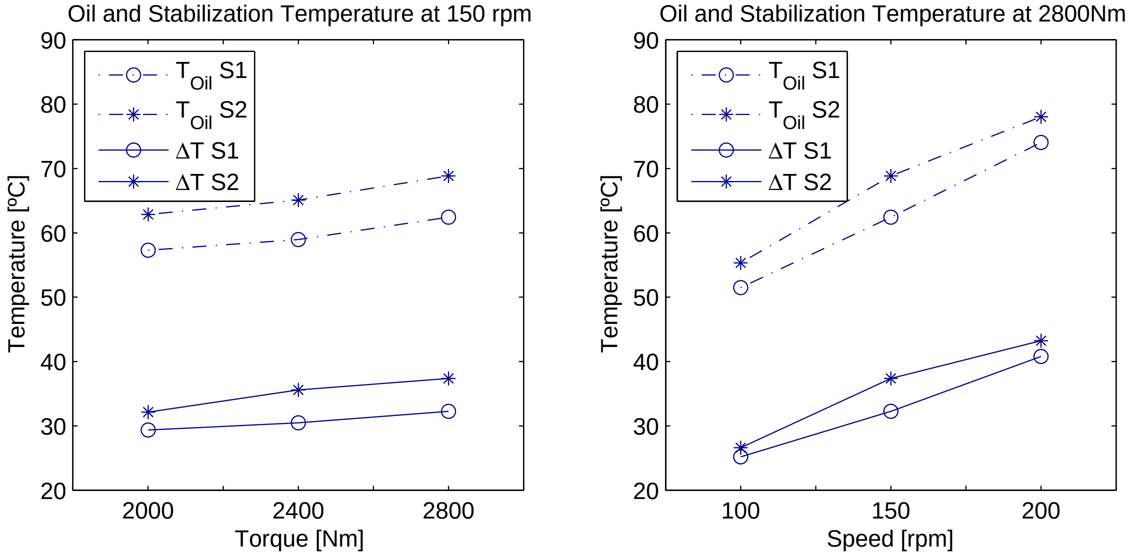

Figure 7.3.: PAOR: Oil and Stabilization temperatures.

7.2. MINR

After the PAOR, the MINR was tested. The power loss values obtained are presented in figure 7.4.

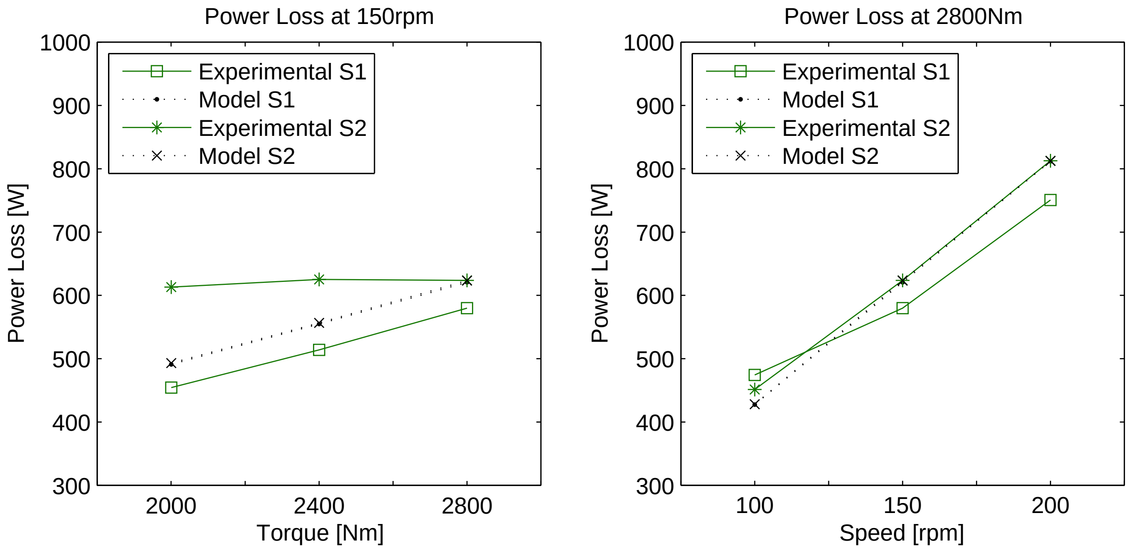

Figure 7.4.: MINR: Power Loss.

For the test at lowest nominal input power, the numerical predictions were lower than the experimental values in both operating directions, and the power loss in S1 was higher than in S2. For all the other tests, S1 presented lower losses than S2 and the numerical predictions stood between the experimental readings.

In what regards to the efficiency, the results obtained are shown in figure 7.5.

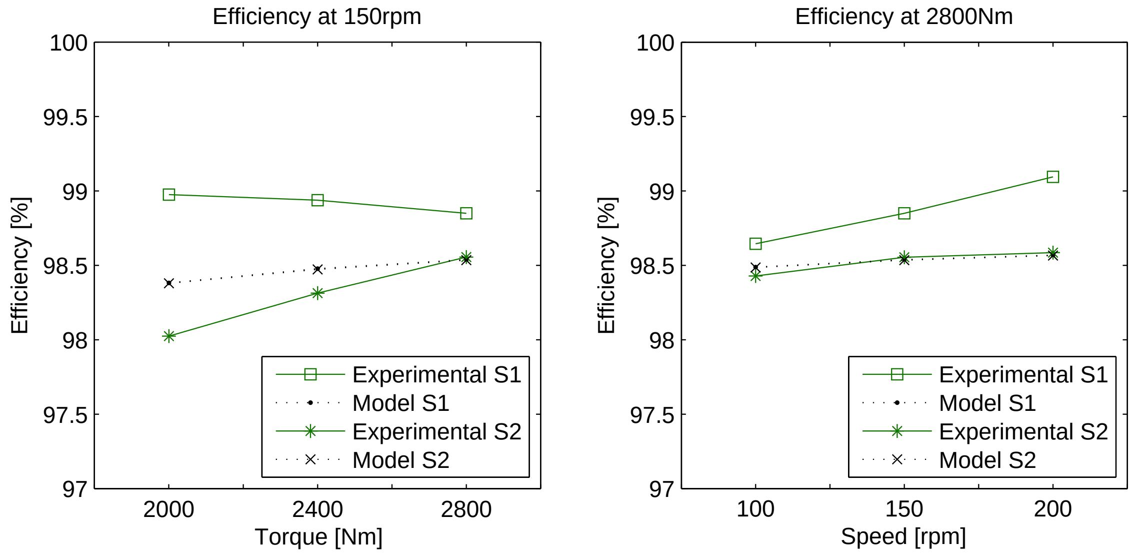

Figure 7.5.: MINR: Efficiency.

The efficiency was always higher when the gearbox worked as a multiplier, and the numerical results stood between the experimental reading or slightly bellow. For the 150rpm set of tests, the efficiency of direction S1 showed a decreasing trend with increasing torque, although this values are not supported by any abnormal behavior in the operating or stabilized temperatures, see figure 7.6.

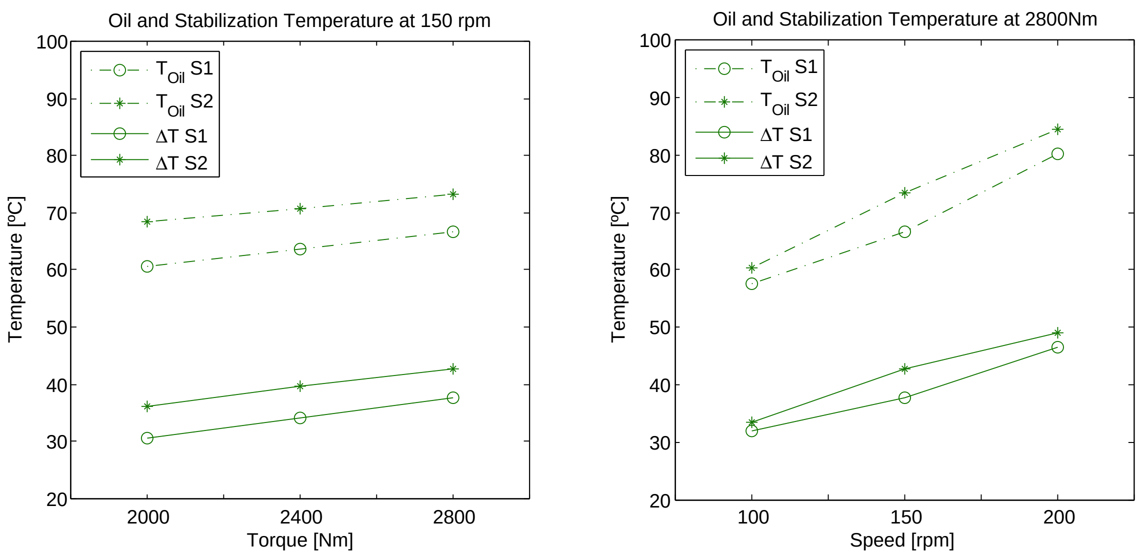

Figure 7.6.: MINR: Oil and Stabilization temperatures.

In similarity to what happened with the PAOR, the operating and stabilized temperatures associated to S2 were always higher than S1. Therefore, the temperature readings indicate different efficiencies for both directions, and independent of the nominal input power.

7.3. MINE

The third oil to be tested was the MINE. The power loss results are presented in figure 7.7.

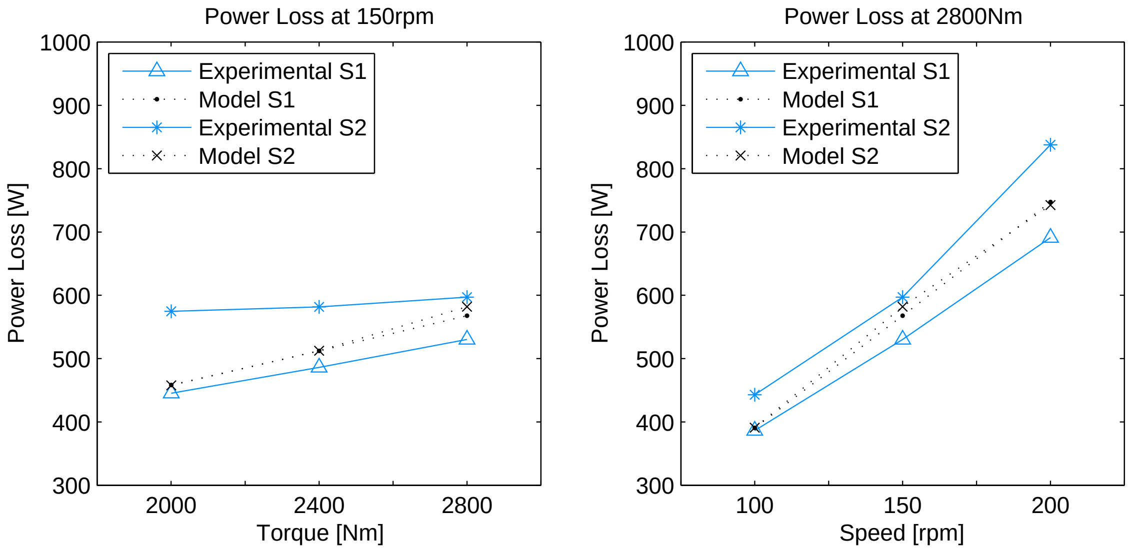

Figure 7.7.: MINE: Power Loss.

For the MINE power loss results, the direction S2 had always higher losses than S1 and the numerical results stood between the experimental values for both operating directions.

Figure 7.8 presents the efficiencies at stabilized operating conditions.

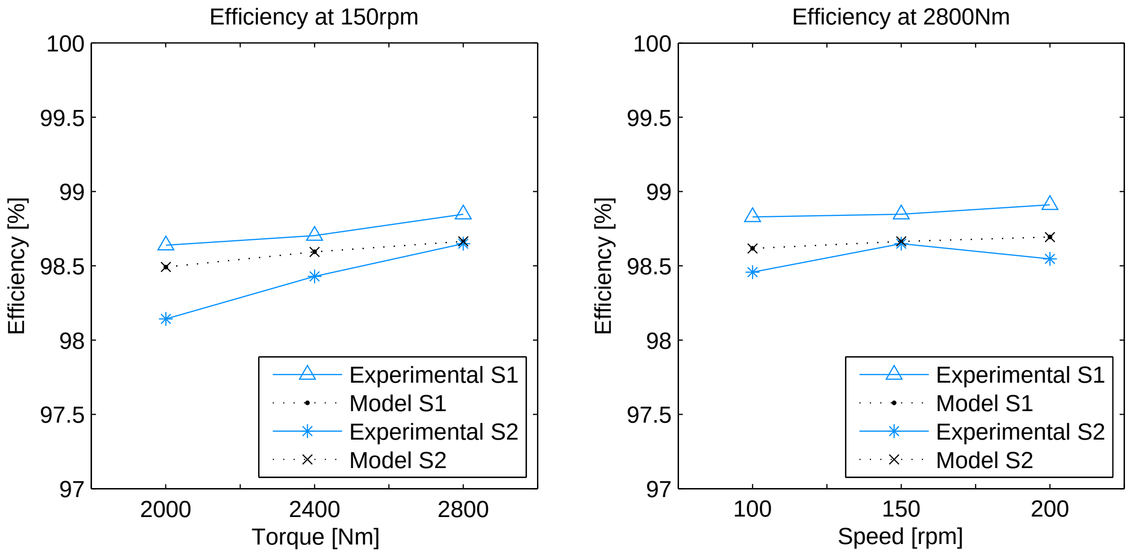

Figure 7.8.: MINE: Efficiency.

As well as the power loss results, the efficiency values were quite consistent. S1

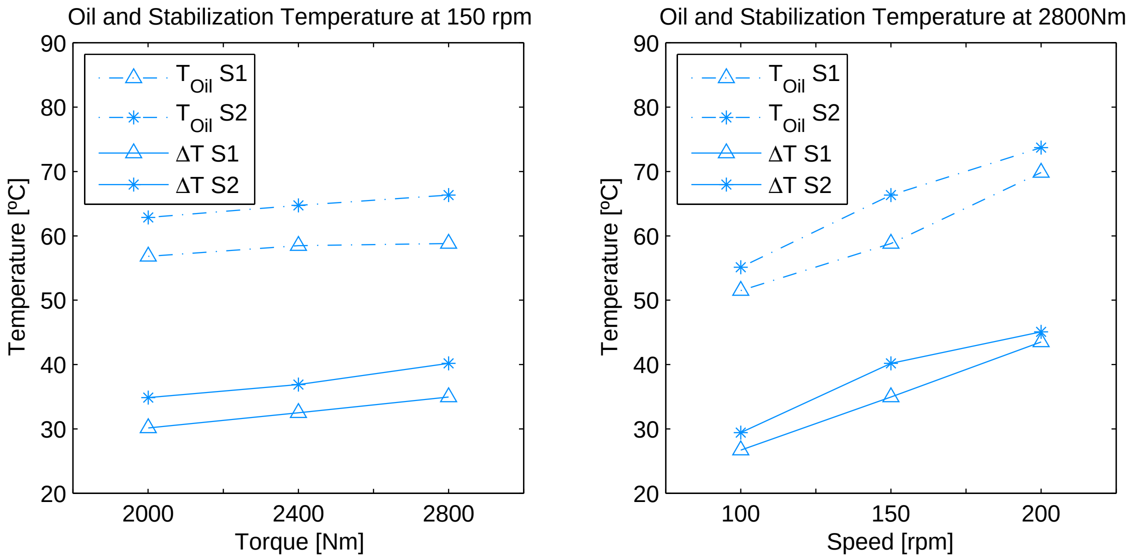

Figure 7.9.: MINE: Oil and Stabilization temperatures.

presents a higher efficiency than S2, and the numerical values stood in between the experimental ones.

As for the temperature readings, the values are presented in figure 7.9. The results obtained are consistent with both power loss and efficiency results. Furthermore, the temperature results of MINE follow the same trend as the previous oils: both operating and stabilized temperatures are higher for S2.

7.4. PAGD

The experimental campaign finished with the PAGD gear oil. The power loss results are show in figure 7.10.

For PAGD, the power losses associated to S2 were higher than for S1, except for the test 100rpm/2800Nm where the power loss values were roughly equal. Contrary to what was observed for the other oils, the numerical values stood bellow the experimental readings. This is due to the fact that the model is not considering the churning losses, and for PAGD this fact has more importance, as for the same volume of oil PAGD is heavier than all the others (see figure 2.3). More energy is needed to keep a heavier mass in acceleration, explaining the larger differences between the numerical and experimental results when compared to the predictions for the other oils. Also, PAGD has a higher dynamic viscosity when compared to the other oils which also contributes to increase the churning losses.

The efficiency results are presented in figure 7.11

The efficiency was always higher when the gearbox worked as a multiplier. The differences found between the two operating conditions seem to be constant at constant speed, while diverging at constant torque. The numerical values vary from

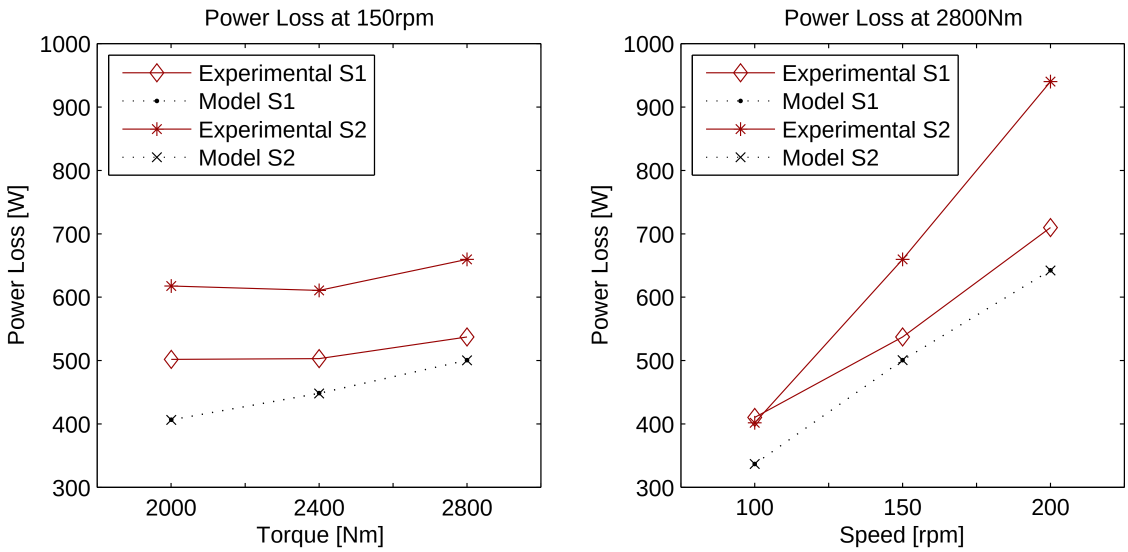

Figure 7.10.: PAGD: Power Loss.

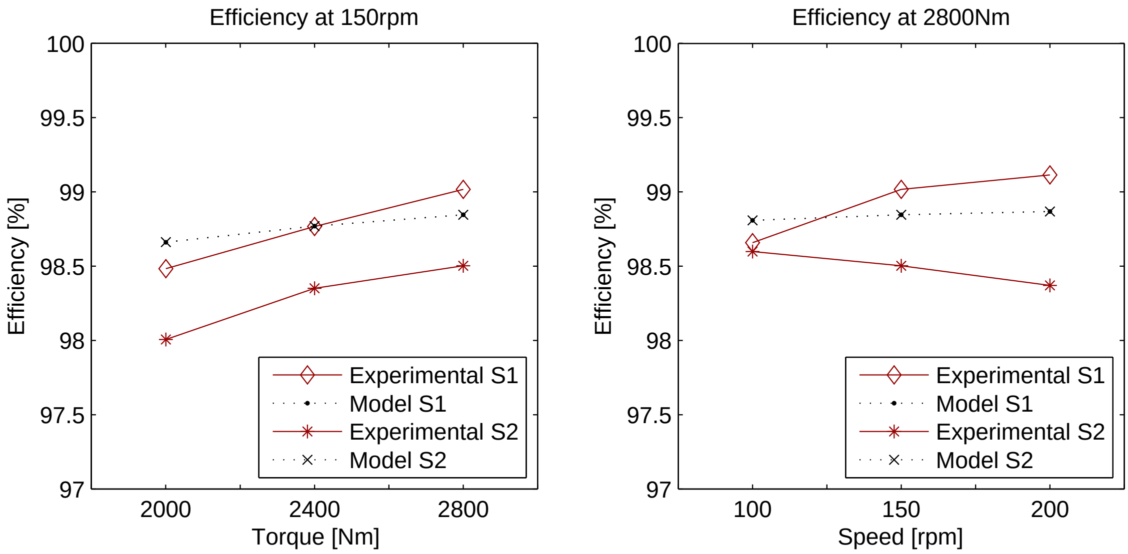

Figure 7.11.: PAGD: Efficiency.

standing between the efficiency of both operating directions or being higher than both, mainly because the predicted power loss was lower than the measurements.

A detail to notice is that the for the 100rpm/2800Nm test, the power loss and efficiency values were very close, and it is reflected in the lowest difference of stabilized temperatures for both operating directions.

Figure 7.12 presents the readings in what concerns to operating and stabilized temperatures.

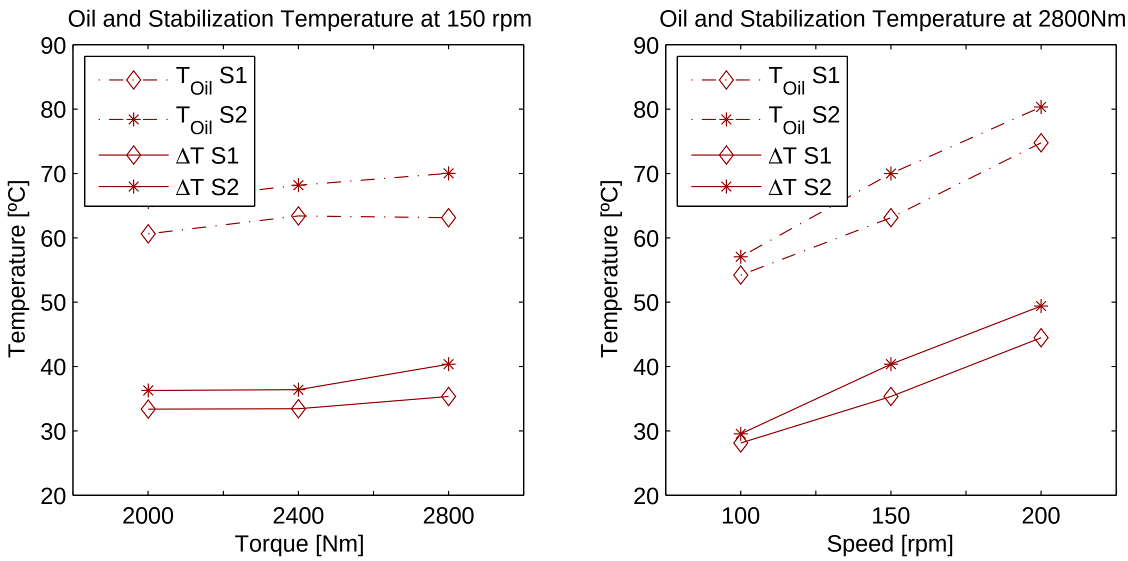

Figure 7.12.: PAGD: Oil and Stabilization temperatures.

PAGD temperatures analysis showed to be consistent with the rest of the tested oils, as the temperatures associated to S2 are higher than the ones associated to S1.

7.5. Oil Comparison

7.5.1. Experimental Results

In the following paragraphs, some parameters such as stabilization temperature, specific film thickness, kinematic and dynamic viscosity were analyzed simultaneously for the four tested oils in order to compare their performance. Parameters such as power loss and efficiency were not plotted as they show irregular results, probably associated to the measurement uncertainty of the torque sensors. All the plotted parameters are related to the operating direction S1 (multiplier).

The stabilized operating temperature for the tested oils is show in figure 7.13.

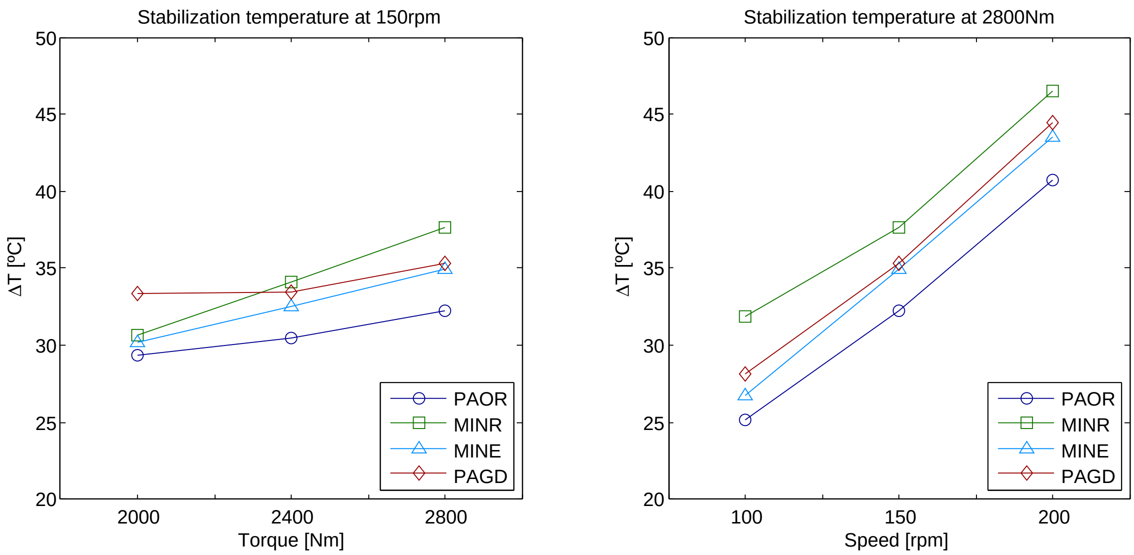

Figure 7.13.: Oil comparison: Stabilization Temperature.

For all the operating conditions, PAOR showed the lowest stabilization temperatures, which indicates that PAOR is the oil that promotes the most efficient operation.

For the lowest nominal torque (2000Nm), PAGD showed the highest stabilization temperature. For all the other tests, the highest stabilization temperature was reached by MINR. To be noticed is the fact that for constant speed, the MINR showed a significant increase of the stabilization temperature with increasing torque, while PAGD started with the highest value, but kept the stabilization temperature almost constant. When the specific film thickness is analyzed (see figure 7.17) it can be seen that at constant speed and with increasing torque, PAGD does not suffer a decrease as marked as the other oils, therefore leading to lower losses in the gears.

At constant torque, all the oils showed a significant increase of the stabilization temperature with increasing speed.

The oil operating temperature is represented in figure 7.14.

Although PAOR showed the lowest stabilization temperature, the lowest operating temperature is shown by MINE in all working conditions, except for the test at

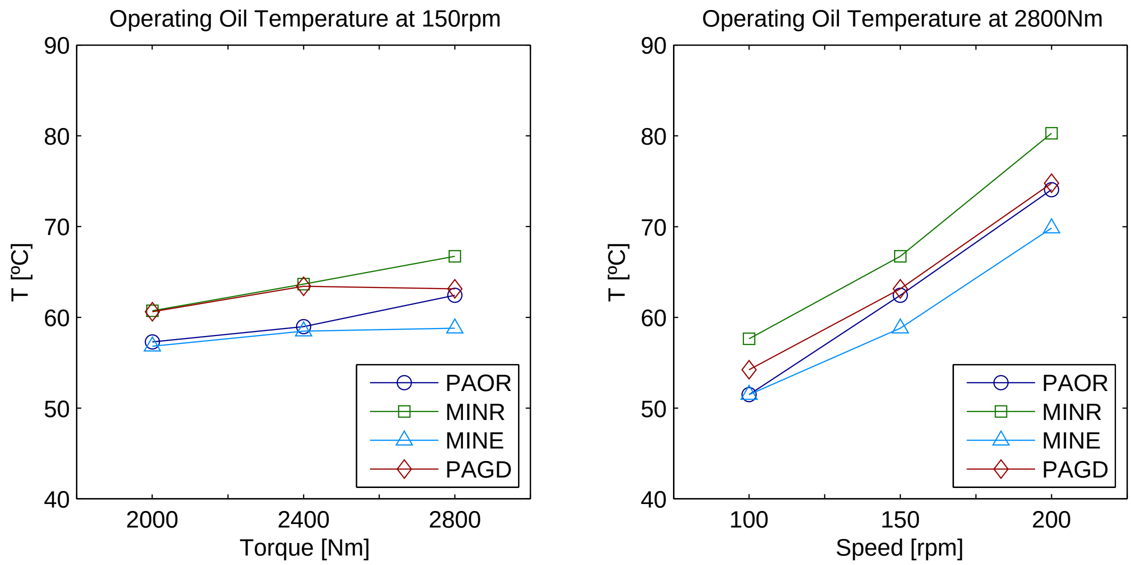

Figure 7.14.: Oil comparison: Operating Temperature.

2000Nm, where the operating temperature of both oils was fairly equal. The operating temperature difference between this two oils seems to increase with increasing power: the differences became evident for the two tests with highest power: 150rpm/2800Nm and 200rpm/2800Nm.

MINR showed the highest operating temperature for the tests carried at 2800Nm. For the other two tests, the operating temperature of MINR and PAGD were similar.

High operating temperatures are to be avoided. Despite the being related to higher power losses, high temperatures have several undesired side effects: they contribute to an increase of the surface failure probability as they lead to thinner film thickness and possible higher friction coefficient [38].

The kinematic and dynamic viscosity are shown in figures 7.15 and figure 7.16, respectively.

In what concerns to the kinematic viscosity the four oils can be ordered from the highest value to the lowest: MINE showed the highest kinematic viscosity, followed closely by PAOR. PAGD stands in the third place, but close to MINE and PAOR. MINR presented the lowest value and significantly far from the other three oils (lowest viscosity index).

As for the dynamic viscosity, PAGD showed the highest values, mainly due to its density which is considerably higher than all the other oils. The rest of the oils follows the same order as for kinematic viscosity: MINE had higher values than PAOR and MINR showed the lowest values of dynamic viscosity, and considerably away from the other oils.

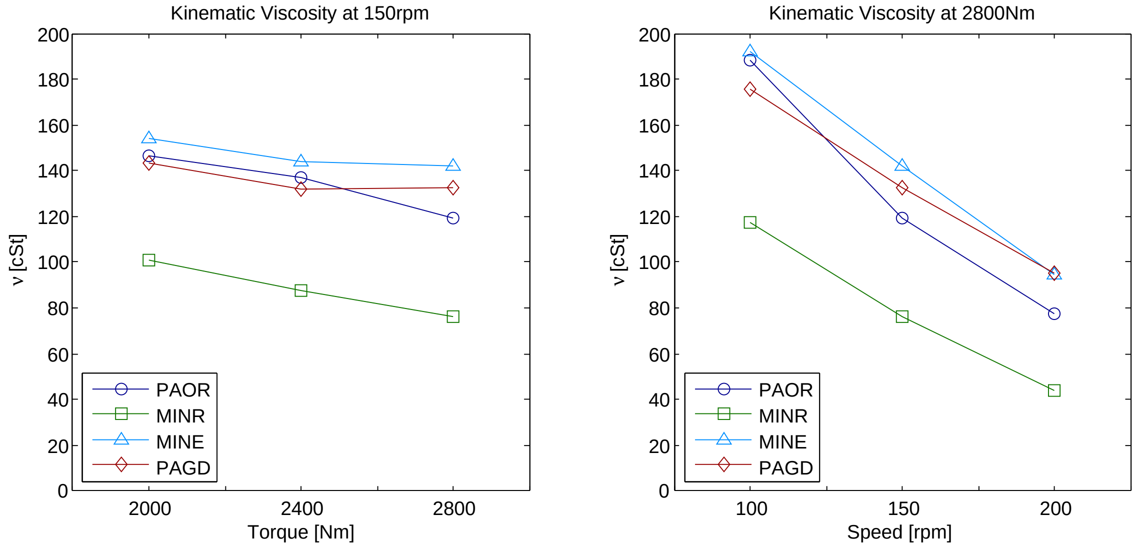

Figure 7.15.: Oil comparison: Kinematic Viscosity.

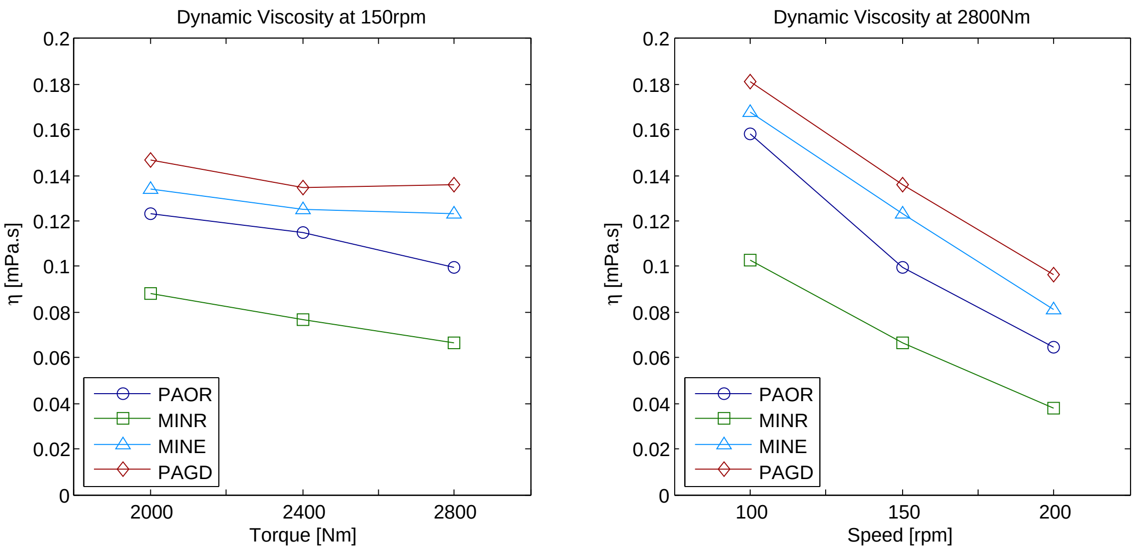

Figure 7.16.: Oil comparison: Dynamic Viscosity.

The specific film thickness depends on a multitude of factors. In what regards the oil properties, the specific film thickness depends on the dynamic viscosity and both thermoviscosity and piezoviscosity coefficients. Therefore, the specific film thickness depends of the operating temperature.

The specific film thickness for the Sun-Planet contact and for the Planet-Ring contact is presented in figure 7.17.

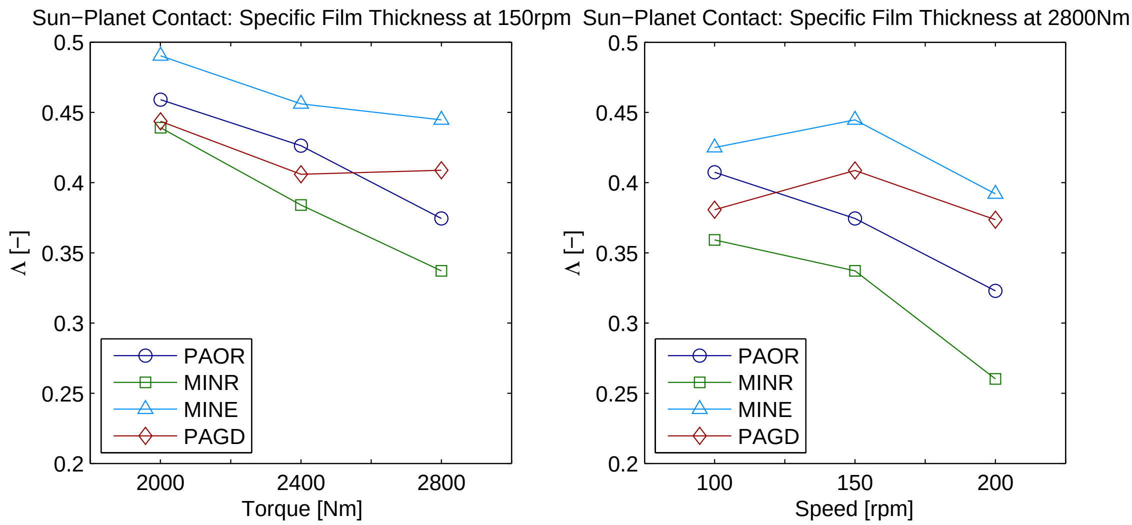

(a) Sun-Planet Contact.

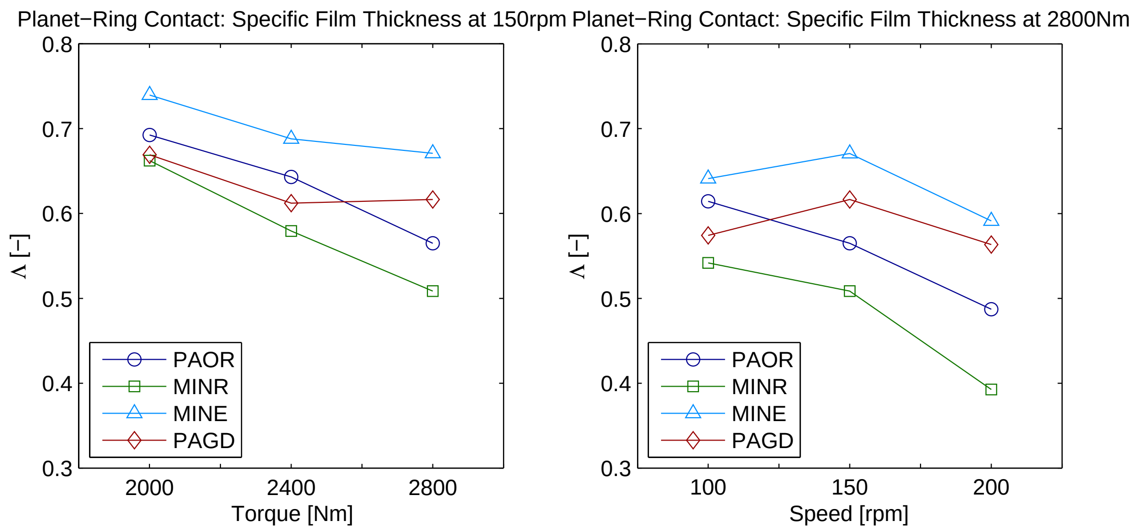

(b) Planet-Ring Contact.

Figure 7.17.: Oil comparison: Specific Film Thickness.

Although with different values, all the oils show the similar trends regarding both contacts. The specific film thickness stood bellow 0.7 for all oils, indicating a boundary film lubrication regime in both contacts. The only exception was the test 150rpm/2000Nm performed with MINE, were the Planet-Ring contact has a specific film thickness higher than 0.7.

MINE showed the highest specific film thickness for the ranged working conditions, while MINR showed the lowest. According to the American Gear Manufacturers Association [38] the specific film thickness has a direct relation to the gear failure probability. Such low specific film thickness as the ones found in MINR lead to a higher breakdown probability than the other oils for the performed tests.

PAGD overcame the specific film thickness of PAOR in the two tests with the highest power level: 150rpm/2800Nm and 200rpm/2800Nm. PAOR showed a decreasing trend with increasing power or with increasing torque while PAGD at constant speed showed a tendency to stabilize with increasing torque and at constant torque showed its best results at 150rpm.

Ferrography results

The ferrography results for PAOR are present in figure 7.18. The sample analyzed was taken in the end of the sixteen test grid.

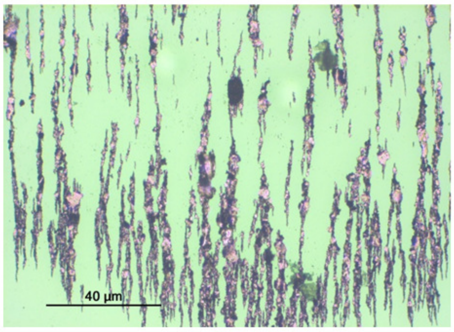

(a) Dilution: 0.1; Location: Core.

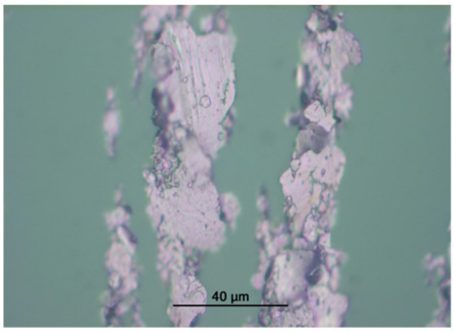

(b) Dilution: 0.1; Location: Core.

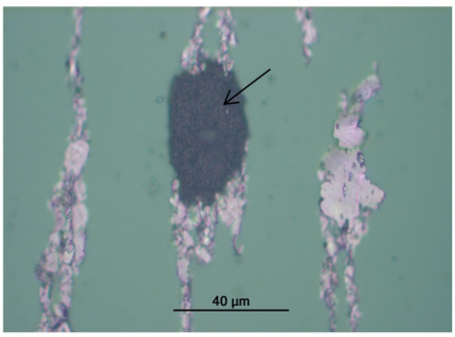

(c) Dilution: 0.1; Location: Core.

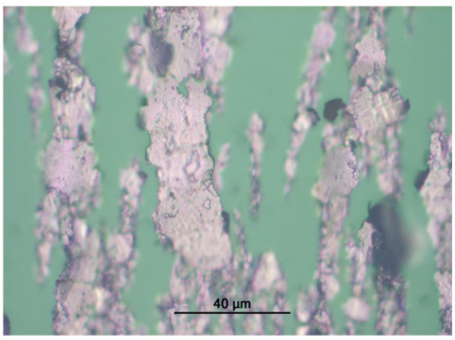

(d) Dilution: 0.1; Location: Core.

Figure 7.18.: Ferrography images: PAOR.

In photograph 7.18a is visible the presence of ferrous particles, some of big dimension.

Photographs 7.18b, 7.18c and 7.18d are magnifications of photgraph 7.18a. Photograph 7.18b and 7.18d show ferrous particles resultant of fatigue wear. In photograph 7.18c is visible a high density friction polymer.

The ferrography results for the MINE oil showed a significant presence of both small and big ferrous particles, see photograph 7.19a. In photograph 7.19b and 7.19c is visible ferrous particles of big dimensions, typical of severe fatigue wear.

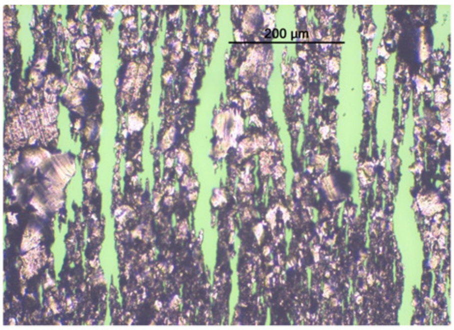

(a) Dilution: 1; Location: Core.

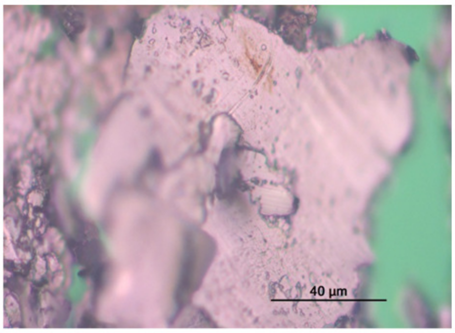

(b) Dilution: 1; Location: Core.

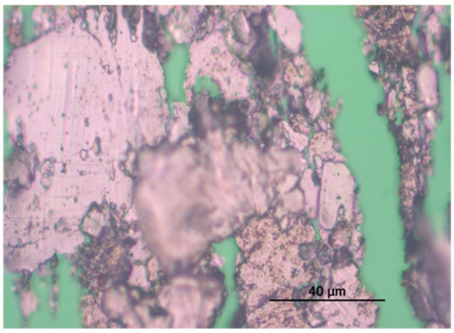

(c) Dilution: 1; Location: Core.

Figure 7.19.: Ferrography images: MINE.

The MINR results are presented in figure 7.20. In photograph 7.20a is visible some wear ferrous particles and thermal oxides.

Photographs 7.20b, 7.20d and 7.20c are magnifications of the first photograph. In 7.20b is visible a ferrous particle of big dimensions slightly oxidized; figures 7.20c and 7.20d show ferrous particles of both big and small dimensions as well as particles from varnishes.

As for the PAGD, the ferrography results are shown in figure 7.21. Photograph 7.21a shows several particles of big dimensions.

Figure 7.21b revels a ferrous particles of large dimensions, typical of adhesive wear.

Figures 7.21c and 7.21d show ferrous particles of large and medium sizes typical of fatigue wear and thermal oxides.

As for the direct reading ferrography results, the values are presented in table 7.1.

The CPUC and ISUC represent, respectively, the wear particles index and the wear severity index.

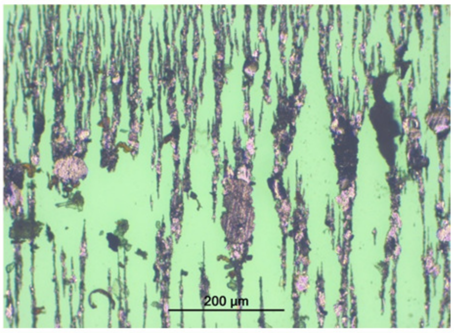

(a) Dilution: 0.1; Location: Core.

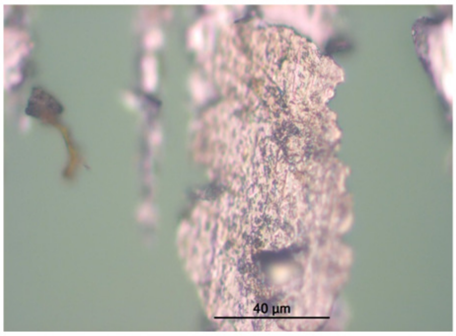

(b) Dilution: 0.1; Location: Core.

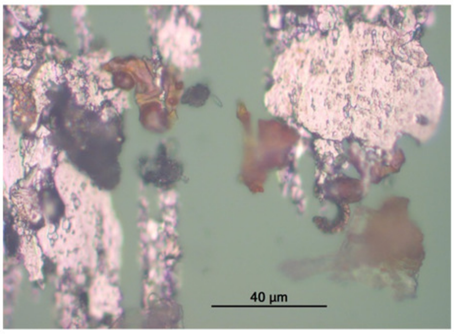

(c) Dilution: 0.1; Location: Core.

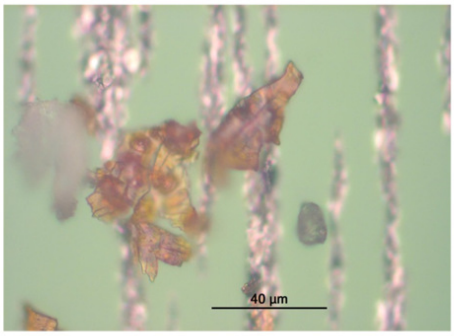

(d) Dilution: 0.1; Location: Middle.

Figure 7.20.: Ferrography images: MINR.

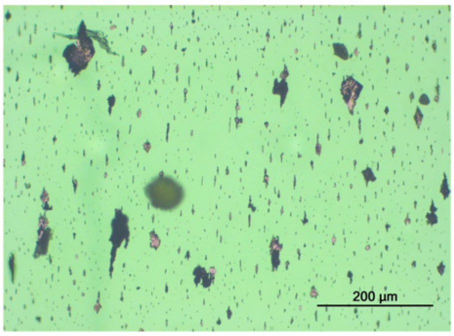

(a) Dilution: 1; Location: Core.

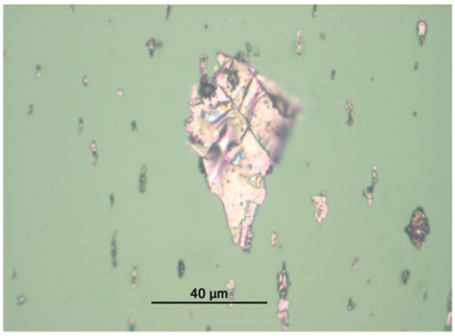

(b) Dilution: 1; Location: Core.

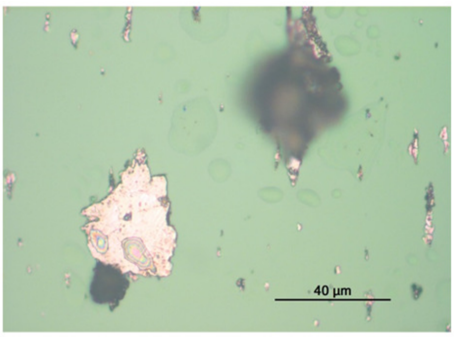

(c) Dilution: 1; Location: Core.

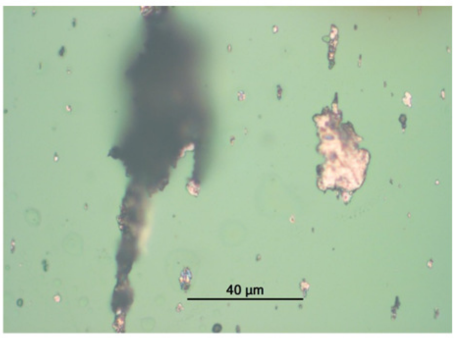

(d) Dilution: 1; Location: Core.

Figure 7.21.: Ferrography images: PAGD.

Table 7.1.: Direct Reading Ferrography Results.

Oil	**Cycles**	d	D_S	D_L	**CPUC**	**ISUC**
PAOR	**924000**	0.1	3.4	25.9	293.0	6.6E+04
MINR	247500	0.1	13.4	45.8	592.0	1.9E+05
MINE	247500	1.0	27.0	88.9	115.9	7.2E+03
PAGD	247500	1.0	9.2	17.0	26.2	2.0E+02

For both wear indexes, PAGD showed to be the best oil, followed by MINE. The PAOR sample analyzed was the one collected after the sixteen test grid and therefore had more than three times the number of cycles and even so, it showed better wear indexes than MINR.

In terms of gear wear and oil degradation, the PAGD showed the lowest wear indexes, even though it showed some premature thermal oxide formation. MINE had good results in the direct reading ferrography, but the analytical ferrography indicates relevant fatigue wear particles. MINR had the worst values in the wear indexes and the analytical ferrography showed a premature oil degradation. PAOR results are not directly comparable to the rest of the oils, but considering the amount of cycles and the working conditions it has supported, the results are satisfactory.

7.5.2. Numerical Results

Using the numerical results, one operating condition was selected to plot the power losses of each gearbox component, in order to evaluate each oil performance in what regards gears, roller bearings and seals. The selected operating condition was the 150rpm/2800Nm (S1), for being the *key point* of the 5 test grids and for being the closest comparison in terms of tangential speed and Hertz pressure (see table 3.3).

The percentages of each component in terms of power loss are represented in figure 7.22. These percentages are towards the operating power input.

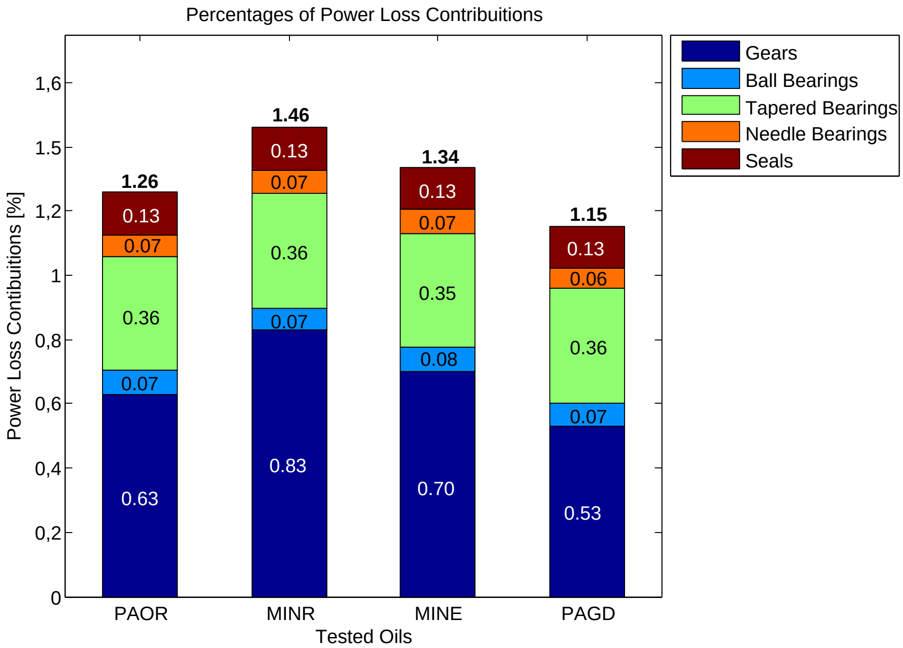

Figure 7.22.: Percentages of Power Loss Contributions.

In terms of total power loss, the numeric results indicate that PAGD is the most efficient oil. Nevertheless, it was already concluded that the numerical values of PAGD deviate more from the experimental then the other oils, as the model does not consider the churning losses. For the rest of the oils, the total power loss follows the stabilization temperature tendency: PAOR is better than MINE, which in turn outperforms than MINR (see figure 7.14).

In what concerns the power losses of each component, the comparison between oils indicates that at the selected operating conditions, the efficiency differences found are almost exclusively related to the gear losses. PAGD showed the lowest values on gear losses, followed by PAOR and MINE. MINR is the oil which leads to the highest values of gear losses.

The roller bearing losses do not vary from one oil to another. Although there are slight differences, they are always about 0.01%, and therefore the differences can be neglected.

The seals show a perfectly constant value, which was expected since according to equation (5.7.1) the seals only depend on the shaft diameter and the rotational speed.

It was also possible to compare the coefficient of friction in the meshing line of both Sun-Planet and Planet-Ring contacts, which are presented in figure 7.23.

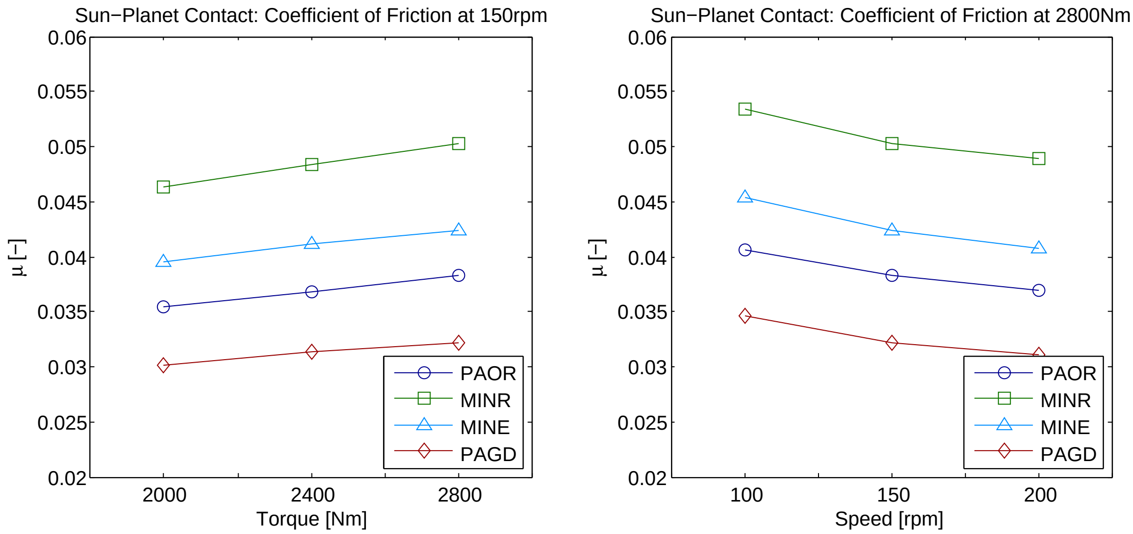

(a) Sun-Planet Contact.

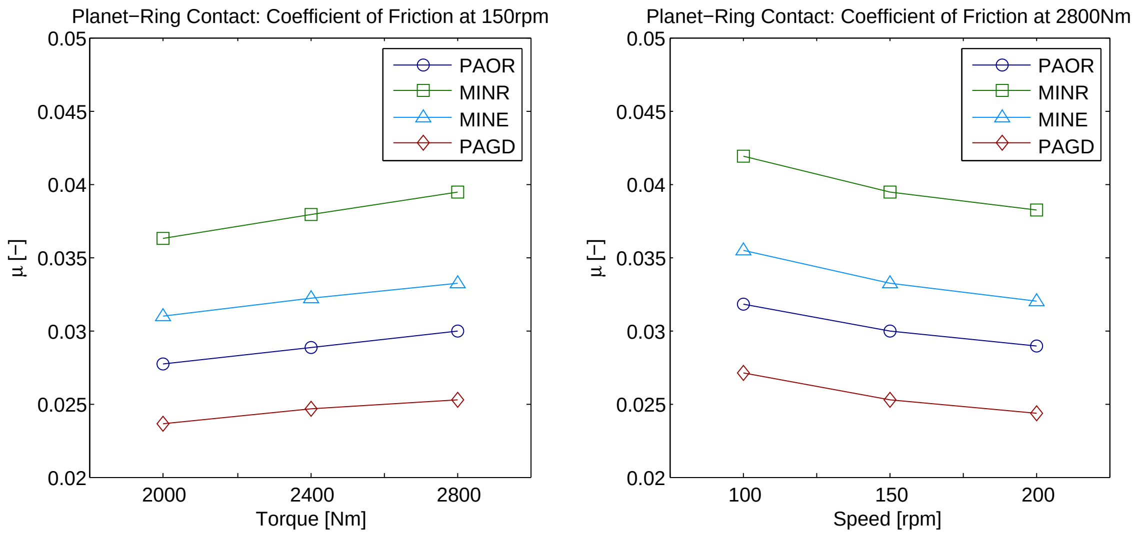

(b) Planet-Ring Contact.

Figure 7.23.: Oil comparison: Coefficient of friction.

The coefficient of friction comparison between oils is very clear: PAGD leads to the lowest coefficient of friction, followed by PAOR and MINE, respectively, while MINR lead to the highest value. This explains the differences found in the gears losses represented in figure 7.22. In the other hand, it is possible to conclude that when using PAGD, the reduction in gear losses due to the lower friction coefficient is not enough to compensate the higher churning losses, as the PAGD stabilization temperature is higher than PAOR and MINE.

The coefficient of friction has a inverted relation to the operating dynamic viscosity (figure 7.16). It is possible to verify that the oils with the highest dynamic viscosity lead to the lowest coefficient of friction.

The Sun-Planet contact and the Planet-Ring contact present the same tendencies in what regards the coefficient of friction: it increases with increasing torque, and decreases with increasing speed. Although presenting the same tendencies, the coefficient of friction in the Planet-Ring contact was always lower than in the Sun-Planet contact, due to its higher equivalent radius and lower line load.

The numerical values of αA for the tested oils were plotted in figure 7.24. The values considered were for the operating direction S1.

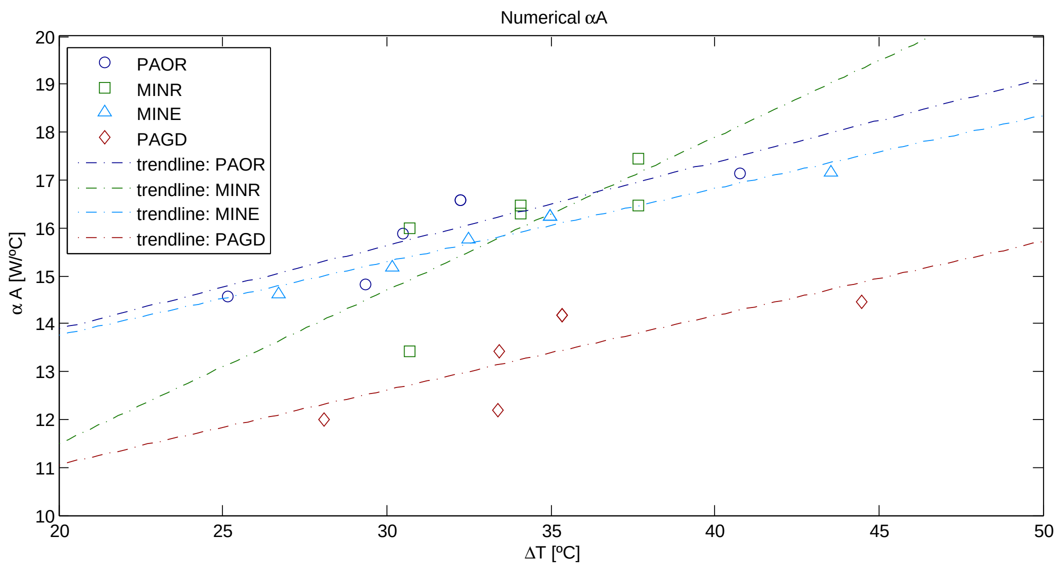

Figure 7.24.: Heat transfer coefficient: numerical values.

The trendlines were considered to be linear ($y = p_1 x + p_2$). The values of the coefficients p_1 and p_2 are represented in table 7.2, as well as the norm of residuals.

Table 7.2.: Trendline coefficients and norm of residuals.

Oil	p_1	p_2	Norm of Residuals
PAOR	0.1742	10.4038	1.1373
MINE	0.1531	10.6973	0.3881
MINR	0.3199	5.0972	2.0643
PAGD	0.1554	7.9502	1.5177

In what concerns the trends of each oil values, it is possible to observe that PAOR and MINE have very close trends, which slightly diverge with increasing stabilization temperature. PAGD showed a similar slope (p_1), although the starting point (p_2) is nearly half when compared to PAOR and MINE. This is due to the fact that the churning losses are not considered in the numerical results, and they are specially relevant for PAGD. MINR showed a completely different trend compared to the other three oils: it has a more accentuated slope, roughly twice, and a starting point that stands in the middle of PAGD and MINE.

Regarding the scattering of each oil plot, it is visible that MINR had the worst correlation, followed by PAGD, each one with a norm of residuals higher than 1.5. PAOR had a good correlation, with a norm of residuals of 1.1, while MINE had the best correlation with a norm of residual of 0.4.

8. Additional tests

The power loss differences found between the directions S1 and S2, which were followed by an increase of the operating temperature raised some doubts in the analysis of the results. At first, the increase of the operating temperature was assigned to be a consequence of having another 90min of test after the 240min test was carried out. After that, it was found that the stabilization temperature also suffered an increase. At this point, two hypothesis were available to explain the differences in both power loss and stabilization temperature:

- The gearbox could have different efficiencies for each direction, implying different values of power loss and stabilization temperature;
- The increase of the stabilization temperature could be a consequence of a malfunction in the data acquisition when the test rig was restarted.

In order to clarify these behaviors, PAOR was reintroduced in the gearbox and two tests (100rpm/2800Nm and 150rpm/2800Nm) were carried out but with switched operating directions: at first the gearbox worked as a reducer (S2) and after as multiplier (S1). The new tests were compared with the tests performed for the sixteen and five test grid. The evolution of the operating temperature and the difference between oil and room temperature were plotted through all the 330min and are represented in figure 8.1 and 8.2.

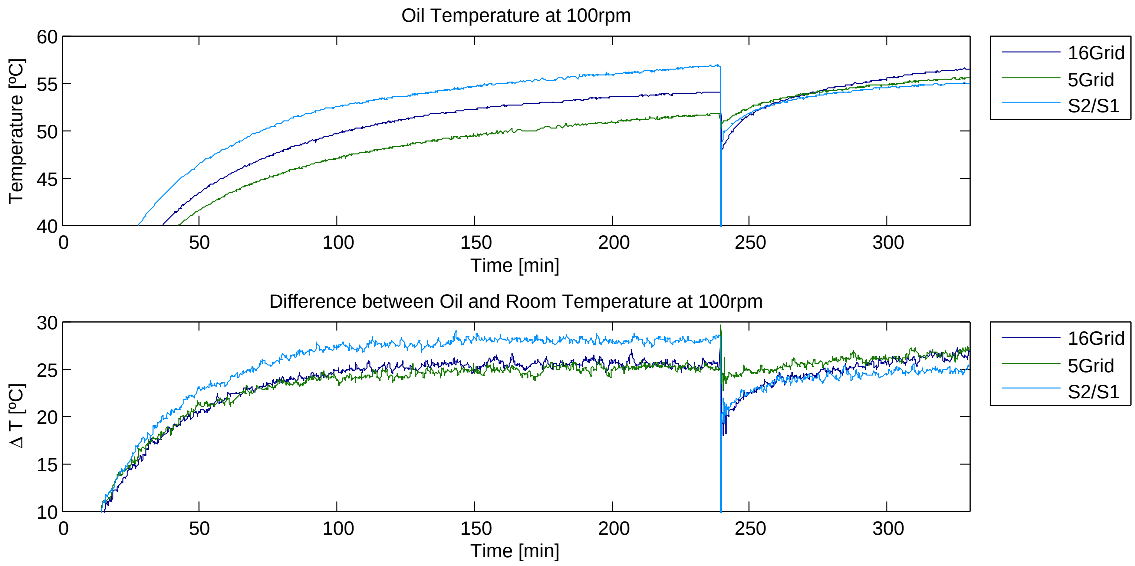

Figure 8.1.: Temperatures evolution at the 100rpm test.

For the 100rpm test, see figure 8.1, the operating temperatures of the sixteen and the five test grid results did not match for the first part of the test. In the second part of the test, the three operating temperatures were quite close. Nevertheless, the operating temperature of the S2/S1 test was higher than the other two in the first part, and lower in the second.

In what concerns to the stabilization temperature, the sixteen and five grid test had the same stabilization temperature in the first part of the test. In the second, the stabilization temperature starts at a different value, as the time taken to restart the test rig was probably different, but merged into the same value of stabilization temperature. As for the test with inverted directions, the stabilization temperature was higher than the other two for the first part (S2), and lower for the second (S1).

Aiming to validate the hypothesis of different efficiencies for different operating directions, the 150rpm/2800Nm was carried out. The temperatures are represented in figure 8.2.

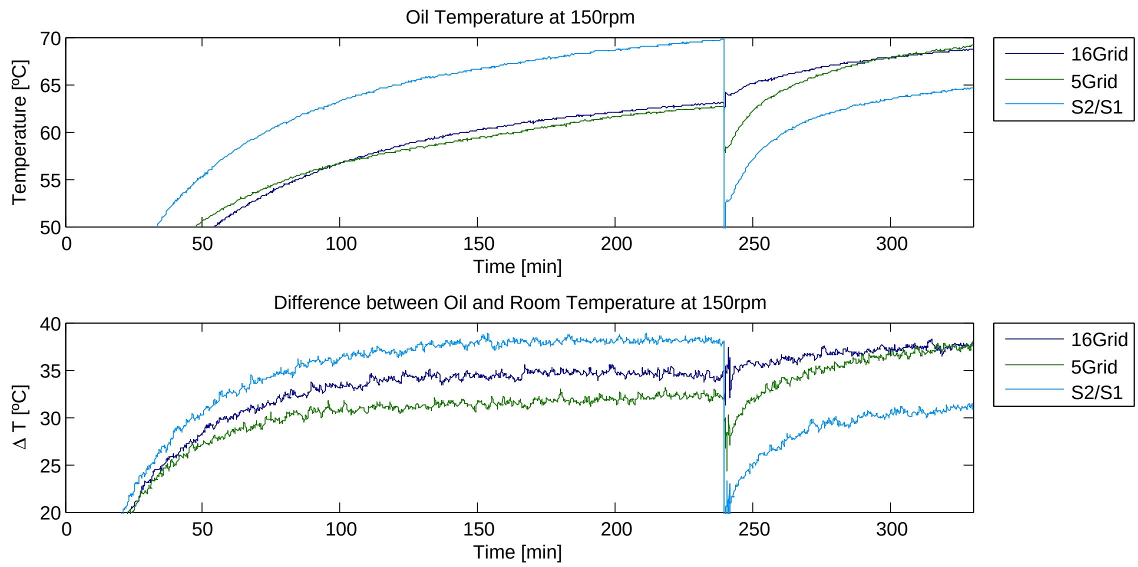

Figure 8.2.: Temperatures evolution at the 150rpm test.

In this case, the results leave no doubt. The operating temperature of the sixteen and five grid tests had very similar values in the first part of the test. In the second part the operating temperature starts at a different value, due to the different stopping time, but converge to the same values after a while. The test carried out with inverted directions was clearly different from the other two: higher operating temperature in the first part (S2) and lower in the second (S1).

As for the stabilization temperature, the values for the sixteen and five grid test are not a match in the first part of the test, but converge to the same value in the second. The stabilization temperature of the inverted direction test was again higher than the other two in the first part and lower in the second.

According to this results, the tested gearbox at this working conditions has different efficiencies for both operating directions being more efficient when working as a multiplier.

The differences in efficiency can be explained by the power flow through the components and/or the churning losses.

The two main sources of power loss found where the gears and the tapered roller bearings. When working as a multiplier, the power in the gearbox goes through the gears first, and then through the tapered roller bearings; as a reducer, the power flows in the other way around. The differences of the power flow in the gearbox can be one of the causes for different efficiencies. One way to verify it would be to reprogram the numerical model in order to take into account the successive power losses from one component to another.

The churning losses can have different values for different operating directions, as churning losses are related to the fluid motion, which can be different in both direction for a multitude of reasons: for instance, a non-symmetrical housing or display of components inside the gearbox could be enough to lead to different churning losses values [30].

While analyzing the temperature evolution for the three tests considered in this chapter, a curious fact stand out. While plotting the wall temperature along side with the oil temperature, they seem to diverge or converge according to the operating direction. The results are shown in figure 8.3.

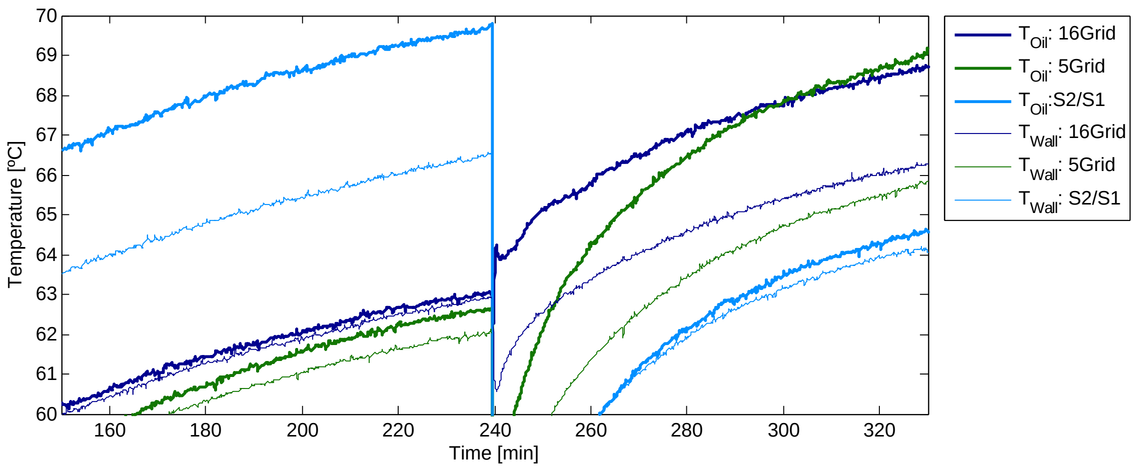

Figure 8.3.: Wall and Oil temperature evolution.

The oil and wall temperatures seem to converge to the same value when the gearbox works as a multiplier, and seem to diverge when it works as a reducer. The wall temperature sensor is not placed in plane of symmetry of the gearbox (see figure 3.4), and with different working direction the fluid flow inside the gearbox can be considerably different for each operating direction, meaning that in one direction the amount of fluid near to the oil sensor is higher than in the other, therefore leading the wall temperature to be close to the oil temperature in one direction, and to be significantly different in the other.

Part IV.

Conclusions and Future Work

9. Conclusions

9.1. Conclusions based on experimental results

PAOR showed to lead to the lowest values of stabilization temperature. MINR led to the highest stabilization temperatures, except for the test at 100rpm, where the highest temperature was achieved with PAGD. The differences between oils never exceeded $7°C$.

In terms of operating temperature, MINE showed the lowest values. PAOR showed to be more sensitive to both speed and torque increase than PAGD, both standing between the two mineral based oils, with MINR reaching the highest operating temperatures. The differences found were maximum at the most severe conditions, and were about $10°C$.

As for the operating viscosity, MINR had the lowest values in both kinematic and dynamic viscosity. The other three oils behave similarly, with MINE being the oil with the highest kinematic viscosity and PAGD being the one with the highest dynamic viscosity, due to its high density. In the other hand, viscosity has an important influence in the specific film thickness.

In what regards to the specific film thickness, MINE had the highest values and MINR had the lowest. PAOR and PAGD stood in between, with PAOR showing better results at lower power levels, and PAGD achieving higher specific film thickness at higher power levels.

PAGD achieved the lowest values for the coefficient of friction while MINR had the highest. PAOR and MINE stood in between, although PAOR had lower values than MINE.

In what concerns the wear indexes, specially the severity wear index, PAGD presented values significantly better than the other oils. MINE showed a considerable amount of particles typical of fatigue wear and MINR had particles indicating a premature oil degradation.

The additional tests results allow one to conclude that the tested gearbox has different efficiency for both operating directions in the ranged operating conditions. Additional temperature readings reveal that the fluid flow in the gearbox has great influences in the temperature values.

9.2. Conclusions based on numerical results

The numerical values for power loss and efficiency stood between the two experimental readings in most cases. The only significant exception was PAGD and the high speed tests (200 and 250rpm) for the sixteen test grid.

The differences found between the experimental readings and the numerical values are explained by the churning losses, which the numerical model doesn't take into account. The churning losses are particularly relevant for high operating speeds and for PAGD, as it is denser than the other oils.

The numerical values showed that the power loss is more sensitive to speed than to the torque, and the experimental results validate this prediction.

In terms of component losses, the numerical model showed that at the ranged working conditions, the gears are the most significant power loss source, except for the lowest torque applied (1600Nm), where the tapered roller bearings are the main power loss source.

For the same working conditions, the numerical results indicate that PAGD had the lowest power loss. The lowest value of PAGD power loss is due to its lowest gear losses which are justified by the experimental results for the gear coefficient of friction of PAGD. The rest of the components have nearly the same losses for the tested oils. The gears losses vary accordingly to the coefficient of friction obtained for each oil.

The churning losses seem to be quite relevant, specially for PAGD which despite showing the lowest coefficient of friction in the gears (most important source of power loss) it did not present the best power loss performance. The reduction of the friction in the gears is not big enough to overcome the increase in the churning losses relatively to the other lubricants.

For the sixteen test grid, the experimental values of the heat transfer coefficient showed a high dispersion of results, when compared to the numerical ones. The scattering indicates a measurement uncertainty in the torque sensors or indicates that the stabilization temperature, by it self, is not enough to ascertain the power loss.

10. Future Works

The repeatability of the tests could not be assured, specially in terms of torque measurements. The torque sensors accuracy should be checked and the tests carried out should be repeated with higher reliability in the results.

The scattering visible on the heat transfer coefficients determined with the experimental power loss results is big enough to justify the introduction of a relative humidity sensor in the test rig. The thermal conductibility of the air significantly changes with the water vapor presence and therefore, two temperature readings are not enough to accurately ascertain the power loss of a gear box. Additional tests should be carried out in order to obtain a more realistic equation regarding other air properties, as relative humidity.

The power loss model should be re-built in order to consider successive power losses as the power flows through the gearbox. The efficiency differences found experimentally should be compared to that new version of the model, attempting to comprehend why the gearbox shows different efficiency for both operating directions.

The churning losses and the fluid flow seem to be a relevant part of the gearbox losses. A computational fluid dynamic (CFD) analysis should be carried out in order to predict the fluid motion and the churning losses. The CFD results could be partially validated by filming several tests with a thermographic camera, assuming that the fluid motion and temperature would be represented as a gradient temperature at the surface of the gearbox.

Bibliography

[1] D. Gonçalves. Efficiency of a gearbox lubricated with wind mill gear oils. Master's thesis, Faculdade de Engenharia da Universidade do Porto, 2011.

[2] P. Marques. Efficiency of a gearbox lubricated with wind mill gear oils. Master's thesis, Faculdade de Engenharia da Universidade do Porto, 2012.

[3] D. Pereira. Torque loss in a planetary multiplier gearbox: Influence of operating conditions and gear oil formulation. Master's thesis, Faculdade de Engenharia da Universidade do Porto, 2013.

[4] REN21. Renewables 2013 global status report, 2013.

[5] GWEC. Global wind report annual market update 2013, 2013.

[6] EWEA European Wind Energy Association. Wind energy factsheets, 2013.

[7] Magdi Ragheb Adam M. Ragheb. Fundamental and advanced topics in wind power. 2011-06-20.

[8] Hanspeter Dinner. KISSsoft:-Wind Turbine Gearbox Calculation, April 2010.

[9] World Energy Council. Energy efficiency indicators, 2011.

[10] B.-R. Höhn, K. Michaelis, and T. Vollmer. Thermal rating of gear drives: Balance between power loss and heat dissipation. *AGMA Technical Paper*, 1996.

[11] B.-R. Höhn, K. Michaelis, and M. Hinterstoißer. Optimization of gearbox efficiency. *goriva i maziva*, 48(4):462–480, 2009.

[12] Luís Magalhães, Ramiro Martins, Cristiano Locateli, and Jorge Seabra. Influence of tooth profile and oil formulation on gear power loss. *Tribology International*, 43(10):1861–1871, 2010. 36th Leeds-Lyon Symposium Special Issue: Multi-facets of Tribology.

[13] Carlos M.C.G. Fernandes, Pedro M. P. Amaro, Ramiro C. Martins, and Jorge H.O. Seabra. Torque loss in cylindrical roller thrust bearings lubricated with wind turbine gear oils at constant temperature. *Tribology International*, (0):under review, 2013.

[14] Carlos M.C.G. Fernandes, Ramiro C. Martins, and Jorge H.O. Seabra. Friction torque of thrust ball bearings lubricated with wind turbine gear oils. *Tribology International*, 58(0):47 – 54, 2013.

[15] Carlos M.C.G. Fernandes, Pedro M.P. Amaro, Ramiro C. Martins, and Jorge H.O. Seabra. Torque loss in thrust ball bearings lubricated with wind

turbine gear oils at constant temperature. *Tribology International*, 66(0):194 – 202, 2013.

[16] Carlos M.C.G. Fernandes, Ramiro C. Martins, and Jorge H.O. Seabra. Torque loss of type C40 FZG gears lubricated with wind turbine gear oils. *Tribology International*, (0):–, 2013.

[17] Pedro M.T. Marques, Carlos M.C.G. Fernandes, Ramiro C. Martins, and Jorge H.O. Seabra. Power losses at low speed in a gearbox lubricated with wind turbine gear oils with special focus on churning losses. *Tribology International*, 62(0):186 – 197, 2013.

[18] Deirdra Barr. Modern wind turbines: A lubrication challenge, Septmeber 2002.

[19] Determination of viscosity of bitumen emulsions - engler method.

[20] Astm d341 - 09, standard practice for viscosity - temperature charts for liquid petroleum products.

[21] J. Denis, J. Briant, and J.-C. Hipeaux. *Physico-Chimie des Lubrifiants - Analyses et Essais*. Éditions Technip, 1997.

[22] Matt McMahon Michael Barret. Analytical ferrography, October 2000.

[23] José A. Brandão, Mathilde Meheux, Fabrice Ville, Jorge H.O. Seabra, and Jorge Castro. Comparative overview of five gear oils in mixed and boundary film lubrication. *Tribology International*, 47(0):50 – 61, 2012.

[24] D. Dowson and G. R. Higginson. *Elasto-hydrodynamic Lubrication*. Pergamon Press, SI edition edition, 1977.

[25] D. Simner. Quantifying the potential fuel economy benefit of transmission lubricants. *Industrial and Automotive Lubrication*, 2:8, 1998.

[26] F. Roux. *Notion de tribologie, em La Lubrification Industrielle - Tome 1 - Transmissions Compresseurs, Turbines*. Publications de l'Institue Français du Pétrole, 1984.

[27] JP. W. Gold, A. Schmidt, H. dicke, H. Loos, and C. Aßmann. Viscosity-pressure-temperature behaviour of mineral and synthetic oils. *Journal of Synthetic Lubrication*, 18(1), 2001.

[28] L. Schlenk. *Unterscuchungen zur Fresstragfähigkeit von Grozahnrädern*. PhD thesis, Dissertation TU München, 1994.

[29] C. Changenet, G. Leprince, F. Ville, and P. Velex. A note on flow regimes and churning loss modeling. *Journal of Mechanical Design*, 133(12):121009, 2011.

[30] C. Changenet and P. Velex. Housing Influence on Churning Losses in Geared Transmissions. *Journal of Mechanical Design*, 130(6):062603, 2008.

[31] A. S. Terekhov. Hydraulic losses in gearboxes with oil immersion. *Vestn. Mashinostroeniya*, 55(5):13–17, 1975.

[32] R. J. Boness. Churning losses of discs and gears running partially submerged in oil. *Procedings of ASME International Power Transmission Gearing Conference*, 1:355–359, 1989.

[33] S. Seetharaman and A. Kahraman. Load-independent spin power losses of a spur gear pair: Model formulation. *Journal of Tribology*, 131(2):022201, 2009.

[34] Gauthier LePrince, Christophe Changenet, Fabrice Ville, Philippe Velex, Christophe Dufau, and Frédéric Jarnias. Influence of Aerated Lubricants on Gear Churning Losses - An Engineering model. *Tribology Transactions*, 54(6):929–938, 2011.

[35] F Concli and C Gorla. Computational and experimental analysis of the churning power losses in an industrial planetary speed reducer. In *9th International Conference on Advances in Fluid Mechanics-Advances in Fluid Mechanics IX, WIT Transactions on Engineering Sciences*, volume 74, pages 287–298, 2012.

[36] *SKF General Catalogue 6000 EN*. SKF, 2013.

[37] Eschmann Hasbargen Weigand. *Ball and Roller Bearings - Theory, Design, and Application*. Wiley, 1985.

[38] American Gear Manufacturers Association. Effect of lubrication on gear surface distress, agma 925-a03. *AGMA Information sheet*.

Appendix

A. Ring surface temperature tests

The temperatures readings of the additional tests have proven that the fluid flow inside the gearbox has a relevant influence in the temperatures measured in the oil sump and in the wall. Therefore, the gearbox was equipped with four thermocouples placed on the area exterior to the ring (see figure A.1) in an attempt to ascertain the ring temperatures, considering that part of the ring is immersed in the oil sump, an the other is not.

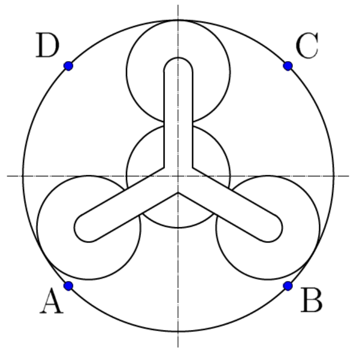

Figure A.1.: Thermocouples' positioning.

Three tests were performed at 150rpm/2800Nm. In two of them, the first working direction was S2 (reducer), and in the last one, the first operating direction was S1 (multiplier). The thermocouples' readings were recorded by two thermologgers; in different tests, the combination between thermocouples and thermologgers was changed, in order to verify the results repeatability. The results are shown in figure A.2, A.3 and A.4.

The repeatability of the temperature's readings was not verified: Between the first and the second tests (figures A.2 and A.3), the maximum and minimum temperature points switched positions; in the third test (figure A.4) is visible that in the second part of the test point A and C have different trends from point B and D. In this test, the thermocouples measuring point A and C were recorded by one thermologger, while thermocouples measuring point B and D were recorded by the other. The readings might be affected by a "thermologger factor", as there is no plausible explanation for the diagonal differences found.

Nevertheless, the temperature difference found between two points was higher than $10°C$ in two out of three cases, reinforcing the need to run additional tests aiming to clarify the fluid flow influence in the oil, wall and surface temperatures' behavior.

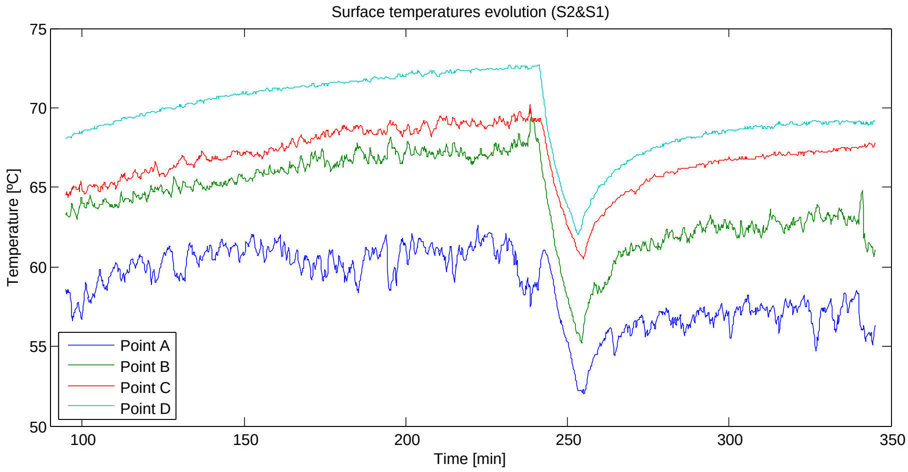

Figure A.2.: Surface temperatures in the area exterior to the ring (test: 1).

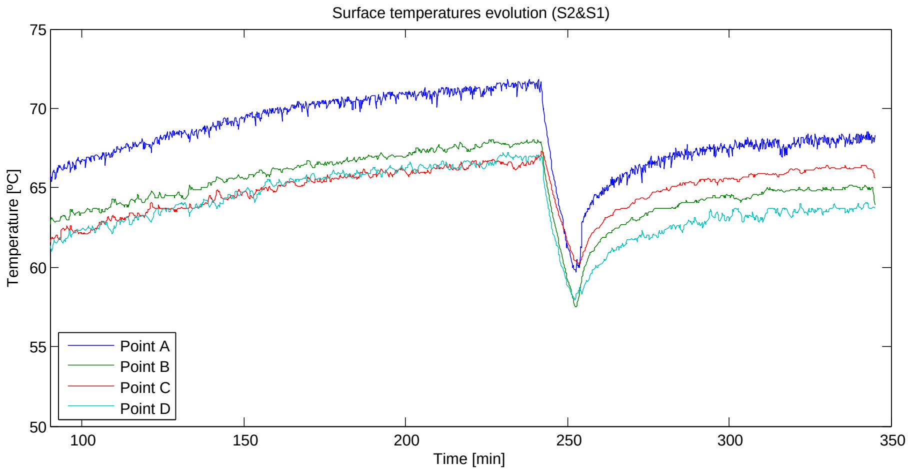

Figure A.3.: Surface temperatures in the area exterior to the ring (test: 2).

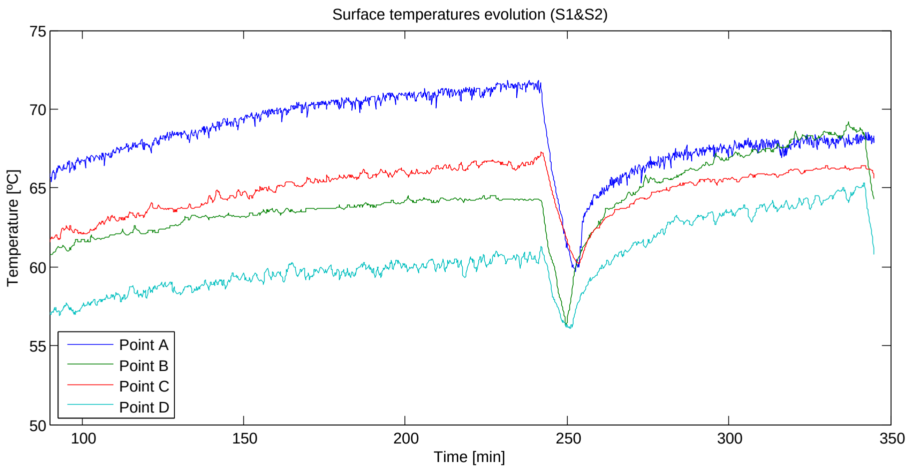

Figure A.4.: Surface temperatures in the area exterior to the ring (test: 3).

B. Test Reports

B.1. PAOR Oil: 16 Test Grid

Test Number:1	Date:05/03/2014	By: Raquel Camacho
Oil:	PAOR	
	Imposed Working Conditions:	**Units**
n_{in}	100	rpm
TQ_{in}	1600	Nm
$Test\ duration$	$240 + 90$	min

	S1: Multiplier Gearbox	
	Actual Working Conditions:	**Units**
n_1	102.6	rpm
TQ_1	1549.5	Nm
TQ_2	383.0	Nm
	Temperature readings:	**Units**
$T_{Oil\ M5}$	43.26	$°C$
$T_{Oil\ M12}$	44.80	$°C$
T_{Wall}	43.50	$°C$
T_{Amb}	25.18	$°C$
	Additional Information:	**Units**
$T_{Oil\ M5} - T_{Amb}$	18.08	$°C$
$Efficiency$	98.88	%
TQ_{Loss}	17.4	Nm

	S2: Reducer Gearbox	
	Actual Working Conditions:	**Units**
n_1	102.5	rpm
TQ_1	1549.5	Nm
TQ_2	395.9	Nm
	Temperature readings:	**Units**
$T_{Oil\ M5}$	45.12	$°C$
$T_{Oil\ M12}$	45.24	$°C$
T_{Wall}	44.04	$°C$
T_{Amb}	26.96	$°C$
	Additional Information:	**Units**
$T_{Oil\ M5} - T_{Amb}$	18.16	$°C$
$Efficiency$	97.86	%
TQ_{Loss}	33.9	Nm

Test Number:2	Date:06/03/2014	By: Raquel Camacho
Oil:	PAOR	
	Imposed Working Conditions:	**Units**
n_{in}	100	rpm
TQ_{in}	2000	Nm
$Test\ duration$	$240 + 90$	min

	S1: Multiplier Gearbox	
	Actual Working Conditions:	**Units**
n_1	99.7	rpm
TQ_1	1935.5	Nm
TQ_2	479.0	Nm
	Temperature readings:	**Units**
$T_{Oil\ M5}$	46.07	$°C$
$T_{Oil\ M12}$	46.92	$°C$
T_{Wall}	45.81	$°C$
T_{Amb}	27.12	$°C$
	Additional Information:	**Units**
$T_{Oil\ M5} - T_{Amb}$	18.96	$°C$
$Efficiency$	99.00	%
TQ_{Loss}	19.4	Nm

	S2: Reducer Gearbox	
	Actual Working Conditions:	**Units**
n_1	99.7	rpm
TQ_1	1935.2	Nm
TQ_2	491.9	Nm
	Temperature readings:	**Units**
$T_{Oil\ M5}$	48.16	$°C$
$T_{Oil\ M12}$	47.69	$°C$
T_{Wall}	46.52	$°C$
T_{Amb}	28.78	$°C$
	Additional Information:	**Units**
$T_{Oil\ M5} - T_{Amb}$	19.38	$°C$
$Efficiency$	98.34	%
TQ_{Loss}	32.6	Nm

Test Number:3	Date:07/03/2014	By: Raquel Camacho
Oil:	PAOR	
	Imposed Working Conditions:	**Units**
n_{in}	100	rpm
TQ_{in}	2400	Nm
$Test\ duration$	$240 + 90$	min

	S1: Multiplier Gearbox	
	Actual Working Conditions:	**Units**
n_1	99.7	rpm
TQ_1	2321.5	Nm
TQ_2	573.6	Nm
	Temperature readings:	**Units**
$T_{Oil\ M5}$	47.58	$°C$
$T_{Oil\ M12}$	48.38	$°C$
T_{Wall}	47.02	$°C$
T_{Amb}	26.96	$°C$
	Additional Information:	**Units**
$T_{Oil\ M5} - T_{Amb}$	20.62	$°C$
$Efficiency$	98.83	%
TQ_{Loss}	27.2	Nm

	S2: Reducer Gearbox	
	Actual Working Conditions:	**Units**
n_1	99.7	rpm
TQ_1	2320.6	Nm
TQ_2	588.5	Nm
	Temperature readings:	**Units**
$T_{Oil\ M5}$	51.03	$°C$
$T_{Oil\ M12}$	50.11	$°C$
T_{Wall}	48.80	$°C$
T_{Amb}	29.79	$°C$
	Additional Information:	**Units**
$T_{Oil\ M5} - T_{Amb}$	21.24	$°C$
$Efficiency$	98.58	%
TQ_{Loss}	33.4	Nm

Test Number:4	Date:10/03/2014	By: Raquel Camacho
Oil:	PAOR	
	Imposed Working Conditions:	**Units**
n_{in}	150	rpm
TQ_{in}	1600	Nm
$Test\ duration$	$240 + 90$	min

	S1: Multiplier Gearbox	
	Actual Working Conditions:	**Units**
n_1	149.9	rpm
TQ_1	1549.8	Nm
TQ_2	381.6	Nm
	Temperature readings:	**Units**
$T_{Oil\ M5}$	55.59	$°C$
$T_{Oil\ M12}$	57.79	$°C$
T_{Wall}	56.74	$°C$
T_{Amb}	31.12	$°C$
	Additional Information:	**Units**
$T_{Oil\ M5} - T_{Amb}$	24.47	$°C$
$Efficiency$	98.48	%
TQ_{Loss}	23.5	Nm

	S2: Reducer Gearbox	
	Actual Working Conditions:	**Units**
n_1	149.9	rpm
TQ_1	1549.0	Nm
TQ_2	393.5	Nm
	Temperature readings:	**Units**
$T_{Oil\ M5}$	58.59	$°C$
$T_{Oil\ M12}$	58.77	$°C$
T_{Wall}	57.73	$°C$
T_{Amb}	33.73	$°C$
	Additional Information:	**Units**
$T_{Oil\ M5} - T_{Amb}$	24.85	$°C$
$Efficiency$	98.40	%
TQ_{Loss}	25.2	Nm

Test Number:5	Date:11/03/2014	By: Raquel Camacho
Oil:	PAOR	
	Imposed Working Conditions:	**Units**
n_{in}	150	rpm
TQ_{in}	2000	Nm
$Test\ duration$	$240 + 90$	min

	S1: Multiplier Gearbox	
	Actual Working Conditions:	**Units**
n_1	149.9	rpm
TQ_1	1936.4	Nm
TQ_2	475.7	Nm
	Temperature readings:	**Units**
$T_{Oil\ M5}$	61.00	$°C$
$T_{Oil\ M12}$	62.31	$°C$
T_{Wall}	61.11	$°C$
T_{Amb}	31.07	$°C$
	Additional Information:	**Units**
$T_{Oil\ M5} - T_{Amb}$	29.93	$°C$
$Efficiency$	98.26	%
TQ_{Loss}	33.6	Nm

	S2: Reducer Gearbox	
	Actual Working Conditions:	**Units**
n_1	150.6	rpm
TQ_1	1935.8	Nm
TQ_2	490.7	Nm
	Temperature readings:	**Units**
$T_{Oil\ M5}$	64.04	$°C$
$T_{Oil\ M12}$	64.06	$°C$
T_{Wall}	62.75	$°C$
T_{Amb}	34.49	$°C$
	Additional Information:	**Units**
$T_{Oil\ M5} - T_{Amb}$	29.55	$°C$
$Efficiency$	98.62	%
TQ_{Loss}	27.0	Nm

Test Number:6	Date:12/03/2014	By: Raquel Camacho
Oil:	PAOR	
	Imposed Working Conditions:	**Units**
n_{in}	150	rpm
TQ_{in}	2400	Nm
$Test\ duration$	$240 + 90$	min

	S1: Multiplier Gearbox	
	Actual Working Conditions:	**Units**
n_1	149.9	rpm
TQ_1	2322.3	Nm
TQ_2	571.7	Nm
	Temperature readings:	**Units**
$T_{Oil\ M5}$	63.29	$°C$
$T_{Oil\ M12}$	64.00	$°C$
T_{Wall}	62.89	$°C$
T_{Amb}	32.13	$°C$
	Additional Information:	**Units**
$T_{Oil\ M5} - T_{Amb}$	31.16	$°C$
$Efficiency$	98.46	%
TQ_{Loss}	35.7	Nm

	S2: Reducer Gearbox	
	Actual Working Conditions:	**Units**
n_1	149.8	rpm
TQ_1	2321.7	Nm
TQ_2	588.6	Nm
	Temperature readings:	**Units**
$T_{Oil\ M5}$	68.60	$°C$
$T_{Oil\ M12}$	68.57	$°C$
T_{Wall}	67.23	$°C$
T_{Amb}	34.80	$°C$
	Additional Information:	**Units**
$T_{Oil\ M5} - T_{Amb}$	33.80	$°C$
$Efficiency$	98.61	%
TQ_{Loss}	32.7	Nm

Test Number:7	Date:13/03/2014	By: Raquel Camacho
Oil:	PAOR	
	Imposed Working Conditions:	**Units**
n_{in}	200	rpm
TQ_{in}	1600	Nm
$Test\ duration$	$240 + 90$	min
	S1: Multiplier Gearbox	
	Actual Working Conditions:	**Units**
n_1	200.7	rpm
TQ_1	1549.2	Nm
TQ_2	379.3	Nm
	Temperature readings:	**Units**
$T_{Oil\ M5}$	68.44	$°C$
$T_{Oil\ M12}$	69.50	$°C$
T_{Wall}	68.97	$°C$
T_{Amb}	31.27	$°C$
	Additional Information:	**Units**
$T_{Oil\ M5} - T_{Amb}$	37.17	$°C$
$Efficiency$	97.94	%
TQ_{Loss}	32.0	Nm
	S2: Reducer Gearbox	
	Actual Working Conditions:	**Units**
n_1	200.0	rpm
TQ_1	1547.2	Nm
TQ_2	393.0	Nm
	Temperature readings:	**Units**
$T_{Oil\ M5}$	70.63	$°C$
$T_{Oil\ M12}$	73.72	$°C$
T_{Wall}	72.68	$°C$
T_{Amb}	33.55	$°C$
	Additional Information:	**Units**
$T_{Oil\ M5} - T_{Amb}$	37.07	$°C$
$Efficiency$	98.41	%
TQ_{Loss}	25.0	Nm

Test Number:8	Date:14/03/2014	By: Raquel Camacho
Oil:	PAOR	
	Imposed Working Conditions:	**Units**
n_{in}	200	rpm
TQ_{in}	2000	Nm
$Test\ duration$	$240 + 90$	min

	S1: Multiplier Gearbox	
	Actual Working Conditions:	**Units**
n_1	201.8	rpm
TQ_1	1935.8	Nm
TQ_2	475.4	Nm
	Temperature readings:	**Units**
$T_{Oil\ M5}$	72.85	$°C$
$T_{Oil\ M12}$	73.06	$°C$
T_{Wall}	72.63	$°C$
T_{Amb}	31.75	$°C$
	Additional Information:	**Units**
$T_{Oil\ M5} - T_{Amb}$	41.10	$°C$
$Efficiency$	98.24	%
TQ_{Loss}	34.1	Nm

	S2: Reducer Gearbox	
	Actual Working Conditions:	**Units**
n_1	200.2	rpm
TQ_1	1940.8	Nm
TQ_2	492.8	Nm
	Temperature readings:	**Units**
$T_{Oil\ M5}$	74.48	$°C$
$T_{Oil\ M12}$	77.34	$°C$
T_{Wall}	76.32	$°C$
T_{Amb}	34.04	$°C$
	Additional Information:	**Units**
$T_{Oil\ M5} - T_{Amb}$	40.44	$°C$
$Efficiency$	98.46	%
TQ_{Loss}	30.3	Nm

Test Number:9	Date:17/03/2014	By: Raquel Camacho
Oil:	PAOR	
	Imposed Working Conditions:	**Units**
n_{in}	200	rpm
TQ_{in}	2400	Nm
$Test\ duration$	$240 + 90$	min
	S1: Multiplier Gearbox	
	Actual Working Conditions:	**Units**
n_1	201.8	rpm
TQ_1	2322.3	Nm
TQ_2	571.3	Nm
	Temperature readings:	**Units**
$T_{Oil\ M5}$	74.82	$°C$
$T_{Oil\ M12}$	74.63	$°C$
T_{Wall}	74.15	$°C$
T_{Amb}	31.26	$°C$
	Additional Information:	**Units**
$T_{Oil\ M5} - T_{Amb}$	43.55	$°C$
$Efficiency$	98.40	%
TQ_{Loss}	37.2	Nm
	S2: Reducer Gearbox	
	Actual Working Conditions:	**Units**
n_1	200.0	rpm
TQ_1	2319.6	Nm
TQ_2	589.2	Nm
	Temperature readings:	**Units**
$T_{Oil\ M5}$	78.11	$°C$
$T_{Oil\ M12}$	80.82	$°C$
T_{Wall}	79.77	$°C$
T_{Amb}	33.27	$°C$
	Additional Information:	**Units**
$T_{Oil\ M5} - T_{Amb}$	44.84	$°C$
$Efficiency$	98.42	%
TQ_{Loss}	37.1	Nm

Test Number:10	Date:18/03/2014	By: Raquel Camacho
Oil:	PAOR	
	Imposed Working Conditions:	**Units**
n_{in}	250	rpm
TQ_{in}	1600	Nm
$Test\ duration$	$240 + 90$	min

	S1: Multiplier Gearbox	
	Actual Working Conditions:	**Units**
n_1	250.4	rpm
TQ_1	1549.0	Nm
TQ_2	377.5	Nm
	Temperature readings:	**Units**
$T_{Oil\ M5}$	82.08	$°C$
$T_{Oil\ M12}$	82.64	$°C$
T_{Wall}	82.38	$°C$
T_{Amb}	32.82	$°C$
	Additional Information:	**Units**
$T_{Oil\ M5} - T_{Amb}$	49.26	$°C$
$Efficiency$	97.48	%
TQ_{Loss}	39.1	Nm

	S2: Reducer Gearbox	
	Actual Working Conditions:	**Units**
n_1	250.5	rpm
TQ_1	1550.1	Nm
TQ_2	395.0	Nm
	Temperature readings:	**Units**
$T_{Oil\ M5}$	84.69	$°C$
$T_{Oil\ M12}$	87.40	$°C$
T_{Wall}	86.50	$°C$
T_{Amb}	35.00	$°C$
	Additional Information:	**Units**
$T_{Oil\ M5} - T_{Amb}$	49.70	$°C$
$Efficiency$	98.10	%
TQ_{Loss}	30.0	Nm

Test Number:11	Date:19/03/2014	By: Raquel Camacho
Oil:	PAOR	
	Imposed Working Conditions:	**Units**
n_{in}	250	rpm
TQ_{in}	2000	Nm
$Test\ duration$	$240 + 90$	min

	S1: Multiplier Gearbox	
	Actual Working Conditions:	**Units**
n_1	250.5	rpm
TQ_1	1935.7	Nm
TQ_2	475.5	Nm
	Temperature readings:	**Units**
$T_{Oil\ M5}$	85.78	$^\circ C$
$T_{Oil\ M12}$	84.92	$^\circ C$
T_{Wall}	84.62	$^\circ C$
T_{Amb}	34.07	$^\circ C$
	Additional Information:	**Units**
$T_{Oil\ M5} - T_{Amb}$	51.71	$^\circ C$
$Efficiency$	98.26	%
TQ_{Loss}	33.7	Nm

	S2: Reducer Gearbox	
	Actual Working Conditions:	**Units**
n_1	250.5	rpm
TQ_1	1935.9	Nm
TQ_2	492.3	Nm
	Temperature readings:	**Units**
$T_{Oil\ M5}$	86.70	$^\circ C$
$T_{Oil\ M12}$	88.37	$^\circ C$
T_{Wall}	87.71	$^\circ C$
T_{Amb}	36.87	$^\circ C$
	Additional Information:	**Units**
$T_{Oil\ M5} - T_{Amb}$	49.84	$^\circ C$
$Efficiency$	98.32	%
TQ_{Loss}	33.1	Nm

Test Number:12	Date:20/03/2014	By: Raquel Camacho
Oil:	PAOR	
	Imposed Working Conditions:	**Units**
n_{in}	250	rpm
TQ_{in}	2400	Nm
$Test\ duration$	$240 + 90$	min

	S1: Multiplier Gearbox	
	Actual Working Conditions:	**Units**
n_1	250.5	rpm
TQ_1	2321.6	Nm
TQ_2	572.0	Nm
	Temperature readings:	**Units**
$T_{Oil\ M5}$	88.02	$°C$
$T_{Oil\ M12}$	86.55	$°C$
T_{Wall}	86.47	$°C$
T_{Amb}	34.32	$°C$
	Additional Information:	**Units**
$T_{Oil\ M5} - T_{Amb}$	53.70	$°C$
$Efficiency$	98.55	%
TQ_{Loss}	33.6	Nm

	S2: Reducer Gearbox	
	Actual Working Conditions:	**Units**
n_1	250.5	rpm
TQ_1	2322.4	Nm
TQ_2	589.1	Nm
	Temperature readings:	**Units**
$T_{Oil\ M5}$	89.71	$°C$
$T_{Oil\ M12}$	90.15	$°C$
T_{Wall}	90.14	$°C$
T_{Amb}	36.86	$°C$
	Additional Information:	**Units**
$T_{Oil\ M5} - T_{Amb}$	52.85	$°C$
$Efficiency$	98.56	%
TQ_{Loss}	33.9	Nm

Test Number:13	Date:21/03/2014	By: Raquel Camacho
Oil:	PAOR	
	Imposed Working Conditions:	**Units**
n_{in}	100	rpm
TQ_{in}	2800	Nm
$Test\ duration$	$240 + 90$	min

	S1: Multiplier Gearbox	
	Actual Working Conditions:	**Units**
n_1	99.7	rpm
TQ_1	2708.6	Nm
TQ_2	667.6	Nm
	Temperature readings:	**Units**
$T_{Oil\ M5}$	53.84	$°C$
$T_{Oil\ M12}$	53.86	$°C$
T_{Wall}	52.26	$°C$
T_{Amb}	28.40	$°C$
	Additional Information:	**Units**
$T_{Oil\ M5} - T_{Amb}$	25.44	$°C$
$Efficiency$	98.59	%
TQ_{Loss}	38.2	Nm

	S2: Reducer Gearbox	
	Actual Working Conditions:	**Units**
n_1	99.7	rpm
TQ_1	2708.7	Nm
TQ_2	685.6	Nm
	Temperature readings:	**Units**
$T_{Oil\ M5}$	56.24	$°C$
$T_{Oil\ M12}$	55.36	$°C$
T_{Wall}	53.50	$°C$
T_{Amb}	29.92	$°C$
	Additional Information:	**Units**
$T_{Oil\ M5} - T_{Amb}$	26.32	$°C$
$Efficiency$	98.77	%
TQ_{Loss}	33.6	Nm

Test Number:14	Date:24/03/2014	By: Raquel Camacho
Oil:	PAOR	
	Imposed Working Conditions:	**Units**
n_{in}	150	rpm
TQ_{in}	2800	Nm
$Test\ duration$	$240 + 90$	min

	S1: Multiplier Gearbox	
	Actual Working Conditions:	**Units**
n_1	149.8	rpm
TQ_1	2708.3	Nm
TQ_2	667.1	Nm
	Temperature readings:	**Units**
$T_{Oil\ M5}$	62.78	$°C$
$T_{Oil\ M12}$	64.08	$°C$
T_{Wall}	62.64	$°C$
T_{Amb}	28.32	$°C$
	Additional Information:	**Units**
$T_{Oil\ M5} - T_{Amb}$	34.47	$°C$
$Efficiency$	98.53	%
TQ_{Loss}	39.8	Nm

	S2: Reducer Gearbox	
	Actual Working Conditions:	**Units**
n_1	149.8	rpm
TQ_1	2708.4	Nm
TQ_2	685.3	Nm
	Temperature readings:	**Units**
$T_{Oil\ M5}$	68.46	$°C$
$T_{Oil\ M12}$	67.92	$°C$
T_{Wall}	66.04	$°C$
T_{Amb}	30.99	$°C$
	Additional Information:	**Units**
$T_{Oil\ M5} - T_{Amb}$	37.47	$°C$
$Efficiency$	98.81	%
TQ_{Loss}	32.7	Nm

Test Number:15	Date:25/03/2014	By: Raquel Camacho
Oil:	PAOR	
	Imposed Working Conditions:	**Units**
n_{in}	200	rpm
TQ_{in}	2800	Nm
$Test\ duration$	$240 + 90$	min

	S1: Multiplier Gearbox	
	Actual Working Conditions:	**Units**
n_1	200.1	rpm
TQ_1	2700.8	Nm
TQ_2	666.2	Nm
	Temperature readings:	**Units**
$T_{Oil\ M5}$	76.79	$°C$
$T_{Oil\ M12}$	76.43	$°C$
T_{Wall}	75.74	$°C$
T_{Amb}	31.20	$°C$
	Additional Information:	**Units**
$T_{Oil\ M5} - T_{Amb}$	45.59	$°C$
$Efficiency$	98.67	%
TQ_{Loss}	35.9	Nm

	S2: Reducer Gearbox	
	Actual Working Conditions:	**Units**
n_1	200.0	rpm
TQ_1	2708.4	Nm
TQ_2	685.7	Nm
	Temperature readings:	**Units**
$T_{Oil\ M5}$	79.99	$°C$
$T_{Oil\ M12}$	81.19	$°C$
T_{Wall}	79.87	$°C$
T_{Amb}	32.79	$°C$
	Additional Information:	**Units**
$T_{Oil\ M5} - T_{Amb}$	47.20	$°C$
$Efficiency$	98.74	%
TQ_{Loss}	34.5	Nm

Test Number:16	Date:26/03/2014	By: Raquel Camacho
Oil:	PAOR	
	Imposed Working Conditions:	**Units**
n_{in}	250	rpm
TQ_{in}	2800	Nm
$Test\ duration$	$240 + 90$	min

	S1: Multiplier Gearbox	
	Actual Working Conditions:	**Units**
n_1	250.4	rpm
TQ_1	2709.3	Nm
TQ_2	666.8	Nm
	Temperature readings:	**Units**
$T_{Oil\ M5}$	89.94	$°C$
$T_{Oil\ M12}$	87.81	$°C$
T_{Wall}	87.73	$°C$
T_{Amb}	31.93	$°C$
	Additional Information:	**Units**
$T_{Oil\ M5} - T_{Amb}$	58.01	$°C$
$Efficiency$	98.45	%
TQ_{Loss}	42.0	Nm

	S2: Reducer Gearbox	
	Actual Working Conditions:	**Units**
n_1	250.4	rpm
TQ_1	2709.6	Nm
TQ_2	686.1	Nm
	Temperature readings:	**Units**
$T_{Oil\ M5}$	90.93	$°C$
$T_{Oil\ M12}$	92.25	$°C$
T_{Wall}	91.46	$°C$
T_{Amb}	34.02	$°C$
	Additional Information:	**Units**
$T_{Oil\ M5} - T_{Amb}$	56.92	$°C$
$Efficiency$	98.73	%
TQ_{Loss}	34.8	Nm

B.2. PAOR Oil: 5 Test Grid

Test Number:17	Date:03/04/2014	By: Raquel Camacho
Oil:	PAOR	
	Imposed Working Conditions:	**Units**
n_{in}	100	rpm
TQ_{in}	2800	Nm
$Test\ duration$	$240 + 90$	min

	S1: Multiplier Gearbox	
	Actual Working Conditions:	**Units**
n_1	99.6	rpm
TQ_1	2709.0	Nm
TQ_2	668.1	Nm
	Temperature readings:	**Units**
$T_{Oil\ M5}$	51.48	$°C$
$T_{Oil\ M12}$	51.57	$°C$
T_{Wall}	50.07	$°C$
T_{Amb}	26.31	$°C$
	Additional Information:	**Units**
$T_{Oil\ M5} - T_{Amb}$	25.17	$°C$
$Efficiency$	98.65	$\%$
TQ_{Loss}	36.5	Nm

	S2: Reducer Gearbox	
	Actual Working Conditions:	**Units**
n_1	99.6	rpm
TQ_1	2709.0	Nm
TQ_2	685.8	Nm
	Temperature readings:	**Units**
$T_{Oil\ M5}$	55.32	$°C$
$T_{Oil\ M12}$	54.27	$°C$
T_{Wall}	52.45	$°C$
T_{Amb}	28.72	$°C$
	Additional Information:	**Units**
$T_{Oil\ M5} - T_{Amb}$	26.60	$°C$
$Efficiency$	98.75	$\%$
TQ_{Loss}	34.4	Nm

Test Number:18	Date:04/04/2014	By: Raquel Camacho
Oil:	PAOR	
	Imposed Working Conditions:	**Units**
n_{in}	150	rpm
TQ_{in}	2000	Nm
$Test\ duration$	$240 + 90$	min

	S1: Multiplier Gearbox	
	Actual Working Conditions:	**Units**
n_1	149.8	rpm
TQ_1	1935.0	Nm
TQ_2	475.6	Nm
	Temperature readings:	**Units**
$T_{Oil\ M5}$	57.29	$°C$
$T_{Oil\ M12}$	59.35	$°C$
T_{Wall}	57.71	$°C$
T_{Amb}	27.93	$°C$
	Additional Information:	**Units**
$T_{Oil\ M5} - T_{Amb}$	29.36	$°C$
$Efficiency$	98.32	%
TQ_{Loss}	32.6	Nm

	S2: Reducer Gearbox	
	Actual Working Conditions:	**Units**
n_1	149.8	rpm
TQ_1	1935.3	Nm
TQ_2	491.3	Nm
	Temperature readings:	**Units**
$T_{Oil\ M5}$	62.86	$°C$
$T_{Oil\ M12}$	62.23	$°C$
T_{Wall}	60.58	$°C$
T_{Amb}	30.72	$°C$
	Additional Information:	**Units**
$T_{Oil\ M5} - T_{Amb}$	32.14	$°C$
$Efficiency$	98.47	%
TQ_{Loss}	30.0	Nm

Test Number:19	Date:07/04/2014	By: Raquel Camacho
Oil:	PAOR	
	Imposed Working Conditions:	**Units**
n_{in}	150	rpm
TQ_{in}	2400	Nm
$Test\ duration$	$240 + 90$	min

	S1: Multiplier Gearbox	
	Actual Working Conditions:	**Units**
n_1	149.8	rpm
TQ_1	2321.7	Nm
TQ_2	574.8	Nm
	Temperature readings:	**Units**
$T_{Oil\ M5}$	58.97	$°C$
$T_{Oil\ M12}$	60.47	$°C$
T_{Wall}	58.98	$°C$
T_{Amb}	28.47	$°C$
	Additional Information:	**Units**
$T_{Oil\ M5} - T_{Amb}$	30.50	$°C$
$Efficiency$	99.03	%
TQ_{Loss}	22.6	Nm

	S2: Reducer Gearbox	
	Actual Working Conditions:	**Units**
n_1	149.8	rpm
TQ_1	2321.7	Nm
TQ_2	590.6	Nm
	Temperature readings:	**Units**
$T_{Oil\ M5}$	65.08	$°C$
$T_{Oil\ M12}$	64.10	$°C$
T_{Wall}	62.41	$°C$
T_{Amb}	29.50	$°C$
	Additional Information:	**Units**
$T_{Oil\ M5} - T_{Amb}$	35.59	$°C$
$Efficiency$	98.28	%
TQ_{Loss}	40.7	Nm

Test Number:20	Date:08/04/2014	By: Raquel Camacho
Oil:	PAOR	
	Imposed Working Conditions:	**Units**
n_{in}	150	rpm
TQ_{in}	2800	Nm
$Test\ duration$	$240 + 90$	min

	S1: Multiplier Gearbox	
	Actual Working Conditions:	**Units**
n_1	149.8	rpm
TQ_1	2709.4	Nm
TQ_2	671.2	Nm
	Temperature readings:	**Units**
$T_{Oil\ M5}$	62.43	$°C$
$T_{Oil\ M12}$	63.35	$°C$
T_{Wall}	61.85	$°C$
T_{Amb}	30.17	$°C$
	Additional Information:	**Units**
$T_{Oil\ M5} - T_{Amb}$	32.26	$°C$
$Efficiency$	99.09	%
TQ_{Loss}	24.8	Nm

	S2: Reducer Gearbox	
	Actual Working Conditions:	**Units**
n_1	149.8	rpm
TQ_1	2709.1	Nm
TQ_2	687.7	Nm
	Temperature readings:	**Units**
$T_{Oil\ M5}$	68.84	$°C$
$T_{Oil\ M12}$	67.44	$°C$
T_{Wall}	65.64	$°C$
T_{Amb}	31.47	$°C$
	Additional Information:	**Units**
$T_{Oil\ M5} - T_{Amb}$	37.37	$°C$
$Efficiency$	98.48	%
TQ_{Loss}	41.9	Nm

Test Number:21	Date:09/04/2014	By: Raquel Camacho
Oil:	PAOR	
	Imposed Working Conditions:	**Units**
n_{in}	200	rpm
TQ_{in}	2800	Nm
$Test\ duration$	$240 + 90$	min

	S1: Multiplier Gearbox	
	Actual Working Conditions:	**Units**
n_1	200.0	rpm
TQ_1	2707.9	Nm
TQ_2	671.0	Nm
	Temperature readings:	**Units**
$T_{Oil\ M5}$	74.06	$°C$
$T_{Oil\ M12}$	74.36	$°C$
T_{Wall}	72.52	$°C$
T_{Amb}	33.28	$°C$
	Additional Information:	**Units**
$T_{Oil\ M5} - T_{Amb}$	40.78	$°C$
$Efficiency$	99.11	%
TQ_{Loss}	24.0	Nm

	S2: Reducer Gearbox	
	Actual Working Conditions:	**Units**
n_1	200.0	rpm
TQ_1	2709.7	Nm
TQ_2	686.8	Nm
	Temperature readings:	**Units**
$T_{Oil\ M5}$	78.03	$°C$
$T_{Oil\ M12}$	76.87	$°C$
T_{Wall}	75.46	$°C$
T_{Amb}	34.79	$°C$
	Additional Information:	**Units**
$T_{Oil\ M5} - T_{Amb}$	43.24	$°C$
$Efficiency$	98.64	%
TQ_{Loss}	37.3	Nm

B.3. PAOR: comparison between test grids

Test & Direction	Grid	n_1	TQ_1	TQ_2	$T_{Oil\ M5}$	T_{Amb}	ΔT
100rpm/2800Nm (S1)	16	99.7	2708.6	667.6	53.84	28.40	25.44
	5	99.6	2709.0	668.1	51.48	26.31	25.17
100rpm/2800Nm (S2)	16	99.7	2708.7	685.6	56.24	29.92	26.32
	5	99.6	2709.0	685.8	55.32	28.72	26.60
150rpm/2000Nm (S1)	16	149.9	1936.4	475.7	61.00	31.07	29.93
	5	149.8	1935.0	475.6	57.29	27.93	29.36
150rpm/2000Nm (S2)	16	150.6	1935.8	490.7	64.04	34.49	29.55
	5	149.8	1935.3	491.3	62.86	30.72	32.14
150rpm/2400Nm (S1)	16	149.9	2322.3	571.7	63.29	31.13	35.7
	5	149.8	2321.7	574.8	58.97	28.47	30.50
150rpm/2400Nm (S2)	16	149.8	2321.7	588.6	68.60	34.80	33.80
	5	149.8	2321.7	590.6	65.08	29.50	35.59
150rpm/2800Nm (S1)	16	149.8	2708.3	667.1	62.78	28.32	34.47
	5	149.8	2709.4	671.2	62.43	30.17	32.26
150rpm/2800Nm (S2)	16	149.8	2708.4	685.3	68.46	30.99	37.47
	5	149.8	2709.1	687.7	68.84	31.47	41.9
200rpm/2800Nm (S1)	16	200.1	2700.8	666.2	76.79	31.20	45.59
	5	200.0	2707.9	671.0	74.06	33.28	40.78
200rpm/2800Nm (S2)	16	200.0	2708.4	685.7	79.99	32.79	47.20
	5	200.0	2709.7	686.8	78.03	34.79	43.24

B.4. MINR Oil: 5 Test Grid

Test Number:22	Date:10/04/2014	By: Raquel Camacho
Oil:	MINR	
	Imposed Working Conditions:	**Units**
n_{in}	100	rpm
TQ_{in}	2800	Nm
$Test\ duration$	$240 + 90$	min
	S1: Multiplier Gearbox	
	Actual Working Conditions:	**Units**
n_1	99.6	rpm
TQ_1	2709.4	Nm
TQ_2	668.2	Nm
	Temperature readings:	**Units**
$T_{Oil\ M5}$	57.64	$°C$
$T_{Oil\ M12}$	56.70	$°C$
T_{Wall}	54.83	$°C$
T_{Amb}	25.80	$°C$
	Additional Information:	**Units**
$T_{Oil\ M5} - T_{Amb}$	31.83	$°C$
$Efficiency$	98.65	%
TQ_{Loss}	36.7	Nm
	S2: Reducer Gearbox	
	Actual Working Conditions:	**Units**
n_1	99.6	rpm
TQ_1	2708.9	Nm
TQ_2	688.0	Nm
	Temperature readings:	**Units**
$T_{Oil\ M5}$	60.26	$°C$
$T_{Oil\ M12}$	58.11	$°C$
T_{Wall}	56.12	$°C$
T_{Amb}	26.78	$°C$
	Additional Information:	**Units**
$T_{Oil\ M5} - T_{Amb}$	33.48	$°C$
$Efficiency$	98.43	%
TQ_{Loss}	43.3	Nm

Test Number:23	Date:14/04/2014	By: Raquel Camacho
Oil:	MINR	
	Imposed Working Conditions:	**Units**
n_{in}	150	rpm
TQ_{in}	2000	Nm
$Test\ duration$	$240 + 90$	min

	S1: Multiplier Gearbox	
	Actual Working Conditions:	**Units**
n_1	150.0	rpm
TQ_1	1933.0	Nm
TQ_2	478.3	Nm
	Temperature readings:	**Units**
$T_{Oil\ M5}$	60.72	$°C$
$T_{Oil\ M12}$	62.25	$°C$
T_{Wall}	60.10	$°C$
T_{Amb}	30.03	$°C$
	Additional Information:	**Units**
$T_{Oil\ M5} - T_{Amb}$	30.69	$°C$
$Efficiency$	98.98	%
TQ_{Loss}	19.8	Nm

	S2: Reducer Gearbox	
	Actual Working Conditions:	**Units**
n_1	150.0	rpm
TQ_1	1937.3	Nm
TQ_2	494.1	Nm
	Temperature readings:	**Units**
$T_{Oil\ M5}$	68.50	$°C$
$T_{Oil\ M12}$	66.67	$°C$
T_{Wall}	64.85	$°C$
T_{Amb}	32.24	$°C$
	Additional Information:	**Units**
$T_{Oil\ M5} - T_{Amb}$	36.26	$°C$
$Efficiency$	98.02	%
TQ_{Loss}	39.0	Nm

Test Number:24	Date:15/04/2014	By: Raquel Camacho
Oil:	MINR	
	Imposed Working Conditions:	**Units**
n_{in}	150	rpm
TQ_{in}	2400	Nm
$Test\ duration$	$240 + 90$	min
	S1: Multiplier Gearbox	
	Actual Working Conditions:	**Units**
n_1	150.0	rpm
TQ_1	2320.9	Nm
TQ_2	574.1	Nm
	Temperature readings:	**Units**
$T_{Oil\ M5}$	63.67	$°C$
$T_{Oil\ M12}$	64.33	$°C$
T_{Wall}	62.32	$°C$
T_{Amb}	29.60	$°C$
	Additional Information:	**Units**
$T_{Oil\ M5} - T_{Amb}$	34.07	$°C$
$Efficiency$	98.94	%
TQ_{Loss}	24.6	Nm
	S2: Reducer Gearbox	
	Actual Working Conditions:	**Units**
n_1	149.9	rpm
TQ_1	2321.5	Nm
TQ_2	590.3	Nm
	Temperature readings:	**Units**
$T_{Oil\ M5}$	70.66	$°C$
$T_{Oil\ M12}$	68.18	$°C$
T_{Wall}	66.42	$°C$
T_{Amb}	31.01	$°C$
	Additional Information:	**Units**
$T_{Oil\ M5} - T_{Amb}$	39.65	$°C$
$Efficiency$	98.31	%
TQ_{Loss}	39.8	Nm

Test Number:25	Date:16/04/2014	By: Raquel Camacho
Oil:	MINR	
	Imposed Working Conditions:	**Units**
n_{in}	150	rpm
TQ_{in}	2800	Nm
$Test\ duration$	$240 + 90$	min

	S1: Multiplier Gearbox	
	Actual Working Conditions:	**Units**
n_1	150.0	rpm
TQ_1	2705.5	Nm
TQ_2	668.6	Nm
	Temperature readings:	**Units**
$T_{Oil\ M5}$	66.72	$°C$
$T_{Oil\ M12}$	66.86	$°C$
T_{Wall}	64.62	$°C$
T_{Amb}	29.04	$°C$
	Additional Information:	**Units**
$T_{Oil\ M5} - T_{Amb}$	37.68	$°C$
$Efficiency$	98.85	$\%$
TQ_{Loss}	31.1	Nm

	S2: Reducer Gearbox	
	Actual Working Conditions:	**Units**
n_1	149.9	rpm
TQ_1	2710.5	Nm
TQ_2	687.6	Nm
	Temperature readings:	**Units**
$T_{Oil\ M5}$	73.36	$°C$
$T_{Oil\ M12}$	70.42	$°C$
T_{Wall}	68.51	$°C$
T_{Amb}	30.64	$°C$
	Additional Information:	**Units**
$T_{Oil\ M5} - T_{Amb}$	42.73	$°C$
$Efficiency$	98.56	$\%$
TQ_{Loss}	39.7	Nm

Test Number:26	Date:17/04/2014	By: Raquel Camacho
Oil:	MINR	
	Imposed Working Conditions:	**Units**
n_{in}	200	rpm
TQ_{in}	2800	Nm
$Test\ duration$	$240 + 90$	min

	S1: Multiplier Gearbox	
	Actual Working Conditions:	**Units**
n_1	200.1	rpm
TQ_1	2708.0	Nm
TQ_2	670.9	Nm
	Temperature readings:	**Units**
$T_{Oil\ M5}$	80.30	$°C$
$T_{Oil\ M12}$	77.43	$°C$
T_{Wall}	76.16	$°C$
T_{Amb}	33.77	$°C$
	Additional Information:	**Units**
$T_{Oil\ M5} - T_{Amb}$	46.53	$°C$
$Efficiency$	99.09	%
TQ_{Loss}	24.5	Nm

	S2: Reducer Gearbox	
	Actual Working Conditions:	**Units**
n_1	200.0	rpm
TQ_1	2703.8	Nm
TQ_2	685.6	Nm
	Temperature readings:	**Units**
$T_{Oil\ M5}$	84.50	$°C$
$T_{Oil\ M12}$	80.49	$°C$
T_{Wall}	79.16	$°C$
T_{Amb}	35.38	$°C$
	Additional Information:	**Units**
$T_{Oil\ M5} - T_{Amb}$	49.11	$°C$
$Efficiency$	98.59	%
TQ_{Loss}	38.8	Nm

B.5. MINE Oil: 5 Test Grid

Test Number:27	Date:21/04/2014	By: Raquel Camacho
Oil:	MINE	
	Imposed Working Conditions:	**Units**
n_{in}	100	rpm
TQ_{in}	2800	Nm
$Test\ duration$	$240 + 90$	min

	S1: Multiplier Gearbox	
	Actual Working Conditions:	**Units**
n_1	99.6	rpm
TQ_1	2708.7	Nm
TQ_2	669.3	Nm
	Temperature readings:	**Units**
$T_{Oil\ M5}$	51.49	$°C$
$T_{Oil\ M12}$	52.88	$°C$
T_{Wall}	50.76	$°C$
T_{Amb}	24.79	$°C$
	Additional Information:	**Units**
$T_{Oil\ M5} - T_{Amb}$	26.70	$°C$
$Efficiency$	98.83	%
TQ_{Loss}	31.7	Nm

	S2: Reducer Gearbox	
	Actual Working Conditions:	**Units**
n_1	99.7	rpm
TQ_1	2708.3	Nm
TQ_2	687.7	Nm
	Temperature readings:	**Units**
$T_{Oil\ M5}$	55.13	$°C$
$T_{Oil\ M12}$	54.65	$°C$
T_{Wall}	52.62	$°C$
T_{Amb}	25.70	$°C$
	Additional Information:	**Units**
$T_{Oil\ M5} - T_{Amb}$	29.43	$°C$
$Efficiency$	98.46	%
TQ_{Loss}	42.4	Nm

Test Number:28	Date:22/04/2014	By: Raquel Camacho
Oil:	MINE	
	Imposed Working Conditions:	**Units**
n_{in}	150	rpm
TQ_{in}	2000	Nm
$Test\ duration$	$240 + 90$	min

	S1: Multiplier Gearbox	
	Actual Working Conditions:	**Units**
n_1	149.9	rpm
TQ_1	1935.3	Nm
TQ_2	477.2	Nm
	Temperature readings:	**Units**
$T_{Oil\ M5}$	56.82	$°C$
$T_{Oil\ M12}$	60.01	$°C$
T_{Wall}	57.77	$°C$
T_{Amb}	26.66	$°C$
	Additional Information:	**Units**
$T_{Oil\ M5} - T_{Amb}$	30.17	$°C$
$Efficiency$	98.64	%
TQ_{Loss}	26.3	Nm

	S2: Reducer Gearbox	
	Actual Working Conditions:	**Units**
n_1	149.8	rpm
TQ_1	1935.4	Nm
TQ_2	493.0	Nm
	Temperature readings:	**Units**
$T_{Oil\ M5}$	62.85	$°C$
$T_{Oil\ M12}$	62.99	$°C$
T_{Wall}	61.21	$°C$
T_{Amb}	27.99	$°C$
	Additional Information:	**Units**
$T_{Oil\ M5} - T_{Amb}$	34.87	$°C$
$Efficiency$	98.14	%
TQ_{Loss}	36.6	Nm

Test Number:29	Date:23/04/2014	By: Raquel Camacho
Oil:	MINE	
	Imposed Working Conditions:	**Units**
n_{in}	150	rpm
TQ_{in}	2400	Nm
$Test\ duration$	$240 + 90$	min

	S1: Multiplier Gearbox	
	Actual Working Conditions:	**Units**
n_1	149.9	rpm
TQ_1	2322.4	Nm
TQ_2	573.1	Nm
	Temperature readings:	**Units**
$T_{Oil\ M5}$	58.48	$°C$
$T_{Oil\ M12}$	61.30	$°C$
T_{Wall}	59.06	$°C$
T_{Amb}	25.98	$°C$
	Additional Information:	**Units**
$T_{Oil\ M5} - T_{Amb}$	32.50	$°C$
$Efficiency$	98.70	%
TQ_{Loss}	30.1	Nm

	S2: Reducer Gearbox	
	Actual Working Conditions:	**Units**
n_1	149.8	rpm
TQ_1	2321.7	Nm
TQ_2	589.7	Nm
	Temperature readings:	**Units**
$T_{Oil\ M5}$	64.72	$°C$
$T_{Oil\ M12}$	64.57	$°C$
T_{Wall}	62.77	$°C$
T_{Amb}	27.83	$°C$
	Additional Information:	**Units**
$T_{Oil\ M5} - T_{Amb}$	36.89	$°C$
$Efficiency$	98.43	%
TQ_{Loss}	37.1	Nm

Test Number:30	Date:24/04/2014	By: Raquel Camacho
Oil:	MINE	
	Imposed Working Conditions:	**Units**
n_{in}	150	rpm
TQ_{in}	2800	Nm
$Test\ duration$	$240 + 90$	min

	S1: Multiplier Gearbox	
	Actual Working Conditions:	**Units**
n_1	149.8	rpm
TQ_1	2709.1	Nm
TQ_2	669.5	Nm
	Temperature readings:	**Units**
$T_{Oil\ M5}$	58.81	$°C$
$T_{Oil\ M12}$	61.16	$°C$
T_{Wall}	59.01	$°C$
T_{Amb}	23.84	$°C$
	Additional Information:	**Units**
$T_{Oil\ M5} - T_{Amb}$	34.97	$°C$
$Efficiency$	98.85	%
TQ_{Loss}	31.2	Nm

	S2: Reducer Gearbox	
	Actual Working Conditions:	**Units**
n_1	153.6	rpm
TQ_1	2709.7	Nm
TQ_2	686.7	Nm
	Temperature readings:	**Units**
$T_{Oil\ M5}$	66.34	$°C$
$T_{Oil\ M12}$	65.87	$°C$
T_{Wall}	64.05	$°C$
T_{Amb}	26.15	$°C$
	Additional Information:	**Units**
$T_{Oil\ M5} - T_{Amb}$	40.19	$°C$
$Efficiency$	98.65	%
TQ_{Loss}	37.1	Nm

Test Number:31	Date:28/04/2014	By: Raquel Camacho
Oil:	MINE	
	Imposed Working Conditions:	**Units**
n_{in}	200	rpm
TQ_{in}	2800	Nm
$Test\ duration$	$240 + 90$	min

	S1: Multiplier Gearbox	
	Actual Working Conditions:	**Units**
n_1	202.0	rpm
TQ_1	2705.2	Nm
TQ_2	668.9	Nm
	Temperature readings:	**Units**
$T_{Oil\ M5}$	69.84	$°C$
$T_{Oil\ M12}$	71.50	$°C$
T_{Wall}	69.33	$°C$
T_{Amb}	26.31	$°C$
	Additional Information:	**Units**
$T_{Oil\ M5} - T_{Amb}$	43.52	$°C$
$Efficiency$	98.91	%
TQ_{Loss}	29.5	Nm

	S2: Reducer Gearbox	
	Actual Working Conditions:	**Units**
n_1	199.9	rpm
TQ_1	2713.2	Nm
TQ_2	688.3	Nm
	Temperature readings:	**Units**
$T_{Oil\ M5}$	73.72	$°C$
$T_{Oil\ M12}$	74.65	$°C$
T_{Wall}	73.12	$°C$
T_{Amb}	28.63	$°C$
	Additional Information:	**Units**
$T_{Oil\ M5} - T_{Amb}$	45.09	$°C$
$Efficiency$	98.55	%
TQ_{Loss}	40.0	Nm

B.6. PAGD Oil: 5 Test Grid

Test Number:32	Date:29/04/2014	By: Raquel Camacho
Oil:	MINE	
	Imposed Working Conditions:	**Units**
n_{in}	100	rpm
TQ_{in}	2800	Nm
$Test\ duration$	$240 + 90$	min

	S1: Multiplier Gearbox	
	Actual Working Conditions:	**Units**
n_1	99.6	rpm
TQ_1	2709.5	Nm
TQ_2	668.3	Nm
	Temperature readings:	**Units**
$T_{Oil\ M5}$	54.22	$°C$
$T_{Oil\ M12}$	55.32	$°C$
T_{Wall}	53.21	$°C$
T_{Amb}	26.11	$°C$
	Additional Information:	**Units**
$T_{Oil\ M5} - T_{Amb}$	28.11	$°C$
$Efficiency$	98.66	%
TQ_{Loss}	36.3	Nm

	S2: Reducer Gearbox	
	Actual Working Conditions:	**Units**
n_1	99.6	rpm
TQ_1	2709.1	Nm
TQ_2	686.9	Nm
	Temperature readings:	**Units**
$T_{Oil\ M5}$	57.05	$°C$
$T_{Oil\ M12}$	56.67	$°C$
T_{Wall}	54.67	$°C$
T_{Amb}	27.50	$°C$
	Additional Information:	**Units**
$T_{Oil\ M5} - T_{Amb}$	29.55	$°C$
$Efficiency$	98.60	%
TQ_{Loss}	38.5	Nm

Test Number:33	Date:30/04/2014	By: Raquel Camacho
Oil:	MINE	
	Imposed Working Conditions:	**Units**
n_{in}	150	rpm
TQ_{in}	2000	Nm
$Test\ duration$	$240 + 90$	min

	S1: Multiplier Gearbox	
	Actual Working Conditions:	**Units**
n_1	149.8	rpm
TQ_1	1934.9	Nm
TQ_2	476.4	Nm
	Temperature readings:	**Units**
$T_{Oil\ M5}$	60.62	$°C$
$T_{Oil\ M12}$	63.59	$°C$
T_{Wall}	61.39	$°C$
T_{Amb}	27.23	$°C$
	Additional Information:	**Units**
$T_{Oil\ M5} - T_{Amb}$	33.39	$°C$
$Efficiency$	98.48	%
TQ_{Loss}	29.3	Nm

	S2: Reducer Gearbox	
	Actual Working Conditions:	**Units**
n_1	149.8	rpm
TQ_1	1935.6	Nm
TQ_2	493.8	Nm
	Temperature readings:	**Units**
$T_{Oil\ M5}$	65.54	$°C$
$T_{Oil\ M12}$	65.67	$°C$
T_{Wall}	63.83	$°C$
T_{Amb}	29.24	$°C$
	Additional Information:	**Units**
$T_{Oil\ M5} - T_{Amb}$	36.29	$°C$
$Efficiency$	98.01	%
TQ_{Loss}	39.4	Nm

Test Number:34	Date:02/05/2014	By: Raquel Camacho
Oil:	MINE	
	Imposed Working Conditions:	**Units**
n_{in}	150	rpm
TQ_{in}	2400	Nm
$Test\ duration$	$240 + 90$	min

	S1: Multiplier Gearbox	
	Actual Working Conditions:	**Units**
n_1	149.9	rpm
TQ_1	2322.2	Nm
TQ_2	573.4	Nm
	Temperature readings:	**Units**
$T_{Oil\ M5}$	63.42	$°C$
$T_{Oil\ M12}$	66.14	$°C$
T_{Wall}	63.70	$°C$
T_{Amb}	29.97	$°C$
	Additional Information:	**Units**
$T_{Oil\ M5} - T_{Amb}$	33.45	$°C$
$Efficiency$	98.77	%
TQ_{Loss}	28.6	Nm

	S2: Reducer Gearbox	
	Actual Working Conditions:	**Units**
n_1	150.0	rpm
TQ_1	2320.1	Nm
TQ_2	589.7	Nm
	Temperature readings:	**Units**
$T_{Oil\ M5}$	68.19	$°C$
$T_{Oil\ M12}$	67.98	$°C$
T_{Wall}	66.05	$°C$
T_{Amb}	31.77	$°C$
	Additional Information:	**Units**
$T_{Oil\ M5} - T_{Amb}$	36.41	$°C$
$Efficiency$	98.35	%
TQ_{Loss}	38.9	Nm

Test Number:35	Date:08/05/2014	By: Raquel Camacho
Oil:	MINE	
	Imposed Working Conditions:	**Units**
n_{in}	150	rpm
TQ_{in}	2800	Nm
$Test\ duration$	$240 + 90$	min

	S1: Multiplier Gearbox	
	Actual Working Conditions:	**Units**
n_1	152.8	rpm
TQ_1	2709.2	Nm
TQ_2	670.6	Nm
	Temperature readings:	**Units**
$T_{Oil\ M5}$	63.15	$°C$
$T_{Oil\ M12}$	65.92	$°C$
T_{Wall}	63.73	$°C$
T_{Amb}	27.79	$°C$
	Additional Information:	**Units**
$T_{Oil\ M5} - T_{Amb}$	35.35	$°C$
$Efficiency$	99.02	%
TQ_{Loss}	26.6	Nm

	S2: Reducer Gearbox	
	Actual Working Conditions:	**Units**
n_1	152.9	rpm
TQ_1	2709.3	Nm
TQ_2	687.6	Nm
	Temperature readings:	**Units**
$T_{Oil\ M5}$	70.01	$°C$
$T_{Oil\ M12}$	69.59	$°C$
T_{Wall}	67.31	$°C$
T_{Amb}	29.65	$°C$
	Additional Information:	**Units**
$T_{Oil\ M5} - T_{Amb}$	40.36	$°C$
$Efficiency$	98.50	%
TQ_{Loss}	41.2	Nm

Test Number:36	Date:12/05/2014	By: Raquel Camacho
Oil:	MINE	
	Imposed Working Conditions:	**Units**
n_{in}	200	rpm
TQ_{in}	2800	Nm
$Test\ duration$	$240 + 90$	min

	S1: Multiplier Gearbox	
	Actual Working Conditions:	**Units**
n_1	200.0	rpm
TQ_1	2708.2	Nm
TQ_2	671.1	Nm
	Temperature readings:	**Units**
$T_{Oil\ M5}$	74.78	$°C$
$T_{Oil\ M12}$	76.59	$°C$
T_{Wall}	74.16	$°C$
T_{Amb}	30.30	$°C$
	Additional Information:	**Units**
$T_{Oil\ M5} - T_{Amb}$	44.48	$°C$
$Efficiency$	99.11	%
TQ_{Loss}	24.0	Nm

	S2: Reducer Gearbox	
	Actual Working Conditions:	**Units**
n_1	200.0	rpm
TQ_1	2710.2	Nm
TQ_2	688.8	Nm
	Temperature readings:	**Units**
$T_{Oil\ M5}$	80.33	$°C$
$T_{Oil\ M12}$	79.21	$°C$
T_{Wall}	77.46	$°C$
T_{Amb}	30.92	$°C$
	Additional Information:	**Units**
$T_{Oil\ M5} - T_{Amb}$	49.41	$°C$
$Efficiency$	98.37	%
TQ_{Loss}	44.9	Nm

C. Lubrican Analysis Report

driving innovation

since 1986

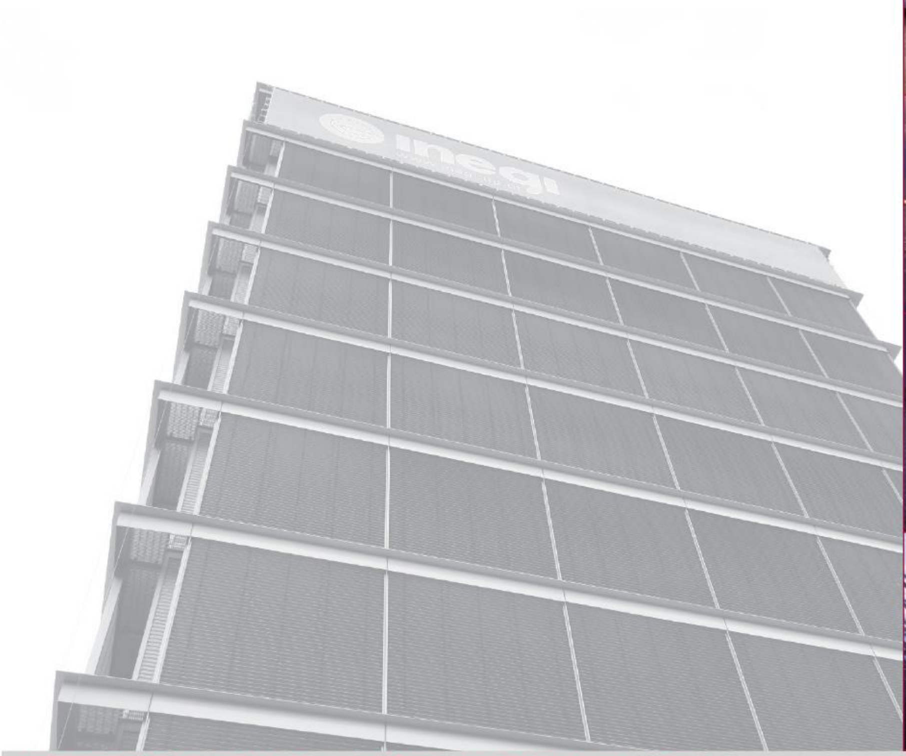

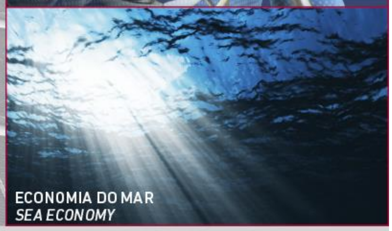

INSTITUTO DE ENGENHARIA MECÂNICA E GESTÃO INDUSTRIAL
INSTITUTE OF MECHANICAL ENGINEERING AND INDUSTRIAL MANAGEMENT

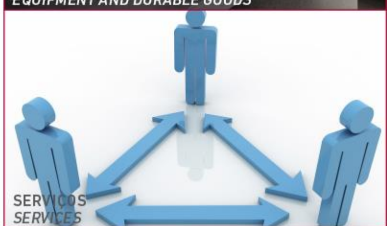

ANÁLISE DE LUBRIFICANTES

ANÁLISE DE FERROGRAFIA

CETRIB
Unidade de Tribologia, Vibrações e Manutenção Industrial

U.PORTO

0 Controlo Documental

0.1 Identificação do Documento

Análise Nº	36 - 43 / 14
Tipo de Análise	Análise de Ferrografia
Nome Ficheiro Documento	Ensaios_Banco

0.2 Identificação do Equipamento

Equipamento	Banco de Ensaios
Componente	Caixa de Engrenagens
Lubrificante	Óleos MinE; MinR; PAO; PAG

0.3 Autor(es)

Nome	Iniciais
Beatriz Graça	BMG
Ramiro Martins	RCM

0.4 Cliente

Nome	INEGI
Morada	Porto
Telefone / Fax	

0.5 Lista de distribuição

Nome	Iniciais	Entidade

OBJECTIVO

Análise de nove amostras de óleo lubrificante, resultantes de ensaios no Banco de Engrenagens, para avaliação do desgaste presente.

As amostras analisadas foram as seguintes:

Amostra Nº	Análises efectuadas	
	Ferrometria	Ferrografia Analítica
MinE 00	X	-
MinE 5	X	X
MinR 5	X	X
PAOR 100	X	-
PAOR 150	X	-
PAOR 200	X	-
PAOR 250	X	-
PAOR 2800	X	X
PAG	X	X

RESULTADOS DAS ANÁLISES

Nas páginas seguintes são apresentados os resultados referentes às análises de Ferrometria (DR III) e Ferrografia Analítica (FM III).

CLIENTE: ***INEGI***
MORADA: Porto
DATA: 09/06/14

ENSAIO: Banco de Ensaios
Ref. Óleos: MinE; MinR; PAOR; PAG

IDENTIFICAÇÃO									
Amostra nº:	**MinE 00**	**MinE 5**	**MinR 5**	**PAOR 100**	**PAOR 150**	**PAOR 200**	**PAOR 250**	**PAOR 2800**	**PAG**
Data amostra:	**mai-14**	**mai-14**	**mai-14**	**mai-14**	**mai-14**	**mai-14**	**mai-14**	**mai-14**	**mai-14**
Análise nº:	**44/14**	**45/14**	**46/14**	**47/14**	**48/14**	**49/14**	**50/14**	**51/14**	**51/14**
Ciclos/Máquina:	-	-	-	-	-	-	-	-	-
Ciclos/Óleo:	-	-	-	-	-	-	-	-	-
FERROMETRIA									
d:	**1,0**	**1,0**	**0,1**	**0,1**	**0,1**	**0,1**	**0,1**	**0,1**	**1,0**
DL:	**5,3**	**88,9**	**45,8**	**29,3**	**27,8**	**26,4**	**22,8**	**25,9**	**17,0**
DS:	**2,2**	**27,0**	**13,4**	**2,8**	**3,8**	**3,3**	**3,2**	**3,4**	**9,2**
CPUC:	**7,5**	**115,9**	**592,0**	**321,0**	**316,0**	**297,0**	**260,0**	**293,0**	**26,2**
ISUC:	**2,3E+01**	**7,2E+03**	**1,9E+05**	**8,5E+04**	**7,6E+04**	**6,9E+04**	**5,1E+04**	**6,6E+04**	**2,0E+02**
FERROGRAFIA:									
Desgaste normal									
Desgaste severo									
Desgaste abrasão									
Desgaste combinado									
Desgaste fadiga									
Esferas Metálicas									
Ligas não ferrosas									
Óxidos de ferro									
Minerais/Orgânicos									
OILVIEW:									
Índice OilLife:									
Índice Oxidação:									
Índice Contaminação:									
Índice Ferromagnético:									
Grandes Contaminantes:									
Constante Dieléctrica:									
FILTRAGEM									
(Nº Partículas/10 ml)									
5 - 15 µm									
15 - 25 µm									
25 - 50 µm									
50 - 100 µm									
> 100 µm									
VISCOSIDADE									
(cSt a 40° C):									
ACIDEZ (TAN)									
(mg KOH)									
P. INFLAMAÇÃO									
(° C)									
DIAGNÓSTICO:									

LEGENDA

DL - Índice de partículas grandes		Não existe
DS - Índice de partículas pequenas	**f**	Fraco
CPUC - Concentração de partículas de de	**M**	Médio
ISUC - Índice de severidade de desgaste	**F**	Forte

CLIENTE: ***INEGI***	ENSAIO: Banco de Ensaios
MORADA: Porto	**Ref. Óleos: MinE5 d = 1**
DATA: 09/06/14	

Fotografia 1

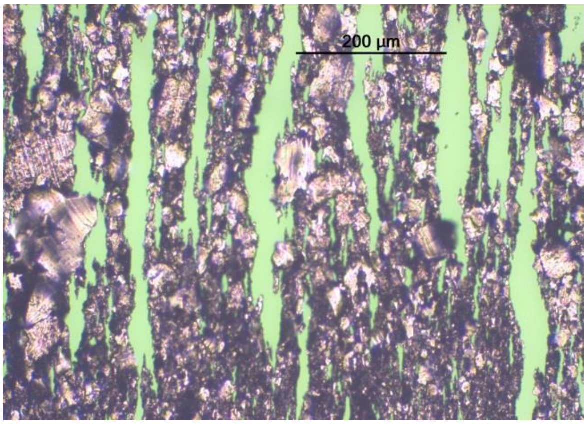

Ampliação: x 200 Diluíção: 1
Localização: Núcleo Luz: Branca / Verde

Observações: Presença significativa de partículas ferrosas de desgaste de grandes e pequenas dimensões .

Fotografia 2

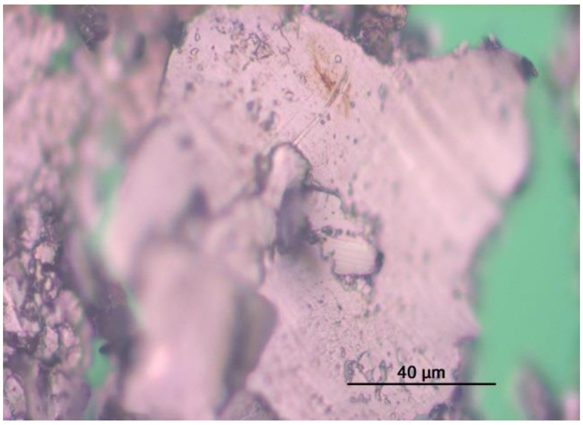

Ampliação: x 1000 Diluíção: 1
Localização: Núcleo Luz: Branca / Verde

Observações: Ampliação da Fotografia 1. Partículas ferrosa de grandes dimensões, típicas de desgaste severo de fadiga.

Fotografia 3

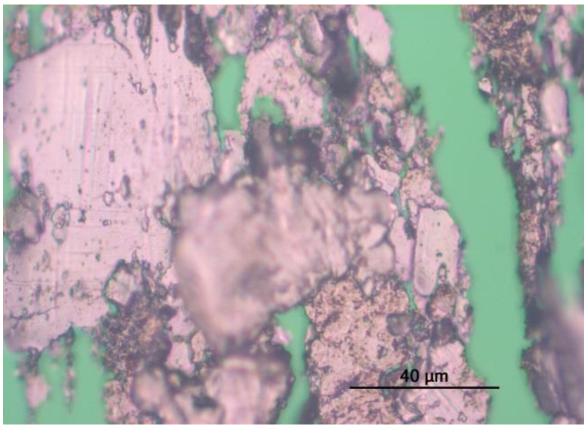

Ampliação: x 1000 Diluíção: 1
Localização: Núcleo Luz: Branca / Verde

Observações: Ampliação da Fotografia 1. Partículas ferrosas de grandes dimensões, típicas de desgaste de fadiga.

CLIENTE: ***INEGI***	ENSAIO: Banco de Ensaios
MORADA: Porto	**Ref. Óleos: MinR 5 d = 0.1**
DATA: 09/06/14	

Fotografia 4

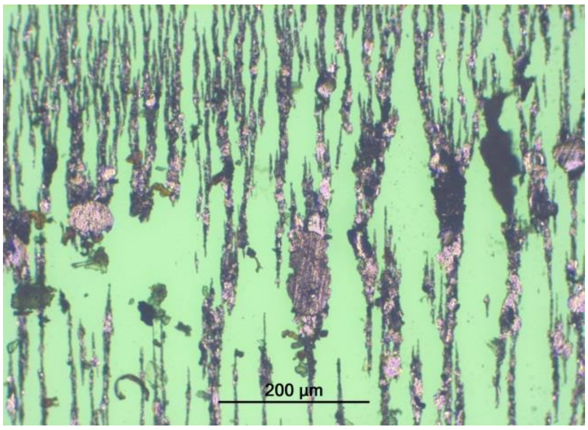

Ampliação: x 200 Diluição: 0,1
Localização: Nucleo Luz: Branca / Verde

Observações: Presença de algumas partículas ferrosas de desgaste e de oxidos térmicos.

Fotografia 5

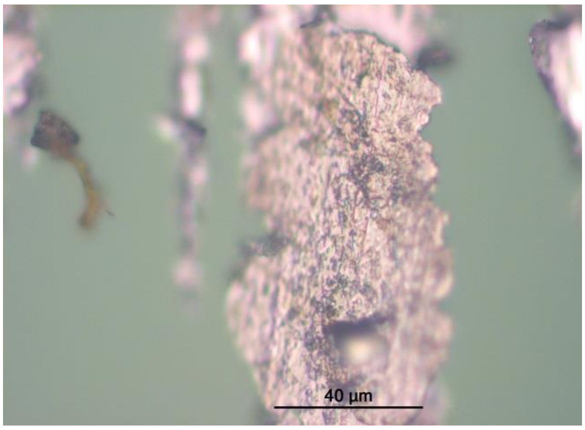

Ampliação: x 1000 Diluíção: 0,1
Localização: Núcleo Luz: Branca / Verde

Observações: Ampliação da Fotografia 4. Partícula ferrosa de desgaste de grande dimensão e ligeiramente oxidada .

Fotografia 6

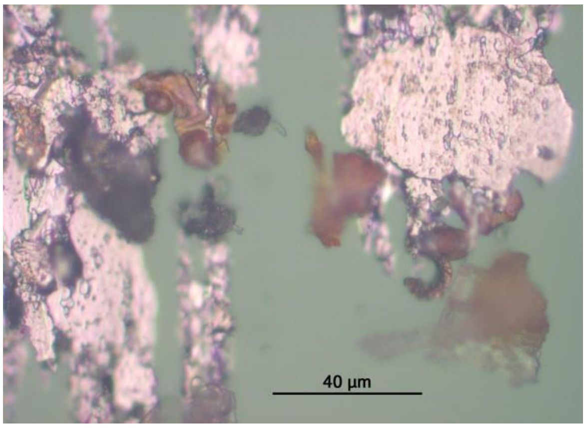

Ampliação: x 1000 Diluição: 0,1
Localização: Nucleo Luz: Branca / Verde

Observações: Ampliação da Fotografia 4. Partículas ferrosas de desgaste de grande dimensão e algumas partículas de "vernizes".

Fotografia 7

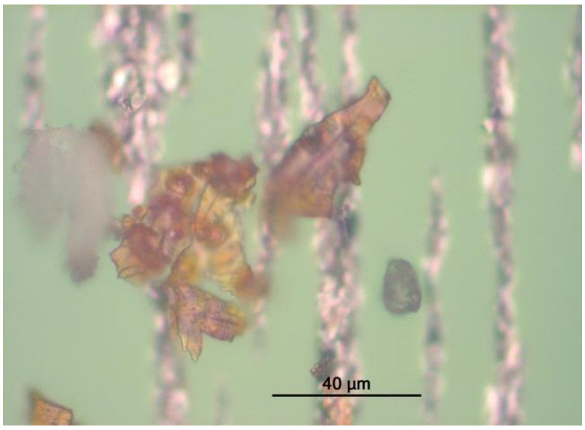

Ampliação: x 1000 Diluição: 0,1
Localização: Meio Luz: Branca / Verde

Observações: Ampliação da Fotografia 4. Partículas ferrosas de desgaste de pequenas dimensões e partículas de "vernizes".

CLIENTE: ***INEGI***	ENSAIO: Banco de Ensaios
MORADA: Porto	**Ref. Óleos: PAO 2800 d = 0,1**
DATA: 09/06/14	

Fotografia 8

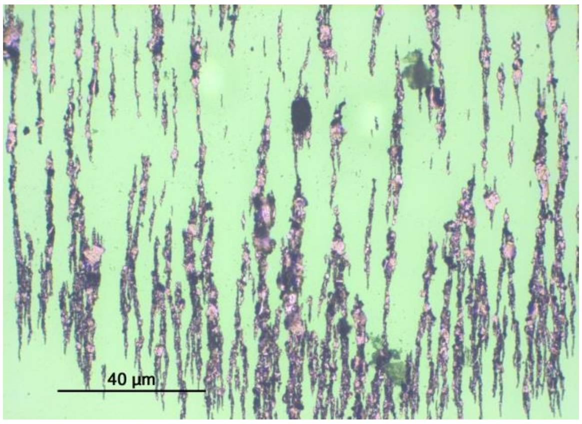

Ampliação: x 200 Diluíção: 0,1
Localização: Núcleo Luz: Branca / Verde

Observações: Presença de partículas ferrosas , algumas de grandes dimensões.

Fotografia 9

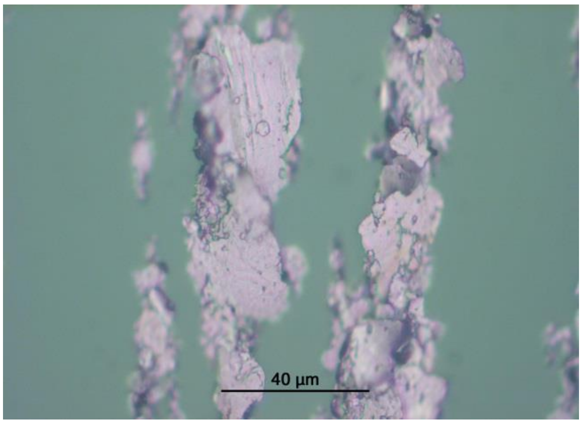

Ampliação: x 1000 Diluíção: 0,1
Localização: Núcleo Luz: Branca / Verde

Observações: Ampliação da Fotografia 8. Partículas ferrosas de grandes dimensões, algumas resultantes de desgaste de fadiga.

Fotografia 10

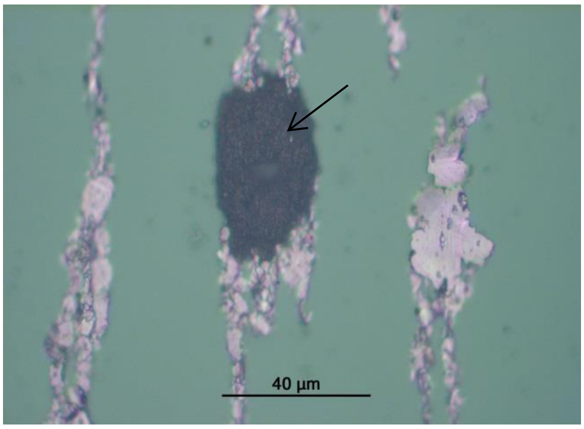

Ampliação: x 1000 Diluíção: 0,1
Localização: Núcleo Luz: Branca / Verde

Observações: Ampliação da Fotografia 8. Polimero de atrito de elevada densidade.

Fotografia 11

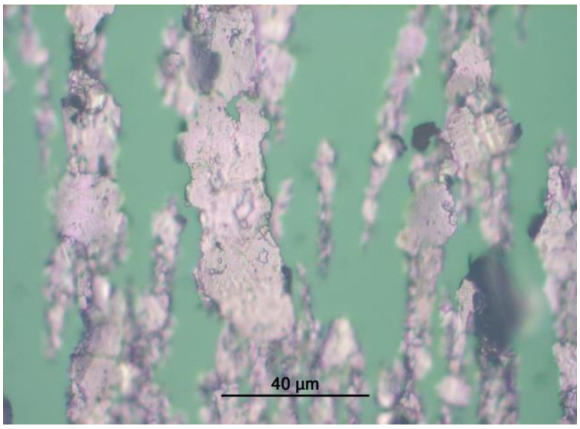

Ampliação: x 1000 Diluíção: 0,1
Localização: Núcleo Luz: Branca / Verde

Observações: Ampliação da Fotografia 8. Partículas ferrosas de grandes dimensões, algumas resultantes de desgaste de fadiga.

CLIENTE: ***INEGI***	ENSAIO: Banco de Ensaios
MORADA: Porto	**Ref. Óleos: PAG d = 1**
DATA: 09/06/14	

Fotografia 13

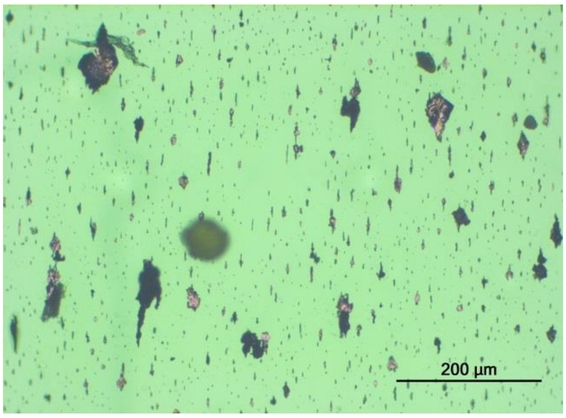

Ampliação: x 200 Diluição: 1
Localização: Núcleo Luz: Branca / Verde

Observações: Presença de algumas partículas ferrosas de grandes dimensões.

Fotografia 14

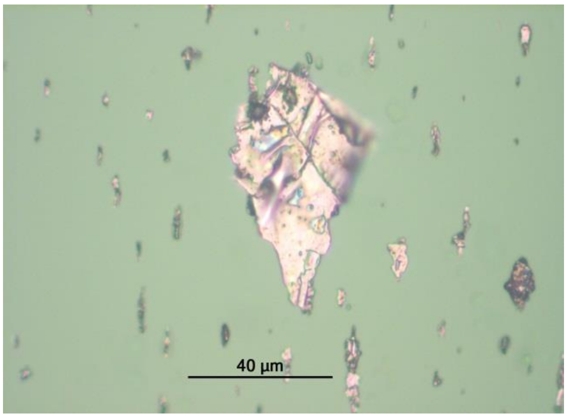

Ampliação: x 1000 Diluição: 1
Localização: Núcleo Luz: Branca / Verde

Observações: Ampliação da Fotografia 13. Partículaferrosa de grandes dimensões, típica de desgaste de adesão.

Fotografia 15

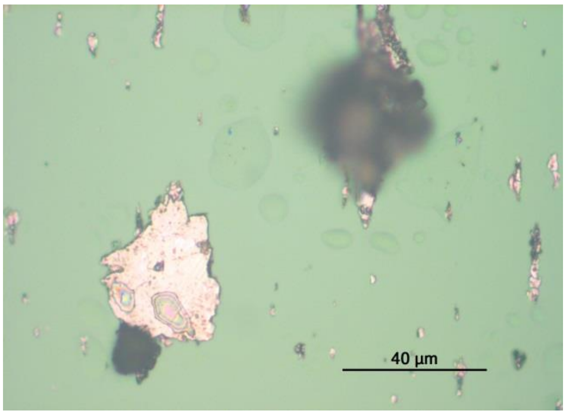

Ampliação: x 1000 Diluição: 1
Localização: Nucleo Luz: Branca / Verde

Observações: Ampliação da Fotografia 13. Partícula ferrosa de grandes dimensões, típicas de desgaste de fadiga e óxidos termicos.

Fotografia 16

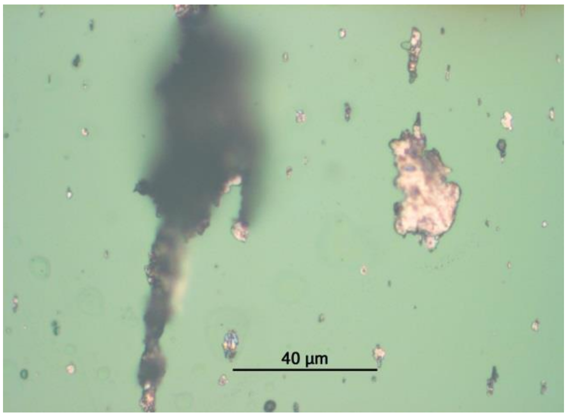

Ampliação: x 1000 Diluição: 1
Localização: Nucleo Luz: Branca / Verde

Observações: Ampliação da Fotografia 13. Partículas ferrosasde médias dimensões, típicas de desgaste de fadiga e óxidos termicos.

INEGI
Campus da FEUP
Rua Dr. Roberto Frias, 400
4200-465 Porto
PORTUGAL

inegi@inegi.up.pt
+ 351 229578710
+ 351 229537352

driving innovation *since 1986*

www.inegi.up.pt

U.PORTO

D. KISSsoft analysis of the planetary gearbox

KISSsoft Release 03/2013

KISSsoft University license - Universidade do Porto

File

Name : report_3006

Changed by: em09047 am: 30.06.2014 um: 13:20:09

Important hint: At least one warning has occurred during the calculation:

1-> The calculation of micropitting specified in ISO15144 is not designed for use with internal toothing because it has not yet been subject to sufficient investigation.

The results can only be used for information purposes.

CALCULATION OF A HELICAL PLANETARY GEAR

Drawing or article number:

Gear 1: 0.000.0

Gear 2: 0.000.0

Gear 3: 0.000.0

Calculation method ISO 6336:2006 Method B

		Gear 1	Gear 2	Gear 3
Number of planets	[p]	(1)	3	(1)
Power (kW)	[P]		65.45	
Speed (1/min)	[n]	1000.0		0.0
Speed difference for planet bearing calculation (1/min)	[n2]		750.0	
Speed planet carrier (1/min)	[nSteg]		250.0	
Torque (Nm)	[T]	625.0	0.0	1875.0
Torque Pl.-Carrier (Nm)	[TSteg]		2500.000	
Application factor	[KA]		1.25	
Power distribution factor	[Kgam]		1.00	
Required service life	[H]		20000.00	
Gear driving (+) / driven (-)		+	-/+	-

1. TOOTH GEOMETRY AND MATERIAL

(geometry calculation according to DIN 3960:1987)

		Gear 1	Gear 2	Gear 3
Center distance (mm)	[a]		73.035	
Centre distance tolerance		ISO 286:2010 Measure js7		
Normal module (mm)	[mn]		2.0000	
Pressure angle at normal section (°)	[alfn]		20.0000	
Helix angle at reference circle (°)	[beta]		10.0000	
Number of teeth	[z]	36	36	-108
Facewidth (mm)	[b]	42.00	42.00	42.00
Hand of gear		left	right	right

Planetary axles can be placed in regular pitch.: 120°

Accuracy grade	[Q-ISO1328:1995]	6	6	6
Inner diameter (mm)	[di]	0.00	0.00	
External diameter (mm)	[di]			0.00
Inner diameter of gear rim (mm)	[dbi]	0.00	0.00	
Outer diameter of gear rim (mm)	[dbi]			0.00

Material

Gear 1: 18CrNiMo7-6, Case-carburized steel, case-hardened
ISO 6336-5 Figure 9/10 (MQ), core strength >=25HRC Jominy J=12mm<HRC28

Gear 2: 18CrNiMo7-6, Case-carburized steel, case-hardened
ISO 6336-5 Figure 9/10 (MQ), core strength >=25HRC Jominy J=12mm<HRC28

Gear 3: 18CrNiMo7-6, Case-carburized steel, case-hardened
ISO 6336-5 Figure 9/10 (MQ), core strength >=25HRC Jominy J=12mm<HRC28

------- Gear 1 ------------ Gear 2 ------------ Gear 3 ---

Surface hardness HRC 61 HRC 61 HRC 61

Material quality according to ISO 6336:2006 Normal (Life factors ZNT and YNT >=0.85)

Fatigue strength. tooth root stress (N/mm²)	[sigFlim]	430.00	430.00	430.00
Fatigue strength for Hertzian pressure (N/mm²)	[sigHlim]	1500.00	1500.00	1500.00
Tensile strength (N/mm²)	[Rm]	1200.00	1200.00	1200.00
Yield point (N/mm²)	[sigs]	850.00	850.00	850.00
Young's modulus (N/mm²)	[E]	206000	206000	206000
Poisson's ratio	[ny]	0.300	0.300	0.300
Mean roughness, Ra, tooth flank (µm)	[RAH]	0.60	0.60	0.60
Mean roughness height, Rz, flank (µm)	[RZH]	4.80	4.80	4.80
Mean roughness height, Rz, root (µm)	[RZF]	20.00	20.00	20.00

Tool or reference profile of gear 1 :

Reference profile 1.25 / 0.25 / 1.0 ISO 53.2:1997 Profil C

Dedendum coefficient	[hfP*]	1.250
Root radius factor	[rhofP*]	0.250
Addendum coefficient	[haP*]	1.000
Tip radius factor	[rhoaP*]	0.000
Tip form height coefficient	[hFaP*]	0.000
Protuberance height factor	[hprP*]	0.000
Protuberance angle	[alfprP]	0.000
Ramp angle	[alfKP]	0.000

not topping

Tool or reference profile of gear 2 :

Reference profile 1.25 / 0.25 / 1.0 ISO 53.2:1997 Profil C

Dedendum coefficient	[hfP*]	1.250
Root radius factor	[rhofP*]	0.250
Addendum coefficient	[haP*]	1.000
Tip radius factor	[rhoaP*]	0.000
Tip form height coefficient	[hFaP*]	0.000
Protuberance height factor	[hprP*]	0.000
Protuberance angle	[alfprP]	0.000
Ramp angle	[alfKP]	0.000

not topping

Tool or reference profile of gear 3 :

Reference profile 1.25 / 0.25 / 1.0 ISO 53.2:1997 Profil C

Dedendum coefficient	[hfP*]	1.250
Root radius factor	[rhofP*]	0.250

Addendum coefficient	[haP*]	1.000
Tip radius factor	[rhoaP*]	0.000
Tip form height coefficient	[hFaP*]	0.000
Protuberance height factor	[hprP*]	0.000
Protuberance angle	[alfprP]	0.000
Ramp angle	[alfKP]	0.000
		not topping

Summary of reference profile gears:

Dedendum reference profile (in module)	[hfP*]	1.250	1.250	1.250
Root radius reference profile (in module)	[rofP*]	0.250	0.250	0.250
Addendum reference profile (in module)	[haP*]	1.000	1.000	1.000
Protuberance height coefficient (in module)	[hprP*]	0.000	0.000	0.000
Protuberance angle (°)	[alfprP]	0.000	0.000	0.000
Tip form height coefficient (in module)	[hFaP*]	0.000	0.000	0.000
Ramp angle (°)	[alfKP]	0.000	0.000	0.000

Type of profile modification: none (only running-in)

Tip relief (µm)	[Ca]	2.00	2.00	2.00

Lubrication type		oil bath lubrication
Type of oil		Oil: GEM 4-320 N Klübersynth
Lubricant base		Synthetic oil based on Polyalphaolefin
Kinem. viscosity oil at 40 °C (mm²/s)	[nu40]	320.00
Kinem. viscosity oil at 100 °C (mm²/s)	[nu100]	36.00
FZG test A/8.3/90 (ISO 14635-1:2006)	[FZGtestA]	14
Specific density at 15 °C (kg/dm³)	[roOil]	0.850
Oil temperature (°C)	[TS]	85.000

		Gear 1		Gear 2		Gear 3
Overall transmission ratio	[itot]		4.000			
Gear ratio	[u]		1.000		-3.000	
Transverse module (mm)	[mt]		2.031			
Pressure angle at pitch circle (°)	[alft]		20.284			
Working transverse pressure angle (°)	[alfwt]		20.122		20.122	
	[alfwt.e/i]		20.154 / 20.090		20.090 / 20.154	
Working pressure angle at normal section (°)	[alfwn]		19.841		19.841	
Helix angle at operating pitch circle (°)	[betaw]		9.990		9.990	
Base helix angle (°)	[betab]		9.391			
Reference centre distance (mm)	[ad]		73.111		-73.111	
Sum of profile shift coefficients	[Summexi]		-0.0377		0.0377	
Profile shift coefficient	[x]	-0.0189		-0.0189		0.0566
Tooth thickness (Arc) (module) (module)	[sn*]	1.5571		1.5571		1.6120
Tip alteration (mm)	[k*mn]	0.000		0.000		0.000
Reference diameter (mm)	[d]	73.111		73.111		-219.332
Base diameter (mm)	[db]	68.577		68.577		-205.731
Tip diameter (mm)	[da]	77.035		77.035		-215.106
(mm)	[da.e/i]	77.035 / 77.025		77.035 / 77.025		-215.106 / -215.116
Tip diameter allowances (mm)	[Ada.e/i]	0.000 / -0.010		0.000 / -0.010		0.000 / -0.010
Tip form diameter (mm)	[dFa.e/i]	77.035 / 77.025		77.035 / 77.025		-215.106 / -215.116
Active tip diameter (mm)	[dNa.e/i]	77.035 / 77.025		77.035 / 77.025		-215.106 / -215.116
Operating pitch diameter (mm)	[dw]	73.035		73.035 / 73.035		-219.105
(mm)	[dw.e]	73.050		73.050 / 73.020		-219.060
(mm)	[dw.i]	73.020		73.020 / 73.050		-219.150
Root diameter (mm)	[df]	68.035		68.035		-224.106
Generating Profile shift coefficient	[xE.e/i]	-0.0669 / -0.0944		-0.0669 / -0.0944		-0.0087 / -0.0430

Manufactured root diameter with xE (mm)	[df.e]	67.84	67.84	-224.37
(mm)	[df.i]	67.73	67.73	-224.50
Theoretical tip clearance (mm)	[c]	0.500	0.500/ 0.500	0.500
Tip clearance upper allowance (mm)	[c.e]	0.671	0.671/ 0.719	0.671
Tip clearance lower allowance (mm)	[c.i]	0.581	0.581/ 0.616	0.581
Active root diameter (mm)	[dNf]	70.232	70.232/ 69.718	-222.731
(mm)	[dNf.e]	70.256	70.256/ 69.740	-222.689
(mm)	[dNf.i]	70.213	70.213/ 69.702	-222.765
Root form diameter (mm)	[dFf]	69.725	69.725	-223.079
(mm)	[dFf.e/i]	69.627 / 69.573	69.627 / 69.573	-223.374 / -223.527
Internal toothing: Calculation dFf with pinion type cutter (z0= 35, x0= 0.000)				
Reserve (dNf-dFf)/2 (mm)	[cF.e/i]	0.341 / 0.293	0.083 / 0.037	0.419 / 0.305
Addendum (mm)	[ha = mn * (haP*+x)]	1.962	1.962	2.113
(mm)	[ha.e/i]	1.962 / 1.957	1.962 / 1.957	2.113 / 2.108
Dedendum (mm)	[hf = mn * (hfP*-x)]	2.538	2.538	2.387
(mm)	[hf.e/i]	2.634 / 2.689	2.634 / 2.689	2.517 / 2.586
Roll angle at dFa (°)	[xsi_dFa.e/i]	29.321 / 29.303	29.321 / 29.303	17.493 / 17.502
Roll angle to dNf (°)	[xsi_dNf.e/i]	12.755 / 12.591	12.755 / 12.591	
	[xsi_dNf.e/i]		10.595 / 10.421	23.738 / 23.793
Roll angle at dFf (°)	[xsi_dFf.e/i]	10.066 / 9.801	10.066 / 9.801	24.232 / 24.341
Tooth height (mm)	[H]	4.500	4.500	4.500
Virtual gear no. of teeth	[zn]	37.555	37.555	-112.666
Normal tooth thickness at tip cyl. (mm)	[san]	1.520	1.520	1.769
(mm)	[san.e/i]	1.452 / 1.405	1.452 / 1.405	1.679 / 1.626
Normal spacewidth at root cylinder (mm)	[efn]	0.000	0.000	1.218
(mm)	[efn.e/i]	0.000 / 0.000	0.000 / 0.000	1.205 / 1.198
Max. sliding velocity at tip (m/s)	[vga]	0.783	0.783/ 0.261	0.329
Specific sliding at the tip	[zetaa]	0.568	0.568/ 0.189	0.400
Specific sliding at the root	[zetaf]	-1.315	-1.315/ -0.667	-0.234
Sliding factor on tip	[Kga]	0.273	0.273/ 0.091	0.115
Sliding factor on root	[Kgf]	-0.273	-0.273/ -0.115	-0.091
Pitch on reference circle (mm)	[pt]		6.380	
Base pitch (mm)	[pbt]		5.984	
Transverse pitch on contact-path (mm)	[pet]		5.984	
Lead height (mm)	[pz]	1302.603	1302.603	3907.810
Axial pitch (mm)	[px]	36.183	36.183	36.183
Length of path of contact (mm)	[ga]	9.969	11.267	
(mm)	[ga.e/i]	10.012 / 9.903	11.311 / 11.196	
Length T1-A (mm)	[T1A]	7.579	17.547/ 6.280	-31.406
Length T1-B (mm)	[T1B]	11.563	13.563/ 11.563	-36.689
Length T1-C (mm)	[T1C]	12.563	12.563/ 12.563	-37.689
Length T1-D (mm)	[T1D]	13.563	11.563/ 12.264	-37.390
Length T1-E (mm)	[T1E]	17.547	7.578/ 17.547	-42.673
Diameter of single contact point B (mm)	[d-B]	72.371	73.747/ 72.371	-218.425
(mm)	[d-B.e]	72.371	73.715/ 72.371	-218.454
(mm)	[d-B.i]	72.364	73.787/ 72.364	-218.388
Diameter of single contact point D (mm)	[d-D]	73.747	72.371/ 72.832	-218.900
(mm)	[d-D.e]	73.715	72.371/ 72.802	-218.900
(mm)	[d-D.i]	73.787	72.364/ 72.873	-218.912
Transverse contact ratio	[Eps.a]	1.666	1.883	
Transverse contact ratio with allowances	[Eps.aEffe/i]	1.673 / 1.655	1.890 / 1.871	
Overlap ratio	[Eps.b]	1.161	1.161	

Total contact ratio	[Eps.G]	2.827	3.044		
Total contact ratio with allowances	[Eps.gEffe/i]	2.834 / 2.816	3.051 / 3.032		

2. FACTORS OF GENERAL INFLUENCE

------- Gear 1 ------------ Gear 2 ------------ Gear 3 ---

Nominal circum. force at pitch circle (N)	[Ft]	5699.119	5699.119		
Axial force (N)	[Fa]	1004.9	1004.9	1004.9	
Axial force (total) (N)	[Fatot=Fa*	3]		3014.7	3014.7
Radial force (N)	[Fr]	2106.309	2106.309		
Normal force (N)	[Fnorm]	6158.4	6158.4	6158.4	
Tangent.load at p.c.d.per mm (N/mm) (N/mm)	[w]	135.69	135.69		
Only as information: Forces at operating pitch circle:					
Nominal circumferential force (N)	[Ftw]	5705.027	5705.027		
Axial force (N)	[Fa]	1004.9	1004.9/ 1004.9	1004.9	
Axial force (total) (N)	[Fatot=Fa*	3]		3014.7	3014.7
Radial force (N)	[Fr]	2090.253	2090.253		
Circumferential speed pitch d.. (m/sec)	[v]		2.87		
Running-in value (µm)	[yp]	0.525	0.600		
Running-in value (µm)	[yf]	0.487	0.563		
Gear body coefficient	[CR]	1.000	1.000		
Correction coefficient	[CM]	0.800	0.800		
Reference profile coefficient	[CBS]	0.975	0.975		
Material coefficient	[E/Est]	1.000	1.000		
Singular tooth stiffness (N/mm/µm)	[c']	13.114	14.931		
Meshing stiffness (N/mm/µm)	[cgalf]	19.662	24.816		
Meshing stiffness (N/mm/µm)	[cgbet]	16.712	21.094		
Reduced mass (kg/mm)	[mRed]	0.0045	0.0181		
Resonance speed (min-1)	[nE1]	17485	9822		
Nominal speed (-)	[N]	0.043	0.076		
Subcritical range					
Running-in value (µm)	[ya]	0.525	0.600		
Planets are supported by fixed restraint bolts					
lpa (mm) = 54.60 b (mm) = 42.00 dsh (mm) = 36.56					
Tooth trace deviation (active) (µm)	[Fby]	4.25	5.87		
from deformation of shaft (µm)	[fsh*B1]	4.10	0.45		
Tooth trace		0	0		
(0:without, 1:crowned, 2:Tip relief, 3:full modification)					
from production tolerances (µm)	[fma*B2]	14.14	14.14		
Running-in value y.b (µm)	[yb]	0.75	1.04		
Dynamic factor	[KV=max(KV12,KV23)]		1.03		
	[KV12,KV23]	1.01	1.03		
Face load factor - flank	[KHb]	1.20	1.35		
- Tooth root	[KFb]	1.18	1.31		
- Scuffing	[KBb]	1.20	1.35		
Transverse load factor - flank	[KHa]	1.18	1.26		
- Tooth root	[KFa]	1.18	1.26		
- Scuffing	[KBa]	1.18	1.26		
Helical load factor scuffing	[Kbg]	1.27	1.29		

Number of load cycles (in mio.)	[NL]	2700.0	900.0	900.0

3. TOOTH ROOT STRENGTH

Calculation of Tooth form coefficients according method: B
Tooth form factors calculated with manufacturing profile shift xE.e
Internal toothing: Calculation of YF, YS with pinion type cutter (z0= 35, x0= 0.000, rofP*= 0.250)

		------- Gear 1	------------ Gear 2	------------ Gear 3 ---
Tooth form factor	[YF]	1.46	1.46/ 1.16	0.95
Stress correction factor	[YS]	2.04	2.04/ 2.22	2.73
Bending lever arm (mm)	[hF]	2.11	2.11/ 1.67	2.28
Working angle (°)	[alfFen]	18.88	18.88/ 16.74	20.15
Tooth thickness at root (mm)	[sFn]	4.19	4.19/ 4.19	5.37
Tooth root radius (mm)	[roF]	0.94	0.94/ 0.94	0.73

(sFn* = 2.094/ 2.094/ 2.094/ 2.684 roF* = 0.470/ 0.470/ 0.470/ 0.366 dsFn = 68.50/ 68.50/ 68.50/ -224.18 alfsFn = 30.0/ 30.0/ 30.0/ 60.0)

		Gear 1	Gear 2	Gear 3
Contact ratio factor	[Yeps]	1.00	1.00	
Helical load factor	[Ybet]	0.92	0.92	
Deep tooth factor	[YDT]	1.00	1.00	
Gear rim factor	[YB]	1.00	1.00	1.00
Effective facewidth (mm)	[beff]	42.00	42.00/ 42.00	42.00
Nominal stress at tooth root (N/mm²)	[sigF0]	184.94	184.94/ 160.89	161.00
Tooth root stress (N/mm²)	[sigF]	330.16	330.16/ 341.94	342.19
Permissible bending stress at root of Test-gear				
Support factor	[YdrelT]	0.997	0.997/ 0.997	1.010
Surface factor	[YRrelT]	0.957	0.957	0.957
Size coefficient (Tooth root)	[YX]	1.000	1.000	1.000
Finite life factor	[YNT]	0.873	0.892	0.892
Alternating bending coefficient	[YM]	1.000	0.700	1.000
Stress correction factor	[Yst]		2.00	
Yst*sigFlim (N/mm²)	[sigFE]	860.00	860.00	860.00
Permissible tooth root stress (N/mm²)	[sigFP=sigFG/SFmin]	511.48	366.00/ 366.00	529.55
Limit strength tooth root (N/mm²)	[sigFG]	716.07	512.41/ 512.41	741.37
Required safety	[SFmin]	1.40	1.40/ 1.40	1.40
Safety for Tooth root stress	[SF=sigFG/sigF]	2.17	1.55/ 1.50	2.17
Transmittable power (kW)	[kWRating]	101.40	72.56/ 70.06	101.29

4. SAFETY AGAINST PITTING (TOOTH FLANK)

		------- Gear 1	------------ Gear 2	------------ Gear 3 ---
Zone factor	[ZH]	2.47	2.47	
Elasticity coefficient (N^.5/mm)	[ZE]	189.81	189.81	
Contact ratio factor	[Zeps]	0.77	0.73	
Helix angle factor	[Zbet]	1.01	1.01	
Effective facewidth (mm)	[beff]	42.00	42.00	
Nominal flank pressure (N/mm²)	[sigH0]	706.41	383.63	
Surface pressure at operating pitch circle (N/mm²)	[sigHw]	953.41	568.66	
Single tooth contact factor	[ZB,ZD]	1.00	1.00/ 1.00	1.00
Flank pressure (N/mm²)	[sigH]	953.41	953.41/ 568.66	568.66
Lubrication coefficient at NL	[ZL]	1.047	1.047/ 1.047	1.047
Speed coefficient at NL	[ZV]	0.971	0.971/ 0.971	0.971

Roughness coefficient at NL	[ZR]	0.951	0.951/ 0.980	0.980
Material pairing coefficient at NL	[ZW]	1.000	1.000/ 1.000	1.000
Finite life factor	[ZNT]	0.885	0.915	0.915
Small no. of pittings permissible:	no			
Size coefficient (flank)	[ZX]	1.000	1.000	1.000
Permissible surface pressure (N/mm²)	[sigHP=sigHG/SHmin]	1283.35	1327.33/1366.79	1366.79
Limit strength pitting (N/mm²)	[sigHG]	1283.35	1327.33/1366.79	1366.79

Safety for surface pressure at operating pitch circle

	[SHw]	1.35	1.39/ 2.40	2.40
Required safety	[SHmin]	1.00	1.00/ 1.00	1.00
Transmittable power (kW)	[kWRating]	118.59	126.85/378.10	378.10
Safety for stress at single tooth contact	[SHBD=sigHG/sigH]	1.35	1.39/ 2.40	2.40
(Safety regarding nominal torque)	[(SHBD)^2]	1.81	1.94/ 5.78	5.78

4b. MICROPITTING ACCORDING TO ISO TR 15144-1:2010

Pairing Gear 1- 2:
Calculation of permissible specific film thickness
Lubricant load according to FVA Info sheet 54/7 10 (Oil: GEM 4-320 N Klübersynth)
Reference data FZG-C Test:

(Nm)	[T1]	265.1
(N/mm)	[Fbb]	236.3
(°)	[theOil]	90.0
(°)	[theM]	121.4
(°)	[theB]	217.9
(µm)	[h]	0.073
	[WW]	1.00
	[lamGFT]	0.146

Permissible specific film thickness (µm) [lamGFP] 0.204
Intermediate results according to ISO TR 15144:2010

	[mym]	0.070
	[XL]	0.800
	[XR]	1.219
(°)	[theM]	90.9
	[XCa]	1.000
	[HV]	0.128
(N/mm²)	[Er]	226374
(m2/N)	[alf38]	0.01378
(Ns/m2)	[etatM]	37.0
(µm)	[Ra]	0.6

Calculation of speeds, load distribution and flank curvature according to method B following ISO 15144-1:2010
With modifications following ISO TR CD 15144-2:2011
Ca taken as optimal in the calculation (0=no, 1=yes) 0 0
Minimal specific film thickness (µm) [lamGFY] 0.162 (hY=0.097 µm)
Safety against micropitting [Slam] 0.793
(For intermediate results refer to file:
Micropitting_12.tmp)

Pairing Gear 2- 3:
Calculation of permissible specific film thickness
Lubricant load according to FVA Info sheet 54/7 10 (Oil: GEM 4-320 N Klübersynth)
Reference data FZG-C Test:

(Nm)	[T1]	265.1
(N/mm)	[Fbb]	236.3
(°)	[theOil]	90.0

(°) [theM] 121.4
(°) [theB] 217.9
(µm) [h] 0.073
[WW] 1.00
[lamGFT]0.146

Permissible specific film thickness (µm)	[lamGFP]	0.204		

Safety against micropitting:
Calculation was not carried out. (Contact analysis under load is required.)

5. STRENGTH AGAINST SCUFFING

Calculation method according to
ISO TR 13989:2000

Lubrication coefficient (for lubrication type)	[XS]	1.000		
Multiple meshing factor	[Xmp]	2.0	2.0	
Relative structure coefficient (Scuffing)	[XWrelT]	1.000	1.000	
Thermal contact factor (N/mm/s^.5/K)	[BM]	13.780	13.780	13.780
Relevant tip relief (µm)	[Ca]	2.00	2.00	2.00
Optimal tip relief (µm)	[Ceff]	8.63	6.83	
Ca taken as optimal in the calculation (0=no, 1=yes)		0	0/ 0	0
Effective facewidth (mm)	[beff]	42.000	42.000	
Applicable circumferential force/facewidth (N/mm)				
	[wBt]	247.172	298.154	
((1)Kbg = 1.268, wBt*Kbg = 313.430)				
((2)Kbg = 1.286, wBt*Kbg = 383.357)				
Angle factor	[Xalfbet]	0.976	0.976	

Flash temperature-criteria			
Lubricant factor	[XL]	0.662	0.662
Tooth mass temperature (°C)	[theMi]	95.66	87.46
theM = theoil + XS*0.47*Xmp*theflm	[theflm]	11.34	2.61
Scuffing temperature (°C)	[theS]	371.91	371.91
Coordinate gamma (point of highest temp.)	[Gamma]	-0.397	-0.500
(1) [Gamma.A]=-0.397 [Gamma.E]=0.397			
(2) [Gamma.A]=-0.500 [Gamma.E]=0.397			
Highest contact temp. (°C)	[theB]	123.17	95.51
Flash factor (°K*N^-.75*s^.5*m^-.5*mm)	[XM]	50.058	50.058
Approach factor	[XJ]	1.017	1.017
Load sharing factor	[XGam]	0.780	0.690
Dynamic viscosity (mPa*s)	[etaM]	44.21	44.21
Coefficient of friction	[mym]	0.056	0.047
Required safety	[SBmin]	2.000	
Safety factor for scuffing (flash-temp)	[SB]	7.516	27.311

Integral temperature-criteria			
Lubricant factor	[XL]	0.800	
Tooth mass temperature (°C)	[theM-C]	98.14	86.72
theM-C = theoil + XS*0.70*theflaint	[theflaint]	9.39	1.23
Integral scuffing temperature (°C)	[theSint]	378.88	378.88
Flash factor (°K*N^-.75*s^.5*m^-.5*mm)	[XM]	50.058	50.058
Running-in factor (well run in)	[XE]	1.000	1.000
Contact ratio factor	[Xeps]	0.255	0.271
Dynamic viscosity (mPa*s)	[etaOil]	44.21	44.21
Averaged coefficient of friction	[mym]	0.069	0.044

Geometry factor	[XBE]	0.305	0.058
Meshing factor	[XQ]	1.000	1.000
Tip relief factor	[XCa]	1.210	1.363
Integral tooth flank temperature (°C)	[theint]	112.22	88.57
Required safety	[SSmin]	1.800	
Safety factor for scuffing (intg.-temp.)	[SSint]	3.38	4.28
Safety referring to transferred torque	[SSL]	10.79	82.27

6. MEASUREMENTS FOR TOOTH THICKNESS

		------- Gear 1	------------ Gear 2	------------ Gear 3 ---
Tooth thickness deviation		DIN 3967 cd25	DIN 3967 cd25	DIN 3967 cd25
Tooth thickness allowance (normal section) (mm)	[As.e/i]	-0.070/ -0.110	-0.070/ -0.110	-0.095/ -0.145
Number of teeth spanned	[k]	5.000	5.000	0.000
(Internal toothing: k = (Measurement gap number)				
Base tangent length (no backlash) (mm)	[Wk]	27.597	27.597	0.000
Actual base tangent length ('span') (mm)	[Wk.e/i]	27.531/ 27.493	27.531/ 27.493	0.000/ 0.000
Diameter of contact point (mm)	[dMWk.m]	73.753	73.753	0.000
Theoretical diameter of ball/pin (mm)	[DM]	3.389	3.389	3.320
Eff. Diameter of ball/pin (mm)	[DMeff]	3.500	3.500	3.500
Theor. dim. centre to ball (mm)	[MrK]	39.020	39.020	-106.971
Actual dimension centre to ball (mm)	[MrK.e/i]	38.935/ 38.885	38.935/ 38.885	-107.110/ -107.183
Diameter of contact point (mm)	[dMMr.m]	73.059	73.059	-218.951
Diametral measurement over two balls without clearance (mm)				
	[MdK]	78.041	78.041	-213.943
Actual dimension over balls (mm)	[MdK.e/i]	77.870/ 77.771	77.870/ 77.771	-214.221/ -214.366
Actual dimension over rolls (mm)	[MdR.e/i]	77.870/ 77.771	77.870/ 77.771	0.000/ 0.000
Actual dimensions over 3 rolls (mm)	[Md3R.e/i]	0.000/ 0.000	0.000/ 0.000	0.000/ 0.000
Note: Internal gears with helical teeth cannot be measured with rollers.				
Tooth thickness (chordal) in pitch diameter (mm)	['sn]	3.113	3.113	3.224
(mm)	['sn.e/i]	3.043/ 3.003	3.043/ 3.003	3.129/ 3.079
Reference chordal height from da.m (mm)	[ha]	1.992	1.992	2.099
Tooth thickness (Arc) (mm)	[sn]	3.114	3.114	3.224
(mm)	[sn.e/i]	3.044/ 3.004	3.044/ 3.004	3.129/ 3.079
Backlash free center distance (mm)	[aControl.e/i]	72.839/ 72.726	-73.261/ -73.382	
Backlash free center distance, allowances (mm)	[jta]	-0.196/ -0.309	-0.000/ -0.000	
dNf.i with aControl (mm)	[dNf0.i]	69.860	69.388	-223.499
Reserve (dNf0.i-dFf.e)/2 (mm)	[cF0.i]	0.116	-0.120	-0.062
Centre distance allowances (mm)	[Aa.e/i]	0.015/ -0.015	0.015/ -0.015	
Circumferential backlash from Aa (mm)	[jt_Aa.e/i]	0.011/ -0.011	0.011/ -0.011	
Radial clearance (mm)	[jr]	0.324/ 0.181	0.362/ 0.211	
Circumferential backlash (transverse section) (mm)				
	[jt]	0.234/ 0.131	0.270/ 0.156	
Normal backlash (mm)	[jn]	0.217/ 0.121	0.250/ 0.145	
Entire torsional angle (°)	[j.tSys]	0.1890/ 0.1214		
(j.tSys: Torsional angle of planet carrier for blocked shaft)				

7. GEAR ACCURACY

		Gear 1	Gear 2	Gear 3
According to ISO 1328:1995:				
Accuracy grade	[Q-ISO1328]	6	6	6
Single pitch deviation (µm)	[fpt]	7.50	7.50	8.50
Base circle pitch deviation (µm)	[fpb]	7.00	7.00	8.00
Cumulative circular pitch deviation over k/8 pitches (µm)	[Fpk/8]	12.00	12.00	16.00
Profile form deviation (µm)	[ffa]	6.50	6.50	7.50
Profile slope deviation (µm)	[fHa]	5.50	5.50	6.00
Total profile deviation (µm)	[Fa]	8.50	8.50	10.00
Helix form deviation (µm)	[ffb]	10.00	10.00	10.00
Helix slope deviation (µm)	[fHb]	10.00	10.00	10.00
Total helix deviation (µm)	[Fb]	14.00	14.00	15.00
Total cumulative pitch deviation (µm)	[Fp]	26.00	26.00	35.00
Concentricity deviation (µm)	[Fr]	21.00	21.00	28.00
Total radial composite deviation (µm)	[Fi"]	31.00	31.00	37.00
Radial tooth-to-tooth composite deviation (µm)	[fi"]	9.50	9.50	9.50
Total tangential composite deviation (µm)	[Fi']	37.00	36.00	46.00
Tangential tooth-to-tooth composite deviation (µm)	[fi']	11.00	10.00	12.00

Axis alignment tolerances (recommendation acc. ISO TR 10064:1992, Quality 6)

Maximum value for deviation error of axis (µm)	[fSigbet]	9.10	9.10
Maximum value for inclination error of axes (µm)	[fSigdel]	18.20	18.20

8. ADDITIONAL DATA

Maximal possible centre distance (eps_a=1.0)	[aMAX]	74.500	-71.390	
Mean coeff. of friction (acc. Niemann)	[mum]	0.058	0.047	
Wear sliding coef. by Niemann	[zetw]	0.946	0.578	
Meshpower (kW)		49.087	49.087	
Power loss from gear load (kW)		0.122	0.041	
Total power loss (kW)		0.491		
Total efficiency		0.993		
Weight - calculated with da (kg)	[Mass]	1.533	1.533	2.236
Total weight (kg)	[Mass]	8.367		

Moment of inertia (System referenced to wheel 1):
calculation without consideration of the exact tooth shape

single gears ((da+df)/2...di) (kg*m²)	[TraeghMom]	0.0008875	0.0008875	0.02501
System ((da+df)/2...di) (kg*m²)	[TraeghMom]	0.002385		

Indications for the manufacturing by wire cutting:

Deviation from theoretical tooth trace (µm)	[WireErr]	187.4	187.4	62.5
Permissible deviation (µm)	[Fb/2]	7.0	7.0	7.5

9. DETERMINATION OF TOOTHFORM

Data for the tooth form calculation :
Data not available.

REMARKS:

- Specifications with [.e/i] imply: Maximum [e] and Minimal value [i] with consideration of all tolerances

  Specifications with [.m] imply: Mean value within tolerance
- For the backlash tolerance, the center distance tolerances and the tooth thickness deviation are taken into account. Shown is the maximal and the minimal backlash corresponding the largest resp. the smallest allowances

  The calculation is done for the Operating pitch circle..
- Calculation of Zbet according Corrigendum 1 % ISO 6336-2:2008 with Zbet = 1/(COS(beta)^0.5)
- Details of calculation method:

  cg according to method B

  KV according to method B

  KHb, KFb according method C

  fma following equation (64), Fbx following (52/53/56)

  fsh calculated by exactly following the method in Appendix D, ISO 6336-1:2006

  Literature: Journal "Antriebstechnik", 6/2007, p.64.

  KHa, KFa according to method B

End of Report lines: 575

File

Name : report_3006_contactanalysis
Changed by: em09047 am: 30.06.2014 um: 13:21:39

Contact analysis

Determination of Kγ
Sun gear - Planets (Right Tooth Flank)
Planets - Internal gear (Left Tooth Flank)

Total power loss	(kW)	0.566
Efficiency	(%)	99.14

Planet		1	2	3
Center distance error	(μm)	0.000	0.000	0.000
Pitch error	(μm)	0.000	0.000	0.000

Single pitch deviation: Sun gear - Planets	[fpt]	0.0000	μm
Single pitch deviation: Planets - Internal gear	[fpt]	0.0000	μm
Coefficient of friction: Sun gear - Planets	[μ]	0.0500	
Coefficient of friction: Planets - Internal gear	[μ]	0.0500	

Accuracy of calculation medium
Partial load for calculation 100.00 %
Center distance [a] 73.0350 mm
Sun gear - Planets: fma = 0.000 μm, fHβ = 0.000 μm
Planets - Internal gear: fma = 0.000 μm, fHβ = 0.000 μm

Torsion
Sun gear: -
Planets: -
Internal gear: -
Planet carrier: -

Angle to first planet: 0°
Axis alignment
Sun gear: concerning gear axis, dx = 0.000 μm, dz = 0.000 μm
Planets: concerning planet bolts, dr = 0.000 μm, dt = 0.000 μm
Internal gear: concerning gear axis, dx = 0.000 μm, dz = 0.000 μm
Planet carrier: concerning gear axis, dx = 0.000 μm, dz = 0.000 μm
Planet pin: concerning planet carrier, dr = 0.000 μm, dt = 0.000 μm

		min	max	Δ	μ	σ
Transmission error of planet stage	(μm)	-8.0781	-7.7794	0.2986	-7.8775	0.0894
Total power loss	(kW)	0.5293	0.5790	0.0497	0.5658	0.0125

Planet load distribution
Sun gear - Planets

Planet 1	(Nm)	208.2780	208.3737	0.0957	208.3302	0.0124
Planet 2	(Nm)	208.2950	208.3750	0.0799	208.3334	0.0100
Planet 3	(Nm)	208.2514	208.3892	0.1378	208.3338	0.0129

Planets - Internal gear

Planet 1	(Nm)	206.4588	206.8319	0.3731	206.5981	0.0778
Planet 2	(Nm)	206.4668	206.8337	0.3668	206.5997	0.0767
Planet 3	(Nm)	206.4637	206.8006	0.3369	206.5995	0.0733

Kγ

Planet 1: (208.3302 / 208.3333) = 1.000

Planet 2: (208.3334 / 208.3333) = 1.000

Planet 3: (208.3338 / 208.3333) = 1.000

Angular shifting of planet meshing, relative to operating pitch points C

Planet 1, meshing with sun: 0°, meshing with rim: -5°

Planet 2, meshing with sun: 0°, meshing with rim: -5°

Planet 3, meshing with sun: 0°, meshing with rim: -5°

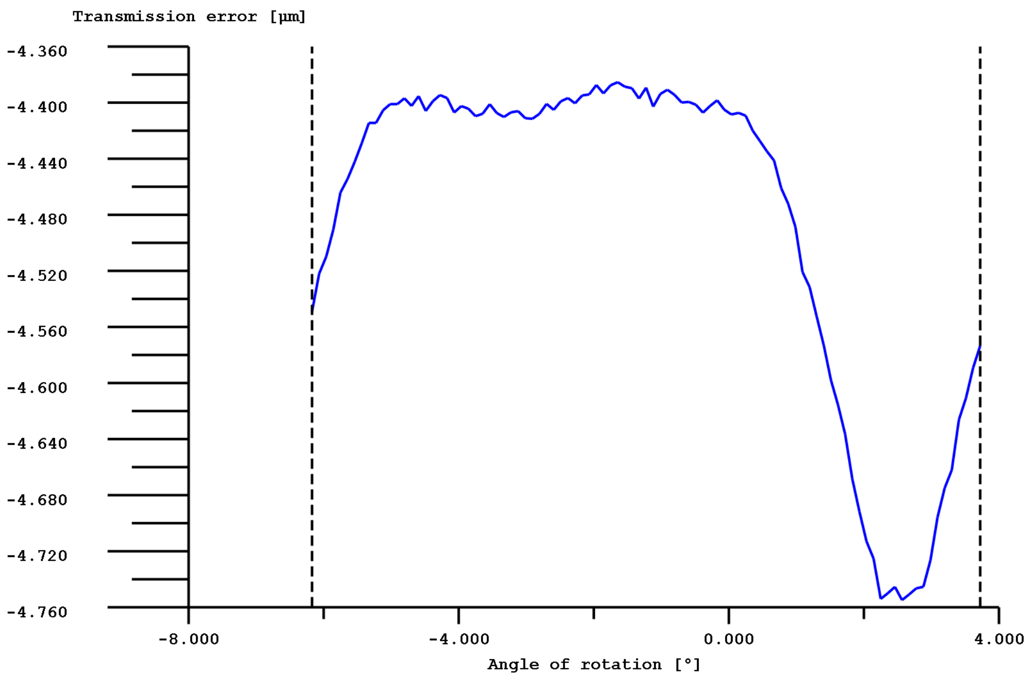

wt = 100 %, a = 0.000 mm,fpt = 0.000 µm,µ = 0Working flank: Right flank

Figure: Transmission error

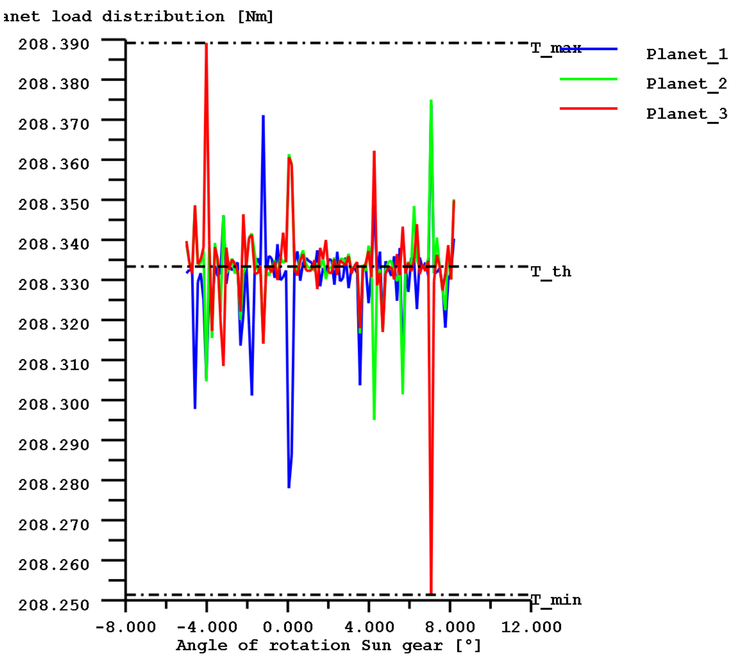

wt = 100 %, a = 73.035 mm,fpt1 = 0.000 µm,fpt2 = 0.000 µm,µ1 = 0.05,µ2 = 0.05
Figure: Planet load distribution

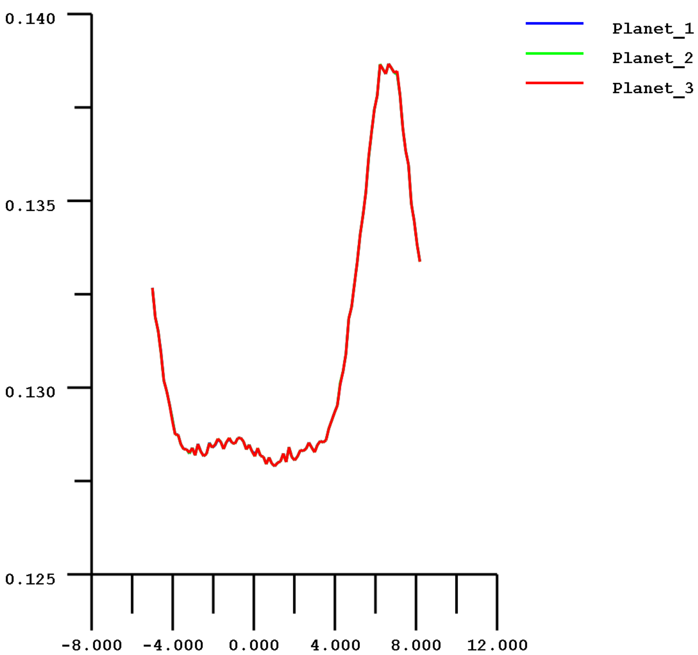

wt = 100 %, a = 73.035 mm,fpt1 = 0.000 µm,fpt2 = 0.000 µm,µ1 = 0.05,µ2 = 0.05
Figure: Planet transmission error

<u>Sun gear - Planets - Planet 1</u>

		min	max	Δ	µ	σ
Transmission error	(µm)	-4.7548	-4.3854	0.3694	-4.4831	0.1204
Stiffness curve	(N/mm/µm)	19.2312	20.6977	1.4664	20.2519	0.3711
Line load	(N/mm)	0.0000	166.4619	166.4619	86.1922	17.7536

Torque Gear 1	(Nm)	208.2780	208.3737	0.0957	208.3302	0.0124
Torque Gear 2	(Nm)	232.9784	242.6930	9.7145	237.0141	2.1413
Power loss	(W)	125.1118	141.0372	15.9253	137.3525	4.1842
Flash temperature	(°)	90.8645	130.0546	39.1901	103.1199	8.0303
Lubricating film	(µm)	0.0910	0.2963	0.2053	0.1267	0.0259
Hertzian stress	(N/mm²)		1189.8185		805.2227	
Safety against micropitting		0.7434				

Transverse contact ratio under load	[ε_a']	1.811
Overlap ratio under load	[ε_b']	1.126
Total contact ratio under load	[ε_g']	2.937

KHβ = (wmax/wm) = 1, (wmax = 186.161 N/mm, wm = 186.161 N/mm)

Planets - Internal gear - Planet 1

		min	max	Δ	µ	σ
Transmission error	(µm)	144.2013	144.6219	0.4206	144.4837	0.1259
Stiffness curve	(N/mm/µm)	26.1468	27.6564	1.5096	26.6733	0.3864
Line load	(N/mm)	0.0000	118.9736	118.9736	69.9131	16.5288
Torque Gear 2	(Nm)	206.4588	206.8319	0.3731	206.5981	0.0778
Torque Gear 3	(Nm)	-639.7816	-636.9883	2.7933	-638.3792	0.6356
Power loss	(W)	50.4873	52.1510	1.6637	51.2497	0.3973
Flash temperature	(°)	87.2716	98.7243	11.4527	90.6776	2.2911
Lubricating film	(µm)	0.0835	0.6183	0.5349	0.2225	0.0871
Hertzian stress	(N/mm²)		959.1102		598.1836	
Safety against micropitting		0.9102				

Transverse contact ratio under load	[ε_a']	2.168
Overlap ratio under load	[ε_b']	1.120
Total contact ratio under load	[ε_g']	3.289

KHβ = (wmax/wm) = 1, (wmax = 186.161 N/mm, wm = 186.161 N/mm)

Sun gear - Planets - Planet 2

		min	max	Δ	µ	σ
Transmission error	(µm)	-4.7548	-4.3854	0.3693	-4.4830	0.1205
Stiffness curve	(N/mm/µm)	19.2259	20.6931	1.4672	20.2488	0.3702
Line load	(N/mm)	0.0000	166.4538	166.4538	86.1932	17.7408
Torque Gear 1	(Nm)	208.2950	208.3750	0.0799	208.3334	0.0100
Torque Gear 2	(Nm)	232.9798	242.6876	9.7078	237.0152	2.1378
Power loss	(W)	125.1140	141.0387	15.9248	137.3550	4.1842
Flash temperature	(°)	90.8645	130.0529	39.1884	103.1209	8.0295
Lubricating film	(µm)	0.0910	0.3490	0.2580	0.1277	0.0323
Hertzian stress	(N/mm²)		1189.7899		805.2964	
Safety against micropitting		0.7434				

Transverse contact ratio under load	[ε_a']	1.811
Overlap ratio under load	[ε_b']	1.126
Total contact ratio under load	[ε_g']	2.937

KHβ = (wmax/wm) = 1, (wmax = 186.161 N/mm, wm = 186.161 N/mm)

Planets - Internal gear - Planet 2

		min	max	Δ	µ	σ
Transmission error	(µm)	144.2013	144.6219	0.4206	144.4837	0.1259
Stiffness curve	(N/mm/µm)	26.1516	27.6564	1.5048	26.6745	0.3871
Line load	(N/mm)	0.0000	118.9770	118.9770	69.9133	16.5280

Torque Gear 2	(Nm)	206.4668	206.8337	0.3668	206.5997	0.0767
Torque Gear 3	(Nm)	-639.8952	-636.9884	2.9068	-638.3821	0.6378
Power loss	(W)	50.4873	52.1360	1.6488	51.2500	0.3974
Flash temperature	(°)	87.2716	98.7244	11.4528	90.6778	2.2912
Lubricating film	(µm)	0.0835	0.6224	0.5389	0.2226	0.0875
Hertzian stress	(N/mm²)		959.2266		598.1545	
Safety against micropitting		0.9102				

Transverse contact ratio under load	[ε_a']	2.168
Overlap ratio under load	[ε_b']	1.120
Total contact ratio under load	[ε_g']	3.289

KHβ = (wmax/wm) = 1, (wmax = 186.161 N/mm, wm = 186.161 N/mm)

<u>Sun gear - Planets - Planet 3</u>

		min	max	Δ	µ	σ
Transmission error	(µm)	-4.7547	-4.3854	0.3693	-4.4830	0.1205
Stiffness curve	(N/mm/µm)	19.2261	20.6934	1.4674	20.2451	0.3774
Line load	(N/mm)	0.0000	166.4506	166.4506	86.2082	17.7104
Torque Gear 1	(Nm)	208.2514	208.3892	0.1378	208.3338	0.0129
Torque Gear 2	(Nm)	232.9833	242.6860	9.7028	237.0093	2.1462
Power loss	(W)	125.1155	141.0457	15.9301	137.3517	4.1964
Flash temperature	(°)	90.8645	130.0516	39.1871	103.1230	8.0301
Lubricating film	(µm)	0.0910	0.3338	0.2428	0.1274	0.0304
Hertzian stress	(N/mm²)		1189.7782		805.4364	
Safety against micropitting		0.7434				

Transverse contact ratio under load	[ε_a']	1.811
Overlap ratio under load	[ε_b']	1.116
Total contact ratio under load	[ε_g']	2.926

KHβ = (wmax/wm) = 1, (wmax = 186.161 N/mm, wm = 186.161 N/mm)

<u>Planets - Internal gear - Planet 3</u>

		min	max	Δ	µ	σ
Transmission error	(µm)	144.2013	144.6219	0.4206	144.4837	0.1259
Stiffness curve	(N/mm/µm)	26.1516	27.6564	1.5048	26.6751	0.3875
Line load	(N/mm)	0.0000	118.9788	118.9788	69.9133	16.5280
Torque Gear 2	(Nm)	206.4637	206.8006	0.3369	206.5995	0.0733
Torque Gear 3	(Nm)	-639.8942	-636.9858	2.9084	-638.3820	0.6291
Power loss	(W)	50.4870	52.1362	1.6492	51.2500	0.3973
Flash temperature	(°)	87.2716	98.7244	11.4528	90.6778	2.2912
Lubricating film	(µm)	0.0835	0.6238	0.5404	0.2226	0.0876
Hertzian stress	(N/mm²)		959.1013		598.1556	
Safety against micropitting		0.9102				

Transverse contact ratio under load	[ε_a']	2.168
Overlap ratio under load	[ε_b']	1.120
Total contact ratio under load	[ε_g']	3.289

KHβ = (wmax/wm) = 1, (wmax = 186.161 N/mm, wm = 186.161 N/mm)

End of Report lines: 193
